Design of an Inverse Photoemission Spectrometer for the Study of Strongly Correlated Materials

by

Christopher McMahon

A thesis
presented to the University of Waterloo
in fulfillment of the
thesis requirement for the degree of
Master of Science
in
Physics

Waterloo, Ontario, Canada, 2012

Abstract

The design and construction of a state-of-the-art ultra-high vacuum spectrometer for the performance of angle-resolved inverse photoemission spectroscopy is presented. Detailed descriptions of its most important components are included, especially the Geiger-Müller ultraviolet photodetectors. By building on recent developments in the literature, we expect our spectrometer to achieve resolution comparable or superior to that of other prominent groups, and in general be one of the foremost apparatus for studying the momentum dependence of the unoccupied states in strongly correlated materials. Summaries of the theory of angle-resolved inverse photoemission spectroscopy and the basics of ultra-high vacuum science are also included.

Acknowledgements

First and foremost, I would like to thank my supervisor David Hawthorn for his invaluable guidance over the past two years. During the many hours we have spent working together in the lab and at the CLS, he has earned not only my respect, but also my friendship.

I have benefited immensely from the advice that my fellow researchers at UW and the CLS have given me. In particular, I must express my gratitude to Andrew, Tom, Ronny, Mao, Feizhou, and the many scientists working on the experimental floor of the CLS.

My thesis would not have been possible without the hard work of Mirko. His IT expertise was invaluable, not to mention all of his help with the heavy lifting.

Finally, I must thank my friends and fellow graduate students for all of their support. In particular, I would like to thank Kevin, Benji, and Kier for not letting me forget that life exists beyond the windowless walls of my lab.

Newton never mentioned that when climbing onto the shoulder of a giant, it helps if you have someone holding the ladder.

Dedication

This thesis is dedicated to my parents Brian and Jodi, whose loving support is the foundation upon which all my achievements stand.

Table of Contents

List of Tables

List of Figures

List of Abbreviations

ARIPES	Angle resolved inverse photoemission spectroscopy
A.U.	Arbitrary Units
CF	ConFlat
FWHM	Full width at half maximum
GM	Geiger-Müller
HV	High-vacuum
IPES	Inverse photoemission spectroscopy
K-cell	Knudsen cell
LEED	Low-energy electron diffraction
PES	Photoemission spectroscopy
preamp	Preamplifier
QCM	Quartz crystal monitor
SCA	Single channel analyzer
SHV	Safe high voltage
TSP	Titanium sublimation pump
turbo	Turbomolecular pump
UHV	Ultra-high vacuum
VUV	Vacuum ultraviolet
XHV	Extreme-high vacuum
X-ray BIS	X-ray Bremsstrahlung Isochromat Spectroscopy

Chapter 1

Introduction

Materials with strongly correlated electrons exhibit a wealth of interesting and technologically valuable phenomena such as high-temperature superconductivity and colossal magneto-resistance. To fully unlock the potential of these materials for practical application, a comprehensive theory that can accurately predict their electronic structures is needed. Traditional theories in condensed matter physics generally treat materials in one of two limits: weakly correlated, which accurately describes itinerant systems like metals, or very strongly correlated, which describes localized systems like ionic compounds. The so-called strongly correlated materials lie mid-way between these two limits, a fact that makes them inherently interesting but also difficult to model. To develop a rigorous theory for this class of materials, a better understanding of strongly correlated electronic structures must be found through experiment. One deficiency that needs to be addressed is in our knowledge of their unoccupied states (electronic levels above the Fermi energy). Understanding the nature of these states, particularly how they depend on doping, is critical for testing the validity of new theories and to ultimately make progress in the field.

There are many experimental techniques for studying the unoccupied states, but inverse photoemission spectroscopy (IPES) stands out from the others due to its unrivaled capacity to resolve the momentum dependence of electronic structures [1, 2]. The modern form of IPES was developed in the 1970's and 1980's [3, 4], yet despite its enormous potential value to the study of strongly correlated materials, it has remained largely overlooked to the present day. Ironically, this is due in part to to the flurry of activity surrounding its sister technique, photoemission spectroscopy (PES),[1] which has dominated the attention of the field for the past two decades. Today, PES is widely regarded as the premiere method for

---

[1] Sometimes referred to as *direct* photoemission spectroscopy to explicitly distinguish it from IPES.

performing momentum-resolved studies of the occupied states, and the many advantages that it shares with IPES only bolsters the expectation that IPES could lead to important discoveries on the other side of the Fermi level.

The field of strongly correlated materials is now effectively wide-open for any experimentalist with the proper equipment and expertise to make significant progress examining the unoccupied states. This thesis describes a newly constructed, state-of-the-art, IPES spectrometer in the Hawthorn Group at the University of Waterloo that was built specifically for that purpose. To our knowledge, it is the only apparatus of its kind in Canada dedicated to strongly correlated materials, and one of only a handful currently operating in the world. The Hawthorn group has extensive experience studying strong correlations, particularly in the cuprate superconductors, and although the spectrometer is capable of measuring a wide variety of solid-state samples, it was designed specifically for the continued study of this class of materials.

Besides for the fulfilment of my degree, this thesis is also intended to serve as a record of the original design features of the spectrometer and important events surrounding its initial development. It is the hope that my work will be a valuable resource to future experimentalists working in our laboratory, especially new graduate students being trained in IPES. I have therefore included an overview of both the theoretical and experimental aspects of the IPES technique in Chapter 2, as well as a review of various aspects of ultra-high vacuum (UHV) science throughout the text and in Appendix A. The reader may find the latter review beneficial to understand the reasoning behind various design choices outlined in Chapter 3, where the spectrometer and its many auxiliary components are described. The ultraviolet photodetectors required a particularly large amount of time to design and build. Their description is therefore reserved to Chapter 4 where a more in-depth analysis can be provided. Following the main body, the appendices then contain a multitude of information regarding various aspects of the spectrometer that the reader may find helpful or interesting.

Chapter 2

Inverse Photoemission Spectroscopy

Inverse photoemission spectroscopy (IPES) is, in some sense, the reverse of the popular technique of photoemission spectroscopy (PES) (see Ref. [5]). In PES, a beam of photons is shone onto a material to eject electrons via the process of photoabsorption. By collecting the electrons and examining their properties, information about the quantum states they started in, known as the occupied states, can be determined. In IPES, a beam of electrons is injected into a material to induce the emission of photons. This happens after the injected electrons spontaneously decay into the ground state of the material's electronic structure, and therefore measuring the emitted photons provides information about the so-called unoccupied states that they passed through. The complementarity of the two techniques is summarized in Table 2.1.

The experimental setup for IPES is relatively simple (Figure 2.1). It consists of an electron gun and a photon detector pointed toward a sample material. Ideally, the electron gun fires a well-defined, monoenergetic beam with energy around 10 eV (see Section 2.2). The penetration depth for electrons at this energy is very short, on the order of 10 Å [6], and therefore surface effects in the material cannot be neglected. Arguably the most important of these effects is the presence of adsorbed gas particles, which can be minimized by conducting the experiment in ultra-high vacuum (see Appendix A).

Technique	Particles In	Particles Out	Information Obtained
PES	Photons	Electrons	Occupied States
IPES	Electrons	Photons	Unoccupied States

Table 2.1: Conceptual comparison of IPES and PES.

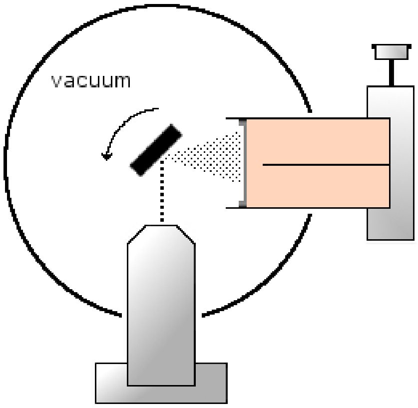

Figure 2.1: Schematic diagram of an IPES experiment. A low-energy electron gun (bottom) fires electrons into the sample (center), causing it to emit photons that are detected by a Geiger-Müller-style photodetector (right). For angle-resolved studies, the sample can be rotated.

2.1 The Energetics of IPES

The basic physical process behind IPES is illustrated in Figure 2.2. When an electron reaches the sample from the electron gun, its energy is conserved as it couples into an unbound quantum state above the vacuum level, labelled $|i\rangle$. Clearly, the system in this configuration is energetically unstable, and the electron will quickly decay into an unoccupied state $|f\rangle$ of lower energy. There are multiple mechanisms by which it can do so, one of which is through the emission of a photon of energy $h\nu$. With knowledge of the incoming electron's energy E_{e^-}, detection of the photon easily provides the energy of the final state $|f\rangle$ through the relation

$$E_{|f\rangle} = E_{\mathrm{e}^-} - h\nu. \tag{2.1}$$

It is the purpose of an IPES experiment to determine the energies of all of the bound unoccupied states, or in other words find the $\mathrm{E}_{|f\rangle}$'s.

2.1.1 Modes of Photon Detection

There are two procedures available that can be used to discover the $E_{|f\rangle}$'s. The first is to hold the electron beam at a constant energy, $E_{\mathrm{e}^-} = E_0$, while detecting the full range of emitted photons. The resulting spectrum will peak whenever

$$h\nu = E_0 - E_{|f\rangle}. \tag{2.2}$$

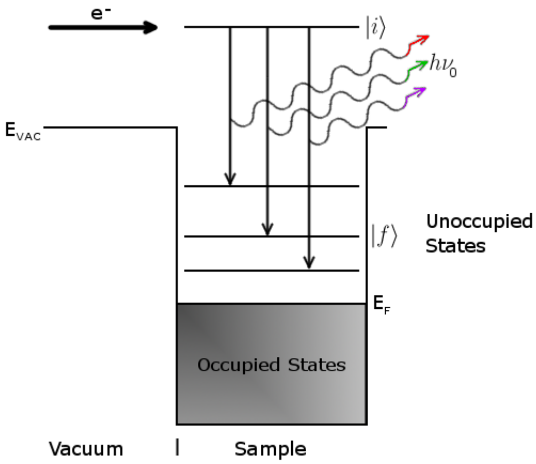

Figure 2.2: Schematic representation of the IPES process. A free electron from the vacuum passes into the sample and couples to unoccupied state $|i\rangle$. It then decays into a lower-energy unoccupied state, possibly releasing a photon in the process. In isochromat mode, photons with energy $h\nu_0$, green in the diagram, are detected. With the initial energy shown in the diagram, information about state $|f\rangle$ can be determined.

Alternatively, the energy of the electron beam can be varied while only one photon energy, $h\nu_0$, is measured. The intensity of the collected photons will then peak whenever

$$E_{e^-} = h\nu_0 + E_{|f\rangle}. \tag{2.3}$$

The latter method is known as isochromat mode, to reflect the fact that only one photon frequency is detected, and the former is known as spectrograph mode.

In spectrograph mode, measurements are performed with a grating spectrograph (or sometimes a lens spectrograph), which requires passing the photons emitted from the sample through an optically dispersive medium to separate their wavelengths before detection with a wide-band photodetector, such as a microchannel plate [2, 7]. In one possible configuration, many detectors are spread along the plane of diffraction, such that each detector measures only a narrow energy range. An alternative method is to use only a single detector and allow the dispersive element to rotate such that the full range of the spectrum can be swept across the detector. Whichever configuration is chosen, the spectrograph will necessarily require significant space for the optics, detectors, and motors, which in a vacuum system implies additional technological challenges and costs. Furthermore, the large distance between the detector(s) and the sample, as well as the narrow collection angle through which the photons must pass to be properly diffracted onto a detector, usually results in count rates much lower than in isochromat mode.

For practical reasons, isochromat mode is simpler to implement and more commonly practiced in recent experiments [8–14]. It's one disadvantage compared to spectrograph mode is its requirement of a photodetector that measures only a narrow window of energies. Overall, the best choice for such a detector is one based on a Geiger-Müller (GM) tube (see Chapter 4), which has a typical resolution of a few hundred meV. A spectrograph, on the other hand, can achieve resolution below 100 meV [15]. However, GM-style photodetectors are cheaper and simpler to install on a vacuum system, and they also boast a wide collection angle and high quantum efficiency. These last two properties reduce collection times which, as described in Section 2.3.2, is a great advantage when performing IPES. The isochromat mode was chosen for our IPES spectrometer, and it will be assumed for all subsequent discussions in this thesis.

2.1.2 The Fermi Energy

In IPES, we wish to determine the energy of an unoccupied state relative to the sample's Fermi energy $E_F^{(s)}$, and therefore we must determine the energy of the incoming electron E_{e^-} using the same reference. In practice, the energy of the electron beam is selected by setting the potential of the electron gun's cathode, V_g:

$$E_{\mathrm{e}^-} = eV_g + \Phi_g, \tag{2.4}$$

where Φ_g is the cathode's work function (see Figure 2.7). However, Φ_g is usually unknown, and V_g is known only to a modest precision,[1] making the calculation of E_{e^-} difficult. Luckily, E_{e^-} can instead be determined quickly and easily through experiment.

When the electron gun's cathode is grounded, the electron beam will have an energy of approximately Φ_g, which for most materials is no more than about 5 eV. Typical GM photodetectors used for IPES are sensitive to photons with energy $h\nu_0 \simeq 10$ eV (see Section 2.2), and therefore it will be impossible for any photons to be detected.[2] As the cathode's voltage is increased, the first detectable photons will be produced when the beam's energy is greater than the sample's Fermi energy by exactly the energy of a photon:

$$E_{\mathrm{e}^-}^{(F)} = E_F^{(s)} + h\nu_0. \tag{2.5}$$

---

[1] V_g must also be known relative to the potential of the sample, which is grounded in a typical IPES experiment. The gun's controller reports V_g relative to ground, but since there are often small offsets between grounds that are physically separated around a vacuum system, the two grounds may not actually be the same. Thus, determining a precise value of V_g can be nontrivial.

[2] It is assumed that the sample is also grounded.

The minimum cathode voltage for which counts can be detected therefore corresponds to the energy of the electron beam that probes $E_{|f\rangle} = 0$, or equivalently $E_{\mathrm{e}^-} = h\nu_0$, both relative to the sample's Fermi energy. Furthermore, since E_{e^-} grows linearly with V_g, unoccupied states of all energies can be probed without requiring knowledge of Φ_g.[1]

The procedure just described for calibrating the electron beam's energy has the caveat that the sample material must have an unoccupied state, which is to say a finite density of states, at its Fermi level into which electrons from the beam can decay. If the material has a band gap across its Fermi level, then performing the above procedure will instead only reveal the lowest-energy unoccupied state, whose relation to the Fermi level may not be known. To avoid this problem, the sample can be placed in electrical contact with a second sample that is made of a material with an easily detected Fermi level. In thermodynamic equilibrium, the Fermi level in the two samples will at the same energy [16]. Thus, performing the above procedure on the second sample will in essence determine the Fermi level of the first. Our spectrometer is setup to use a polycrystalline gold sample for this purpose, which is a well-behaved metal and thus has a very easily distinguished Fermi level. For more details, see Chapter 3.

2.2 Angle-Resolved IPES

For single crystal samples, the electronic states of course do not depend only on energy as in Figure 2.2, but also momentum. Therefore, in order to measure all of the unoccupied states in a material, it must be possible to vary the momentum of the incoming electron beam. This is accomplished by controlling the orientation of the electron beam relative to the crystallographic axes of the sample. When IPES is performed in this way to map-out the momentum characteristics of a material's band structure, it is semantically distinguished from its momentum-integrated counterpart and referred to as angle-resolved inverse photoemission spectroscopy (ARIPES).[2]

Since there is virtually infinite translational periodicity in the crystal's lattice structure along directions parallel to its surface, the component of the incident electron's momentum along this direction, $\vec{k}_{\parallel}$, serves as a good quantum number [6] and is conserved when the electron enters the sample and couples into state $|i\rangle$. During the radiative transition

---

[1] For example, if a peak is found when E_{e^-} is 2 eV above $E_{\mathrm{e}^-}^{(F)}$, then there is an unoccupied state 2 eV above the sample's Fermi level.

[2] Another common name is k-resolved inverse photoemission spectroscopy (KRIPES).

from $|i\rangle$ to $|f\rangle$, the electron's total momentum is conserved,[1] and therefore state $|f\rangle$ must also have the same parallel momentum as the incident electron [17]. In other words, a peak in an ARIPES spectrum corresponds to an unoccupied state with energy dictated by Equation (2.3) and parallel momentum the same as that of the incident electron.

Figure 2.3 illustrates how the incident electron's parallel momentum can be controlled when measuring a sample. The magnitude of the electron's total momentum just before it reaches the sample is given by the free-electron relation

$$k = \frac{\sqrt{2m_\mathrm{e}E_k}}{\hbar}, \tag{2.6}$$

where E_k is its kinetic energy. Therefore, the magnitude of its momentum parallel to the sample surface is dictated by the angle between the electron beam and the surface normal according to

$$\begin{aligned} k_\parallel &= k\sin\theta \\ &= \frac{\sqrt{2m_\mathrm{e}E_k}}{\hbar}\sin\theta, \end{aligned} \tag{2.7}$$

with components along the surface's crystallographic axes

$$\begin{aligned} k_a =& k_\parallel \cos\phi \\ =& \frac{\sqrt{2m_\mathrm{e}E_k}}{\hbar}\sin\theta\cos\phi \end{aligned} \tag{2.8}$$

and

$$k_b = \frac{\sqrt{2m_\mathrm{e}E_k}}{\hbar}\sin\theta\sin\phi. \tag{2.9}$$

Thus, the parallel momentum of the unoccupied state $|f\rangle$ can be selected simply by adjusting the angles θ and ϕ.

2.2.1 ARIPES on Materials with 2D Densities of States

As an example, consider a sample material with a quasi-2D density of states. In such a material, the electronic band structure depends on two components of the electron's

---

[1] More specifically, the incident electron gives up some of its momentum to the emitted photon upon its transition to state $|f\rangle$. Therefore, momentum is of course conserved, but after the transition it is distributed between the electron and the photon. However, for electrons with energy ~ 10 eV, the photon's momentum is negligible, and often the momentum of state $|f\rangle$ is considered equal to the momentum of state $|i\rangle$.

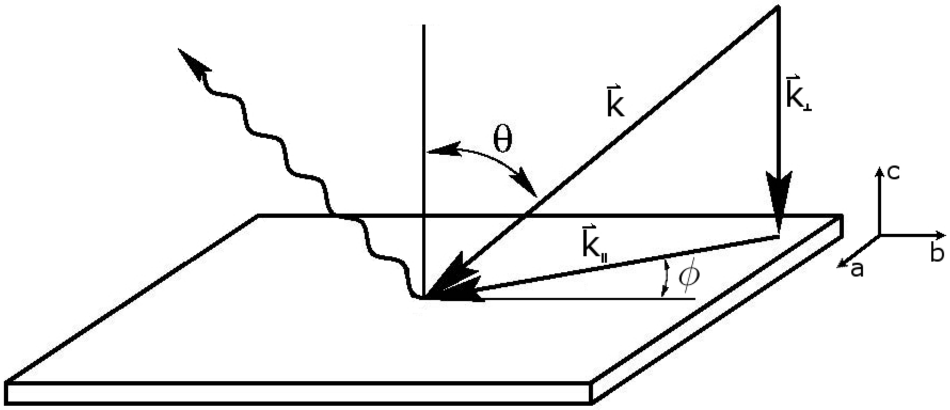

Figure 2.3: Schematic of an ARIPES experimental setup. The incident electron arrives with momentum $\vec{k}$, which can be separated into components $\vec{k}_\parallel$ and $\vec{k}_\perp$. The orientation of the crystallographic axes a, b, and c relative to the electron's momentum can be set by varying angles ϕ and θ. Drawing adapted from Ref. [18].

momentum, but is essentially independent of the third. The cuprate superconductors, which our group intends to study using ARIPES, can exhibit this kind of behaviour where the density of states is an explicit function of $\vec{k}_a$ and $\vec{k}_b$,

$$\rho = \rho(\vec{k}_a, \vec{k}_b), \tag{2.10}$$

but not $\vec{k}_c$. If the sample is oriented properly such that its independent momentum component is normal to its surface, then all of its unoccupied states can be studied by choosing appropriate values for $\vec{k}_\parallel$. This corresponds to a crystal surface with the c-axis normal to the plane as in Figure 2.3 so that the values of $\vec{k}_a$ and $\vec{k}_b$ can be completely determined by ϕ and θ. In a typical experiment, ϕ would be fixed such that the sample's a and b axes are rotated to some desired angle relative to the electron beam, and then θ would be varied while the number of emitted photons are recorded as a function of the energy of the incident electrons. The resulting spectrum would provide information about a slice of the sample's unoccupied density of states. By repeating this procedure for multiple angles of ϕ, many slices would be obtained and the entire unoccupied density of states could be systematically revealed.

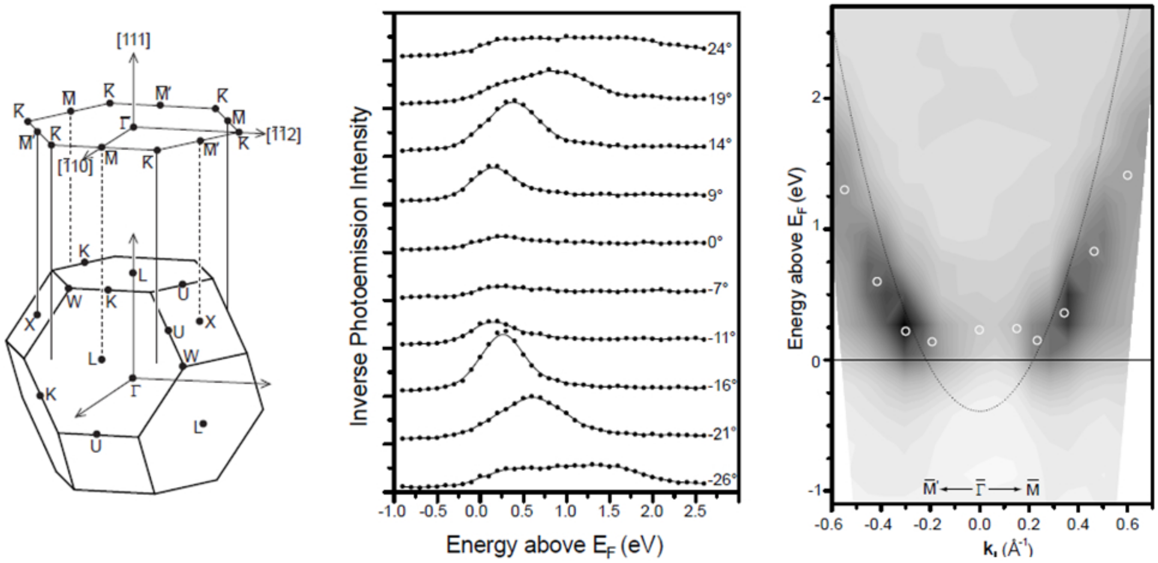

Figure 2.4: Example ARIPES spectra of a Cu(111) surface taken from Ref. [14]. Left: The Brillouin zone of copper showing the (111) plane. Center: ARIPES spectra taken with different values of θ. Right: The ARIPES spectra combined into a heat map plotted as a function of $E_{|f\rangle}$ and $k_{\parallel}$.

2.2.2 Example ARIPES on Cu(111)

Figure 2.4 shows a series of spectra on the (111) surface of a single crystal of copper taken using the ARIPES spectrometer at Queen's University [14]. The crystal's azimuthal angle ϕ was oriented so that the data reveals a slice of the Brillouin zone through the plane parallel to the [111] direction and the line from Γ to $\bar{M}$. In other words, $\theta = 0°$ corresponds to the [111] direction, and $\theta = 90°$ corresponds to $\bar{M}$. The peak is due to an unoccupied Shockley surface band. Like all surface bands, it is two-dimensional and thus can be mapped completely by scanning over ϕ and θ as described in the previous section. The movement of the peak with θ demonstrates the dependence of the band on $k_{\parallel}$. This is clearly shown in the heat map, where the curvature of the band can be seen directly. The energy dependence of the band as a function of momentum is known as the band's dispersion, and it is often an important parameter in many theories of condensed matter physics.

2.2.3 ARIPES on Materials with 3D Densities of States

The component of the incident electron's momentum perpendicular to the crystal surface, $\vec{k}_\perp$, is not necessarily conserved when the electron couples into state $|i\rangle$ [6,17]. This is due to the fact that the extent of the crystal in the perpendicular dimension that is accessible to the electron is dictated by the electron's short penetration depth. There is thus very limited translational symmetry, and $\vec{k}_\perp$ does not act as an effective quantum number. As a consequence, $\vec{k}_\perp$ of the state being probed cannot be directly controlled by the experimenter, and in fact will usually be unknown without prior knowledge of the material's unoccupied band structure. For materials whose band structures do not depend on $\vec{k}_\perp$ such as described in the previous section, this is unimportant. However, the band structure of many materials depends explicitly on all three components of an electron's momentum,

$$\rho = \rho(\vec{k}_a, \vec{k}_b, \vec{k}_c), \tag{2.11}$$

and this property of ARIPES must be taken into account.

As an example, consider a hypothetical material with a 3D density of states that is again oriented as in Figure 2.3. The experimenter can set $\vec{k}_a$ and $\vec{k}_b$ by adjusting ϕ and θ, but the $\vec{k}_c$ value of the state into which the incident electron couples, $|i\rangle$, will be determined by the details of the material's band structure. Figure 2.5 shows several slices of a possible electronic structure for such a material. In each slice, $\vec{k}_\parallel$ is fixed to a different value, which implies the crystal is in a different orientation relative to the electron beam. When an incident electron enters the sample, it will take on whatever value of $\vec{k}_\perp$ ($\vec{k}_c$) it must to couple into an unoccupied state and conserve its energy. If the experimenter has set the electron beam to have the energy represented by the dotted line in the left frame, then the incident electron will couple into the state where the dotted and solid lines intersect.

2.2.4 ARIPES Spectra of 3D Bands

Figure 2.6 shows an example band structure for a fixed $\vec{k}_\parallel$ in a hypothetical material with a 3D density of states and the (idealized) ARIPES spectrum that it might produce. A peak occurs in the spectrum wherever two bands are separated by the particular photon energy that the GM tube can detect.[1] As the energy of the incident electron beam is increased from zero, transition 1 appears first in the spectrum when E_{e^-} is at the top of

---

[1] The transitions shown in Figure 2.6 assume that all radiative transitions between unoccupied bands are allowed. In reality, the transitions between certain bands may be forbidden on symmetry grounds, much the same way as is found for certain transitions between electron orbitals around an atom.

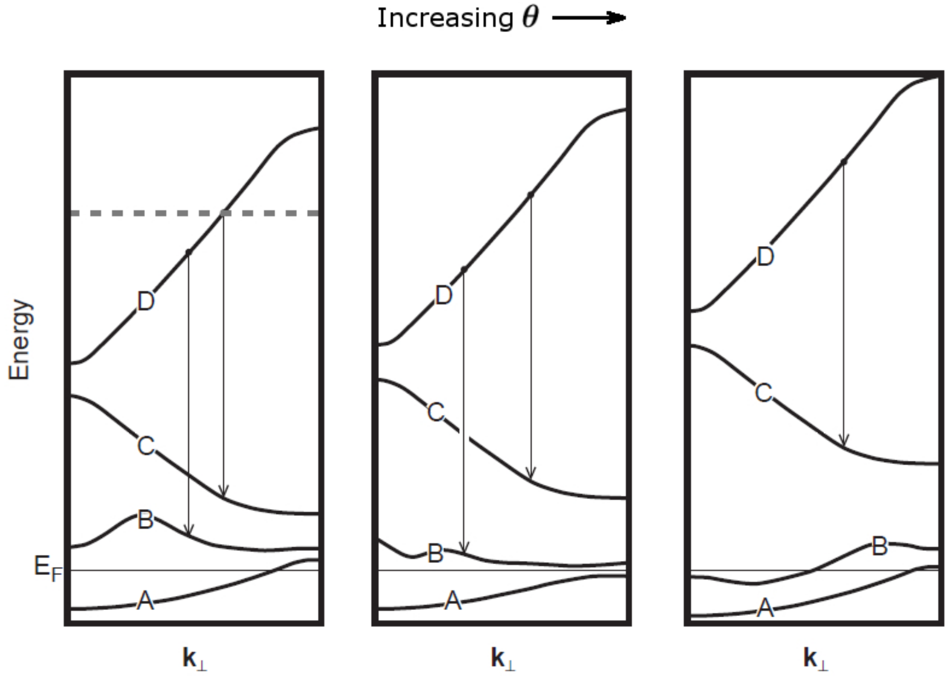

Figure 2.5: Three "slices" of a hypothetical material's band structure, each for a different fixed value of $\vec{k}_\parallel$. Vertical lines indicate radiative transitions that emit photons with detectable energy. If an electron is injected with $\vec{k}_\parallel$ corresponding to the left slice and with energy indicated by the dotted line, it will couple into the state with $k_\perp$ where the dotted and solid lines intersect. Since this state is at the top of an arrow, this will generate a peak in the ARIPES spectrum. Drawing adapted from Ref. [14].

corresponding arrow 1. Peak 2 appears shortly after since transition 2 begins at only a slightly higher energy, and then peak 3 shows up later on. A feature to make note of is the onset of counts when $E_{e^-} - h\nu_0$ exceeds the Fermi energy, E_F. This occurs in many materials, such as metals [14, 19], despite the lack of any apparently available transitions. The cause of this phenomenon is not fully understood, but is generally considered to be a surface effect and does not alter the measurement of the bulk band structure. Another interesting feature is the climbing background, whose origin lies with inelastic collisions. The incident electron can interact with the material through a variety of non-radiative processes that exchange energy and momentum.[1] In simple terms, this causes the electron

---

[1] There is a high probability of electrons interacting with the sample material via non-radiative electron-electron and electron-lattice processes that involve phonons and plasmons. This is the reason why the penetration depth of electrons at low energies is so small [2, 6]. In fact, the probability of non-radiative

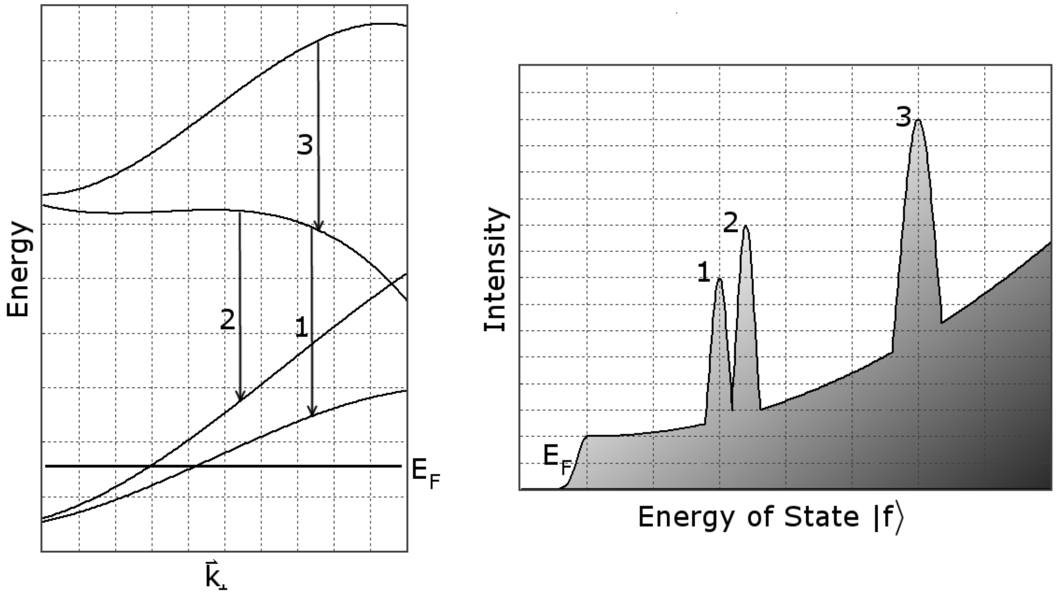

Figure 2.6: Left: Band structure for a fixed $\vec{k}_{\|}$ of a hypothetical material showing three possible transitions that will emit a detectable photon. Levels below the Fermi energy E_F are occupied and thus inaccessible. Right: Idealized ARIPES spectrum for the given band structure. Peaks correspond to the indicated radiative transitions. Note the increasing inelastic background.

to decay down through the band structure by tracing out the curves shown in the figure. Eventually, the electron will come to the top of one of the transition arrows and may fall down it to emit a photon. The detector will erroneously assume that photon came from a $E_{\mathrm{e}^-} \rightarrow E_{\mathrm{e}^-} - h\nu_0$ transition, when in fact it has no predictable relation to E_{e^-}. The higher the energy of the electron beam, the more possible paths exist for this to happen, and the higher the rate of erroneous background counts. One might expect the background to undergo a step increase at every peak, but in practice the background is rarely so well behaved [2,6,14,18]. Many factors, such as adsorbed molecules on the sample surface, can give the background spectrum complex structure.

The shape of an ARIPES spectrum can be described by [2]

$$N(E, h\nu_0) \sim \sum_{i,f} \int c_i \,|\, \langle i|\, \vec{p}\, |f\rangle \cdot \vec{A}|^2 \, \delta(E_i - E_f - h\nu_0)\delta(E - E_f) d\vec{k}, \qquad (2.12)$$

---

decay is generally much higher than radiative, and so the ratio of electrons-in to photons-out can be very large.

where N is the intensity of the emitted photons, E is the energy of interest (the abscissa in Figure 2.6), $\vec{p}$ is the quantum operator for momentum, $\vec{A}$ is the magnetic vector potential, and c_i is the probability that the incident electron will couple into state $|i\rangle$. The exact expression for N differs from Equation (2.12) by geometrical considerations only and provides little additional information about the material under study. In addition, its explicit derivation is beyond the scope of this thesis and will not be given. However, the functional form of Equation (2.12) is clearly consistent with the description of ARIPES just given, and the astute reader may recognize its similarities with the analogous form associated with angle-resolved PES. For further reading, we recommend Ref. [20].

2.2.5 Determining the Kinetic Energy of the Incident Electron

Regardless of the nature of a material's band structure, understanding the results of an ARIPES measurement requires calculating $\vec{k}$ according to Equation (2.6). Therefore, the kinetic energy of the incident electron, E_k, just before it enters the sample must be known. Note that $E_k \neq E_{e^-}$, but instead

$$E_k = E_{e^-} - \Phi_s, \tag{2.13}$$

where Φ_s is the work function of the sample (Figure 2.7). Substituting Equation (2.4), this becomes

$$E_k = eV_g + \Phi_g - \Phi_s. \tag{2.14}$$

As discussed earlier, the work functions Φ_g and Φ_s are typically not known, but they can be replaced in Equation (2.14) using the contact potential

$$\Delta = \Phi_s - \Phi_g \tag{2.15}$$

to obtain

$$E_k = eV_g - \Delta. \tag{2.16}$$

The contact potential is unique to every sample, as well as the particular crystallographic face being studied, but it is easily found through experiment. For more information about contact potential and how to measure it, see Appendix D.

2.2.6 ARIPES vs Momentum-Integrated IPES

In momentum-integrated IPES, a poorly defined electron beam with a wide momentum spread can be used, for example a bare, heated filament. Alternatively, a well-defined

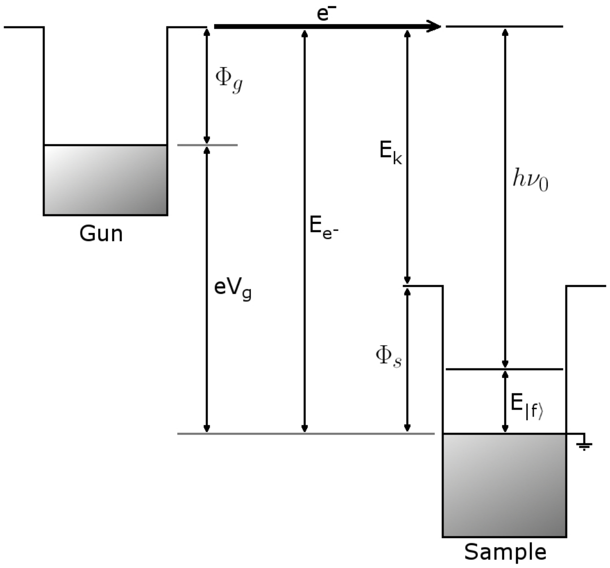

Figure 2.7: The energies involved in an IPES experiment. The kinetic energy of the incident electrons just before they couple into the sample, E_k, is used to determine the magnitude of the momentum, $\vec{k}$.

electron beam with very high energy is equally effective since, for even a small angular spread in its trajectories, the range of its electrons' $\vec{k}_{\|}$ can span the entire Brillouin zone [2]. The latter method is commonly practiced under the name X-ray BIS[1] since the detected photons are in the X-ray region. Using either electron source, the relaxation of $\vec{k}_{\perp}$ conservation then leads to the simultaneous probing of many momenta, and the resulting spectra resemble the total unoccupied density of states [6]. An ARIPES spectrum, on the other hand, is produced with a low-energy, narrowly spread electron beam and reveals the one-dimensional unoccupied density of states along a particular $\vec{k}_{\|}$ direction. It must be performed in the vacuum ultraviolet (VUV) region, instead of higher energies (which are easier to detect), to ensure a narrow spread in $\vec{k}_{\|}$. Our spectrometer is outfitted with such a low-energy gun and is intended to perform ARIPES exclusively.

---

[1] X-ray Bremsstrahlung Isochromat Spectroscopy

2.3 Some Theoretical Considerations

2.3.1 The Emission Cross Section

We follow the approach presented by Johnson and Davenport [21], which is equivalent to the original work done by Pendry [1]. The Hamiltonian describing the interaction between a photon and electron, neglecting spin, is given by

$$H' = \frac{e}{2m_{\mathrm{e}}c}\left(\vec{A}\cdot\vec{p} + \vec{p}\cdot\vec{A}\right) + \frac{e^2}{2m_{\mathrm{e}}c^2}|\vec{A}|^2, \tag{2.17}$$

where $\vec{A}$ is the photon's magnetic vector potential and $\vec{p}$ is the electron's momentum, both quantum operators in this case.

It is interesting to note that for PES, the quantum $\vec{A}$ can be replaced with a classical time-dependent perturbation without changing the results [2]. For IPES, however, a full quantum treatment is required since the spontaneous emission of a photon requires an electromagnetic field with a non-vanishing ground state. Therefore, we have [22]

$$\vec{A}(\vec{x},t) = \frac{2\pi}{\sqrt{V_{h\nu}}}\sum_{\vec{q}}\sum_{\alpha}\frac{\hbar c}{\omega}\left[a_{\vec{q},\alpha}(t)\hat{\boldsymbol{\epsilon}}^{(\alpha)}e^{i\vec{q}\cdot\vec{x}} + a^{\dagger}_{\vec{q},\alpha}(t)\hat{\boldsymbol{\epsilon}}^{(\alpha)}e^{-i\vec{q}\cdot\vec{x}}\right], \tag{2.18}$$

where the photon has wavevector $\vec{q}$, angular frequency ω, and polarization angle α. The photon's normalization volume is given by $V_{h\nu}$, and $\hat{\boldsymbol{\epsilon}}^{(\alpha)}$ is the linear polarization vector. The operators $a^{\dagger}_{\vec{q},\alpha}$ and $a_{\vec{q},\alpha}$ create and annihilate a photon in state $(\vec{q},\alpha)$, respectively, and c is the speed of light in vacuum.

The system has an initial state comprised of a free electron, $\psi_{\vec{k}}(\vec{r})$, and a final state with the electron bound to $\psi_b(\vec{r})$ after the production of a photon with momentum $\vec{q}$. We wish to determine the rate at which $|\psi_{\vec{k}}(\vec{r})\rangle$ will transition to $|\psi_b(\vec{r}),\vec{q}\rangle$. If we employ first-order time-dependent perturbation theory, wherein H' is the perturbing field, then the rate is given by Fermi's golden rule [23]:

$$W = \frac{2\pi}{\hbar}|\langle\psi_b(\vec{r}),\vec{q}|\,H'\,|\psi_{\vec{k}}(\vec{r})\rangle|^2\rho(E), \tag{2.19}$$

where $\rho(E)$ is the density of states for the photon with energy E. Since the photon is emitted into a vacuum, this is given by

$$\rho(E) = \frac{V_{h\nu}\omega^2}{8\pi^3\hbar c^3}d\Omega \tag{2.20}$$

for emission into solid angle $d\Omega$. Since we are working only to first order, we can neglect the term in Equation (2.17) containing $|\vec{A}|^2$, and thus the transition rate becomes

$$W = \frac{\omega e^2}{2\pi\hbar m_{\mathrm{e}}^2 c^3} \left|\langle\psi_b(\vec{r}), \vec{q}\,|\,\hat{\boldsymbol{\epsilon}}\cdot\vec{p}\,|\psi_{\vec{k}}(\vec{r})\rangle\right|^2 d\Omega. \tag{2.21}$$

The so-called transition cross section is defined as the transition rate per flux of injected electrons. For one electron, the flux is

$$\phi = \frac{\hbar|\vec{k}|}{m_{\mathrm{e}} V_{\mathrm{e}^-}}, \tag{2.22}$$

where V_{e^-} is the electron's normalization volume and m_{e} is the electronic mass. Dividing Equation (2.21) by (2.22), we find the change in cross section per steradian of photon emission to be

$$\frac{d\sigma}{d\Omega} = \frac{\omega e^2}{2\pi\hbar^2|\vec{k}|m_{\mathrm{e}}c^3} \left|\langle\psi_b(\vec{r}), \vec{q}\,|\,\hat{\boldsymbol{\epsilon}}\cdot\vec{p}\,|\psi_{\vec{k}}(\vec{r})\rangle\right|^2. \tag{2.23}$$

This quantity is related to the probability that a radiative transition will occur and emit a photon with momentum $\vec{q}$ when an electron with momentum $\vec{k}$ is absorbed by the material.

2.3.2 Comparison to PES

The above derivation can be repeated to find the cross section for PES. Using the emitted electron's density of states

$$\rho_{\mathrm{e}^-}(E) = \frac{m_{\mathrm{e}}|\vec{k}|V_{\mathrm{e}^-}}{8\pi^3\hbar^2}, \tag{2.24}$$

the transition rate is given by

$$W_{PES} = \frac{e^2|\vec{k}|}{16\pi^2 V_{h\nu}\hbar^3 m_{\mathrm{e}}c^2} \left|\langle\psi_{\vec{k}}(\vec{r})|\,\hat{\boldsymbol{\epsilon}}\cdot\vec{p}\,|\psi_{\mathrm{occ}}(\vec{r}), \vec{q}\rangle\right|^2 d\Omega, \tag{2.25}$$

where the initial state is now an electron in an occupied level below the Fermi energy and an incoming photon with momentum $\vec{q}$, and the final state is a free electron with momentum $\vec{k}$. Given a photon flux of

$$\phi_{h\nu} = \frac{\omega}{8\pi\hbar c V_{h\nu}}, \tag{2.26}$$

the cross section comes out to

$$\left(\frac{d\sigma}{d\Omega}\right)_{PES} = \frac{e^2|\vec{k}|}{2\pi\hbar^2\omega mc}\left|\langle\psi_{\vec{k}}(\vec{r})|\,\hat{\boldsymbol{\epsilon}}\cdot\vec{p}\,|\psi_{\mathrm{occ}}(\vec{r}),\vec{q}\rangle\right|^2 d\Omega. \tag{2.27}$$

The IPES and PES processes are often said to be the time-reverse of one another, in which case the square magnitudes of the matrix elements in Equations (2.23) and (2.27) would be the same. This is not strictly true, however. In PES, the emitted electron leaves behind a positively charged vacancy in the material. For IPES to be the time-reverse of PES, the incident electron in that process would have to fill in that vacancy when it is absorbed by the material, but of course it is implicitly assumed that the material begins electrically neutral. This caveat becomes important when comparing the two spectroscopies on small, localized systems such as individual molecules. For bulk structures, however, the addition or subtraction of a single electron is negligible, and the square of the matrix elements can be considered equal in this limit [2, 21]. With this in mind, we can compare the count rates for IPES and PES by taking the ratio of their cross sections:

$$\frac{\frac{d\sigma}{d\Omega}}{\left(\frac{d\sigma}{d\Omega}\right)_{PES}} = \frac{\omega^2}{c^2|\vec{k}|^2} \tag{2.28}$$

$$= \left(\frac{\lambda_{\mathrm{e}^-}}{\lambda_{h\nu}}\right)^2, \tag{2.29}$$

where λ_{e^-} and $\lambda_{h\nu}$ are the wavelengths of the incident electrons and photons, respectively.

For electron energies ~ 10 eV, the IPES cross section is $\simeq 2\times10^{-5}$ times as large as that for PES. At higher energies in the x-ray region, say ~ 1000 eV, the ratio reduces to $\simeq 2\times10^{-3}$. At either energy, this demonstrates that one should expect the count rates in an IPES experiment to be many orders of magnitude less than that in a comparable PES experiment. Since the count rates in PES are not considered exceptionally high, the expectation of low count rates must be incorporated into the designs an IPES spectrometer.

2.4 Vacuum Requirements

As stated earlier, IPES is performed using low-energy electrons with penetration depths on the order of Angstroms, and therefore IPES is very sensitive to the quality of the sample's surface. Ideally, the surface should be atomically ordered and smooth according to the crystallographic plane that is being examined, and no contaminating particles should be present. Preparing such a surface and maintaining it for enough time to complete a measurement requires the pristine environment of ultra-high vacuum (UHV).

When samples are initially loaded into our spectrometer, past exposure to the ambient environment has left their surfaces contaminated with adsorbed molecules, and sometimes even a thin layer of oxide. Therefore, samples must undergo in situ cleaning using the apparatus described in Section 3.4 before they can be measured. Immediately after the quality of a surface is restored, however, it will begin to degrade from exposure to the residual gas particles in the vacuum. An IPES spectrometer must thus be designed so that its vacua are of sufficient quality that measurements can be taken on a sample before contamination exceeds tolerable levels.

The flux per unit area of gas particles incident on a surface that originate from a solid angle $d\Omega$ at angle θ from the surface's normal is given, via the cosine law, by [24]

$$\begin{aligned}
\Phi &= \frac{n}{4\pi}\int d\Omega \int_0^\infty v\cos(\theta) f(v)dv && (2.30)\\
&= \frac{n\bar{v}}{4\pi}\int \cos(\theta)d\Omega && (2.31)\\
&= \frac{n\bar{v}}{4\pi}\int_0^{2\pi}\int_0^{\pi/2} \cos(\theta)\sin(\theta)d\phi && (2.32)\\
&= \frac{n\bar{v}}{4}, && (2.33)
\end{aligned}$$

where it is assumed that the velocities of the gas particles follow a Maxwell-Boltzmann distribution. For an ideal gas, such a distribution takes the form

$$\begin{aligned}
f &= \frac{1}{N}\frac{dN}{dv} && (2.34)\\
&= \frac{4}{\sqrt{\pi}}\left(\frac{m}{2kT}\right)^{3/2} v^2 e^{-mv^2/2kT}, && (2.35)
\end{aligned}$$

the arithmetic mean of which is the speed of the average gas particle:

$$\bar{v} = \sqrt{\frac{8kT}{m\pi}}. \tag{2.36}$$

Substituting Equation (2.36) (and Equation (A.15)) into (2.33), we get

$$\Phi = \frac{P}{\sqrt{2\pi mkT}}. \tag{2.37}$$

Equation (2.37) gives the number of gas particles impinging upon a sample surface per unit area per unit time as a function of pressure and temperature. To understand the rate of surface contamination, we must know what fraction of these particles "stick" to the surface (through adsorption, absorption, or chemical reaction) and how many potential sites there are for sticking to occur per unit area on the sample. Unfortunately, both of these parameters vary highly from sample to sample [25]. In fact, even samples with the same chemical composition that are supposed to be identical can differ in these respects due to microscopic flaws in their topography and chemistry. However, much can still be learned by using Equation (2.37) to estimate a worst-case contamination rate for a typical sample material.

We wish to estimate the amount of time it takes for a complete monolayer of contaminants to form on the surface of our sample. For simplicity, we assume that the first monolayer forms completely before the next one begins. We do not justify the validity of this assumption, but in general the surface will be intolerably contaminated after only a small fraction of the first monolayer forms. Therefore, any inaccuracy introduced by this assumption should be acceptable for our rough estimate. The fraction of the first monolayer that has formed after time t will thus be the flux, Φ, multiplied by the sticking coefficient, α, and divided by the number of sites at which contaminants can bind to the surface, η:

$$F(t) = \frac{\alpha P}{\eta\sqrt{2\pi m k T}} t. \tag{2.38}$$

For our worst-case estimate, we assume a sticking probability of $\alpha = 1$, i.e. every incident particle binds to the surface. Furthermore, we base the value of η on the properties of copper, a element of approximately average size that is commonly found in the materials our group intends to study. Copper has an atomic weight of ~ 64 g/mol and a density of ~ 9 g/cm^3 [26]. Assuming a simple cubic structure[1] and 1 binding site per atom on the sample's surface, that amounts to $\eta \sim 2 \times 10^{15}$ atoms/cm^2. Now if we assume the incident particles are H_2 ($m \approx 3.3 \times 10^{-24}$ g/atom), which is the most abundant species in UHV, and a temperature of 300 K, we find

$$F(t) \sim \frac{Pt}{1.35 \times 10^{-6}\ [\mathrm{Torr} \cdot \mathrm{s}]}, \tag{2.39}$$

or

$$t \sim \frac{1.35 \times 10^{-6}\ [\mathrm{Torr} \cdot \mathrm{s}]}{P} \tag{2.40}$$

---

[1] Since we are only interested in a rough estimate, we can do this to simplify the calculation.

seconds for a monolayer to form. Substituting values from Table A.1, we see that at the onset of HV around 10^{-3} Torr, it takes about 1 ms, and at the onset XHV at 10^{-12} Torr, it takes more than 15 days.

Note that this estimate is for the worst-case scenario and is a gross underestimation for typical materials. Specifically, the timescale will be longer for a real material since the density of binding sites is often larger than our estimate for η, a substantial fraction of the incident gasses will be at least an order of magnitude heavier than H_2, and most importantly α is often very close to zero [25].

Keeping everything else the same as above, but using the more realistic values of $\alpha = 10^{-5}$ and a contamination threshold of $F(t) = 1\%$ [25], then a pressure of 10^{-10} Torr, which is readily achievable in our spectrometer, provides almost 160 days of experimentation before a surface needs to be refreshed. This timescale is sufficiently long that we will be able to complete many IPES measurements on a single, continuous run without having to worry about sample contamination, and thus the efforts described in the next chapter to produce a clean vacuum environment are validated.

2.5 Further Reading

The theory of IPES, and the closely related theory of PES, is extensive and rigorous. To thoroughly analyze spectra extracted from a real experiment, an in-depth knowledge of one, or ideally both techniques is required, which we do not pretend to have exhaustively covered here. Often, the analysis involves subtle details that are inherent to the particular sample being measured, however, and thus it would neither be possible nor appropriate to include such details in this thesis, which intends to focus on the practical aspects of our IPES spectrometer. To delve deeper into the subject, we recommend Hüfner's textbook (Ref. [20]) as a starting point, followed by a literature review of the occupied and unoccupied states in the material(s) of interest.

Chapter 3

The Spectrometer

There are currently no complete IPES solutions available to be purchased commercially, and spectrometers, as well as their many supporting apparatus, need to be custom-designed and built for each research group's specific purposes. This chapter outlines the important design features of our spectrometer, the challenges we faced during construction, and the performance characteristics of the final product.

The design and construction of any sophisticated piece of scientific equipment is a complicated task with a plethora of small, but crucial, details that need to be taken into account. For the sake of concision, the following chapter outlines only the most important features of our spectrometer that should be of interest to the reader. More information is presented elsewhere in this thesis and other references. An important source of supplemental information is the wiki on our research group's website, as described in Appendix H. Additional technical drawings are presented in Appendix I, and a wealth of information can be found in the log books and manuals in our laboratory.

3.1 Overview

A scale model of the IPES spectrometer is shown in Figure 3.1, followed by a schematic in Figure 3.2. Components are organized into four major regions based on their function. Region 1 is the load-lock which houses all of the equipment involved with moving samples into and out of vacuum. Sample surface preparation takes place primarily in region 2, known as the preparation chamber,[1] while experimentation is performed in region 3, known as

---

[1] Manufactured by VG Scienta.

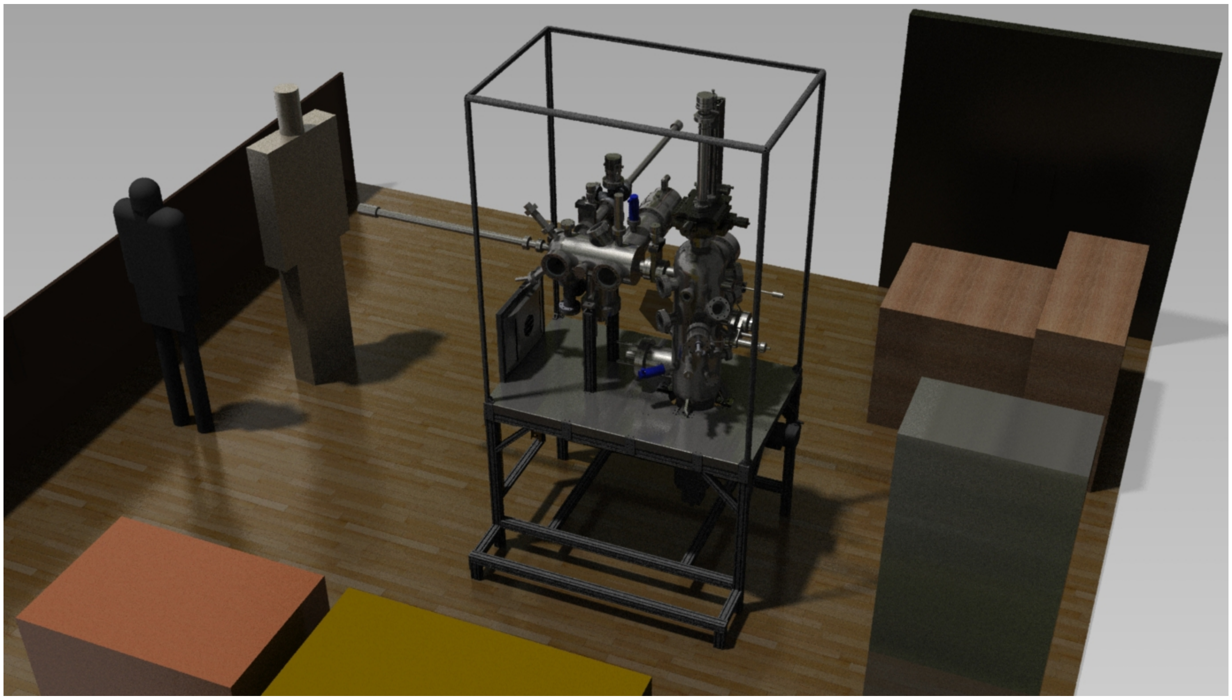

Figure 3.1: A three-dimensional scale model of the IPES spectrometer in our laboratory. Note the size relative to the experimenters on the left.

the IPES chamber.[1] Region 4 contains all other auxiliary components including structural supports, bakeout equipment, and control electronics.

3.2 Sample Holders

Our sample holders are based on the design employed at the RSXS endstation on the REIXS beamline of the Canadian Light Source synchrotron in Saskatoon [27], which in our experience is effective and robust against user errors. As shown in Figure 3.3, samples are mounted on a small rectangular plate of copper or aluminum using a UHV-compatible epoxy or tape (for example compounds, see Appendix C). Since the spectrometer will be used to study a wide variety of sample materials, we chose a simple design that permits the mounting procedure to be tailored to each particular sample and is able to accommodate unusual sizes, shapes, and other physical properties. Furthermore, this design maximizes

---

[1] Manufactured by VG Scienta.

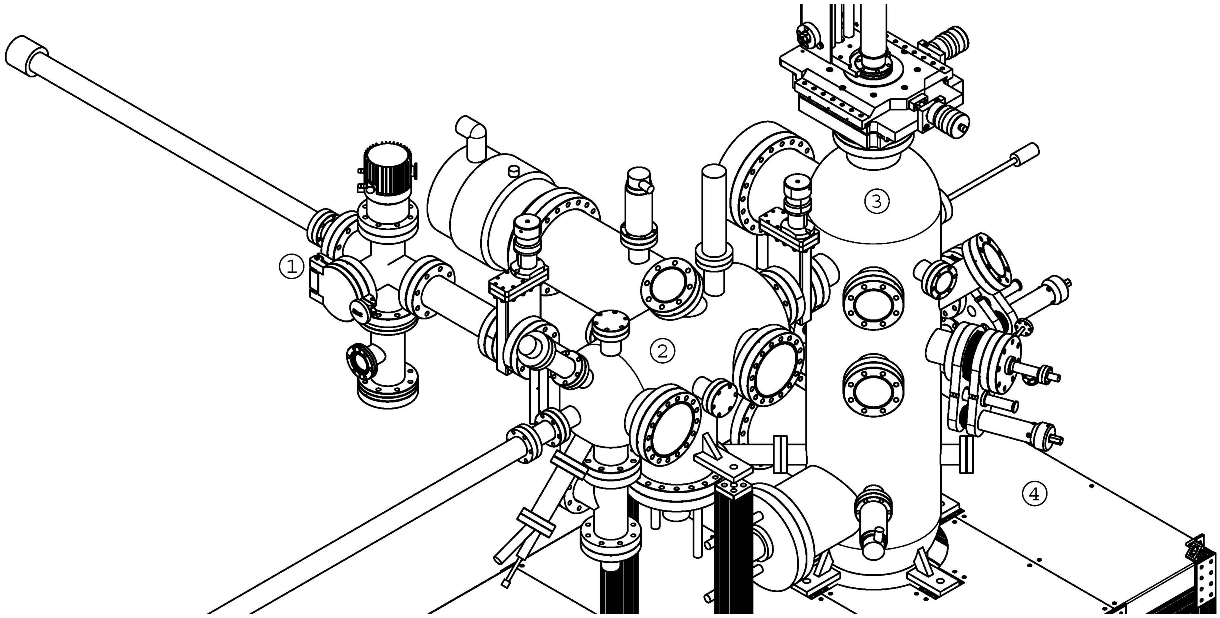

Figure 3.2: The IPES spectrometer, showing the load-lock (1), preparation chamber (2), IPES experimentation chamber (3), and support structure (4). Some components have been omitted for clarity, and not all components are exactly as shown.

the available viewing angle for our detectors and maintains a small surface area that, through frequent exposure to the external atmosphere, is likely to outgas and increase the pressure of the vacuum immediately surrounding the sample.

Another style of sample holder, also based on Ref. [27], that we designed for the spectrometer has the added ability to perform in situ azimuthal rotation. As illustrated in Figure 3.3, it is constructed by drilling a hole in the center of the standard sample holder's main plate, into which a plug is inserted. The plug is held in place via a lip that is sandwiched between the main plate and the smaller plate that screws onto the back. The smaller plate is fastened with significant pressure so that the plug is securely clamped and remains stationary under the typical forces encountered while moving through the spectrometer. However, when the user wishes to perform a rotation, the back plate can be loosened with an in-vacuum screwdriver (see Section 3.5). The back of the plug is outfitted with a fixed screw head that, using the same screwdriver, can then be rotated to reposition the plug before tightening the back plate again. The sample, which gets mounted to the flat face on top of the plug, can thus be manipulated with an additional degree of rotational freedom anytime during the experiment.

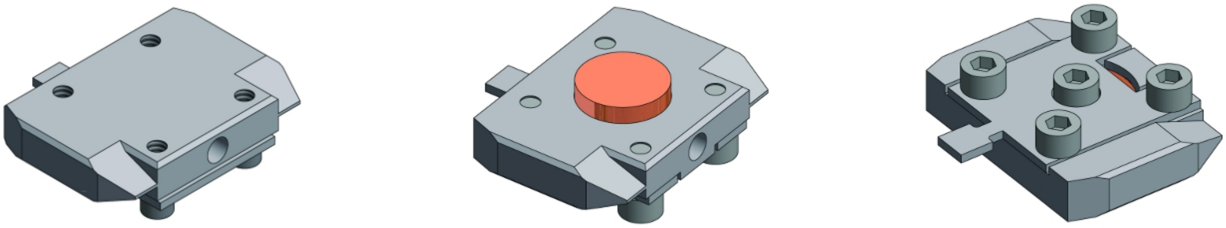

Figure 3.3: Left: Standard sample holder for the IPES spectrometer, shown here made out of Al. Center: Sample holder with added Cu plug that can be rotated azimuthally. Right: Underside of azimuthal holder showing how the bottom plate is connected. The plug is rotated by turning the center screw. A more detailed look at how the azimuthal holder is assembled can be found in Appendix I.

3.3 Load-Lock

For UHV apparatus, it is impractical to vent and then pump the system back down everytime a new sample needs to be examined. Therefore, our spectrometer is equipped with a load-lock (Figure 3.4) that can be isolated from the rest of the system with a gate valve[1] and brought up to atmospheric pressure for the insertion and removal of samples while the rest of the system remains under UHV. To minimize contamination from atmospheric adsorbents like H_2O, the load-lock can be vented to a slight overpressure with dry N_2 gas. That way, whenever it sits open to the air, there will be a small outward flow of gas that will reduce the amount of atmosphere that diffuses in. Furthermore, the N_2 will fill microscopic cracks and pores in the chamber walls where H_2O can otherwise collect [28]. The dry gas will also dissolve some of the H_2O that is adsorbed on the newly introduced samples and sample holders, reducing the amount that will ultimately be released into the other vacuum chambers.

Inside the load-lock, samples reside in a custom-built garage capable of storing up to four sample holders at one time. As shown in Figure 3.5, users insert sample holders into vertical slots by sliding them through the viewport door.[2] The slots are sufficiently loose so that the user can easily add and remove sample holders by hand, and a barrier exists in the bottom track close to the opening to stop holders from sliding out by mistake. The garage must also facilitate sample insertion and removal by a transfer arm (see Section 3.4) that has limited motion capabilities. The barrier was thus designed with a triangular shape that, in combination with the trimmed corners of the sample holder, allows the holder to

---

[1] MDC 302002, Kalrez o-ring

[2] MDC 665216, Viton o-ring

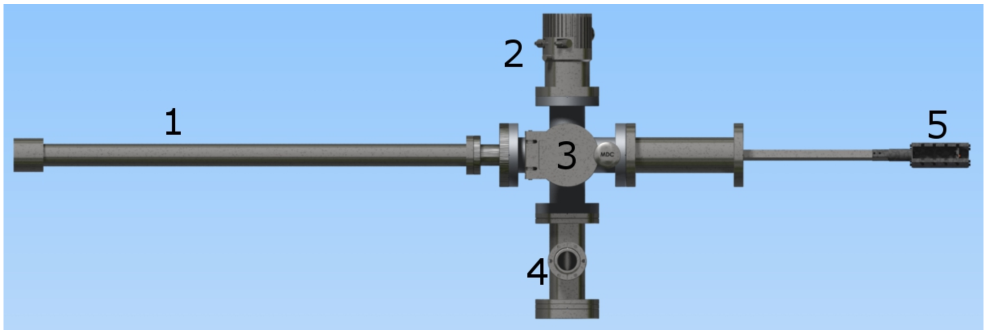

Figure 3.4: Schematic of the load-lock assembly. The transfer arm (1) translates the sample holder garage (5) from the viewport door (3) into the preparation chamber (as shown). The chamber is pumped using a turbo (2) backed by a scroll pump (not shown). Pressure is read by a gauge mounted on port (4).

easily “hop” over the barrier on its way in and out. A schematic of the garage can be found in Appendix I.

The ability to simultaneously store multiple samples under vacuum is of great benefit to the user. It saves time by reducing the frequency with which samples need to be moved in and out of the system. More importantly, though, it provides an exceptionally clean environment in which samples can be stored between measurements. Often, samples are stored in dessicators or containers filled with inert noble gasses, but still they are vulnerable to contamination, especially when exposed to air during transport to and from the spectrometer. In this scenario, samples need to be cleaned every time they are moved in and out of vacuum between measurements. By storing samples in the vacuum system, however, it can take days (or longer) after the initial surface preparation before samples need to to be re-cleaned.

The load-lock was designed to have a small volume and internal surface area so as to minimize pump down times for the convenience of the user. With it’s 80 L/s turbo,[1] which is backed by a dry scroll pump,[2] the pressure can fall from atmosphere to below 10^{-5} Torr within minutes, and below 10^{-8} Torr after a few hours. The exact time of course varies depending upon many factors, but it is substantially reduced if the chamber was vented with dry N_2. The pressure is read by a four-sensor gauge[3] that contains an ion gauge, conduction heat loss sensor, and two diaphragm sensors, which allows the pressure to be accurately reported all the way from atmosphere down to the lower range of UHV. The

---

[1] Pfeiffer HiPace 80

[2] Agilent SH-110 Dry Scroll Vacuum Pump

[3] Granville-Philips, Micro-Ion ATM, 390 Series

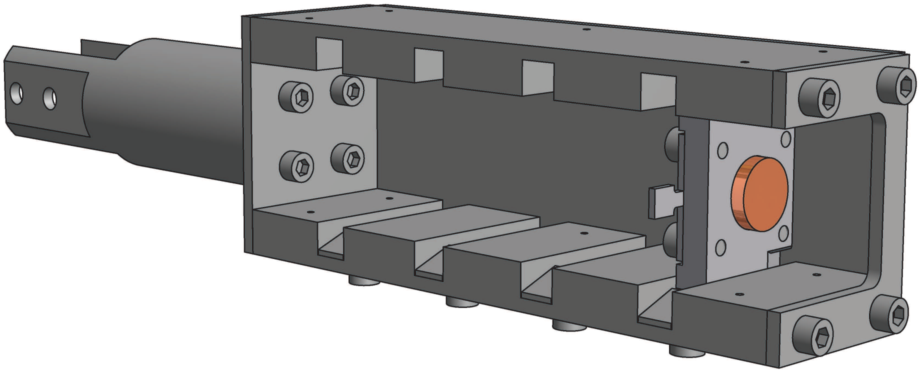

Figure 3.5: The load-lock garage. Up to four sample holders can be stored in vacuum simultaneously. Sample holders are inserted into the vertical slots, either by the user through the load-lock viewport door or by the transfer arm in the preparation chamber.

chamber is sealed by compressing the viewport door against a Viton o-ring. This system allows the user to open and close the door quickly and easily while still maintaining low leak rates that are compatible with UHV. After the samples are inserted and the load-lock is pumped down to an acceptable pressure, the gate valve can then be opened, and the garage, which is mounted on the end of a transfer arm,[1] can be moved into the surface preparation chamber.

3.4 Preparation Chamber

With the load-lock garage fully extended into the preparation chamber, a sample can be selected by means of a second transfer arm[2] set at 90° to the first. A set of pliers is mounted to the end of the arm that can be opened and closed by the user. As shown in Figure 3.7, a sample is picked up by closing the pliers onto the tab[3] at the rear of the sample holder. This is done by turning a magnetically-driven screw mechanism, which is robust against accidental loosening if the arm is jostled. The pliers also have a slot carved out on the inside of each jaw that the tab can slide into. Therefore, while the pliers are held closed, the tab is locked in place, and it is impossible for the sample to be dropped. Once it is picked up, the sample can then be translated down the length of the chamber, as well as

---

[1] Ferrovac GmbH RMDS40; linear motion only

[2] Ferrovac GmbH RMDG40 PGRMS(OMH); translation, rotation, and pincer grips

[3] Omicron-style tab

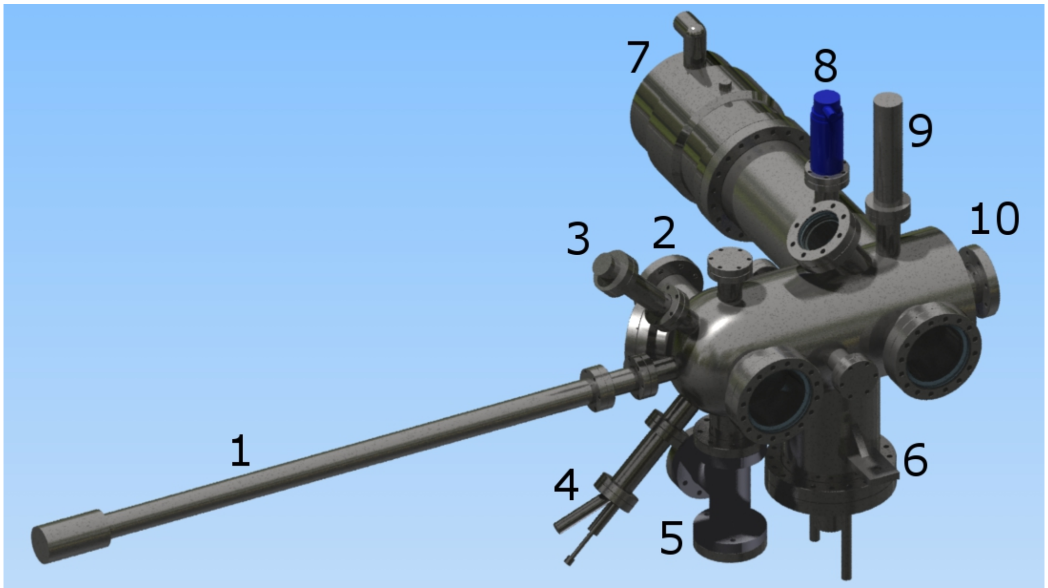

Figure 3.6: The surface preparation chamber showing the transfer arm (1), ion gun (3), K-cell (4), heater stage assembly (5), TSP (6), turbo (7), ion gauge (8), crystal cleaver (9), and ports leading to the load-lock (2) and IPES chamber (10). A detailed schematic can be found in Appendix I.

rotated about the central axis of the transfer arm, and properly positioned to utilize any of the surface preparation apparatus.

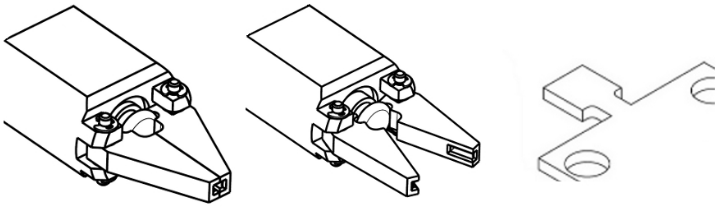

Figure 3.7: Left: Transfer arm pliers in the closed position. Center: Pliers fully opened. Right: Sample holder tab that fits into the slots carved out of each jaw. (Not to scale.) Drawing based on schematics given in Ref. [29].

3.4.1 Ion Gun

The preparation chamber is equipped with an ion gun[1] for the purpose of performing Ar^+-ion bombardment [30], also known as ion sputtering. The gun is composed of a heated filament held at a high voltage that emits high-velocity electrons. Argon gas is bled into the gun at a slow rate through a variable leak valve into the electron cloud. Some of the argon atoms will become positively ionized as a result of collisions with the electrons, at which point they are accelerated by another potential into an ion beam. When the beam reaches the sample, some of the ions will, through the acceptance of an electron, deposit their electrical potential energy and liberate one or more atoms off of the surface. In this way, the topmost atomic layer of the sample will slowly be removed to reveal the next-deepest, and presumably "cleaner," layer underneath. The process can be compared to using an extremely fine grade of sand paper on the sample that with each sweep removes a microscopic amount of the contaminated surface and reveals the clean material of the bulk.

It is useful to note the advantages of using argon for this technique over other gasses. First of all, argon has a high affinity for forming positive-ion/electron pairs, as opposed to positive-ion/negative-ion pairs that is favoured by many other gasses. This property helps the argon cloud undergo strong gas multiplication that greatly increases the beam's intensity. (Gas multiplication is explained in Chapter 4.) Another advantage of argon is its low sticking coefficient for almost all surfaces, a common property amongst the noble gasses. Pressure in the chamber is necessarily kept high during bombardment (often $\sim 10^{-6}$ Torr) to compensate for the inefficiency of ion production, and thus using a gas with a higher sticking coefficient could dirty the surface as fast as it is cleaned. Similarly, argon's low sticking coefficient, combined with a relatively high mass, ensures that the gas can be quickly pumped out of the chamber again after the ion bombardment is finished.[2]

3.4.2 Heater Stage

After a sample surface has been cleaned by Ar^+-ion bombardment, it's topography will be rough on a microscopic scale. Borrowing the analogy used earlier, argon ions polish a surface in a conceptually similar manner as sandpaper and will therefore never leave a

---

[1] LK Technologies NGI3000

[2] For our setup, the argon is primarily removed by a turbo pump. Turbos are useful for this application since they generally have high pumping rates and compression ratios for argon. Our chamber pressure can drop by several orders of magnitude within minutes after a lengthy bombardment session, and completely recovers within a few hours.

surface perfectly smooth. This can be corrected, however, through the process of annealing [31], whereby a sample is heated to high temperature so that its most energetic atoms can temporarily break their lattice bonds. Atoms on the sample's surface, whom are held in place more weakly than atoms in the bulk, can then become mobile and start hopping from binding site to binding site. It is more energetically favourable for an atom to sit in a depression on the surface than on top of a peak since it will have more neighbours in close proximity with which to form bonds. With sufficient time, therefore, it is statistically likely that surface atoms will migrate off of peaks to fill in cracks and pores, thus creating an atomically smooth surface.

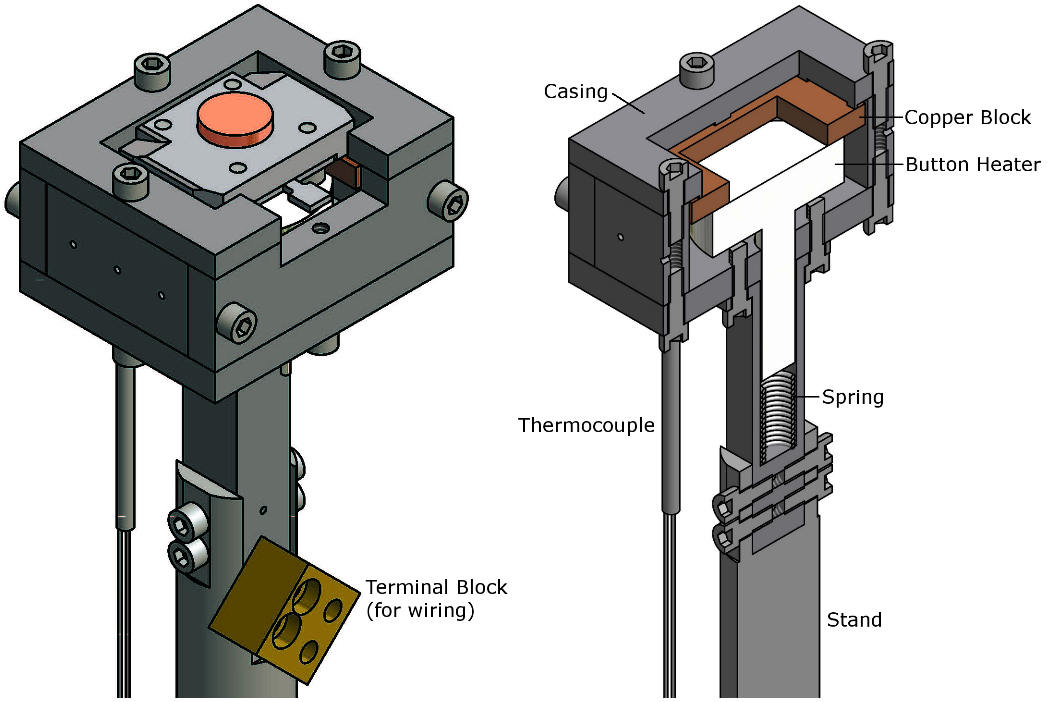

Figure 3.8: Heater stage for annealing or degassing samples and sample holders. Left: Outer view with sample holder. Right: Cut-away view showing internal components. The temperature is monitored through a thermocouple encased in ceramic (HeatWave Labs, Inc. 101689-06). Wiring not shown.

Heating can provide another benefit to surface preparation. Increasing the temperature of adsorbents on a surface increases their vapour pressure and encourages them to outgas. Therefore, although the pressure in the chamber will go up, heating will cause the density of contaminants on a sample to decrease. Effectively, the adsorbed particles migrate from the hot sample to the cooler walls of the chamber. Caution should be exercised, however, that if a sample is cooled while the chamber pressure is still raised, then adsorbents can condense back onto the surface and undo any potential cleaning effects. Heating the sample and keeping it hot until the chamber's pressure recovers to normal values can, however, be beneficial, especially for inert samples whose surfaces have not been chemically modified by the adsorbed gas.

To heat samples in our spectrometer, we constructed the heater stage depicted in Figure 3.8. In our design, a button heater[1] encased in molybdenum is pressed up hard via an underlying spring against a C-shaped block made of OFHC copper. The pressure between the components is intended to promote efficient heat conduction to the sample holder, which is placed on top of the copper. The assembly is surrounded by a stainless steel box that protects chamber walls from radiative heating and slows the spread of outgassing by the hot surfaces contained within it. We verified that the heater can achieve temperatures well above what we expect to require for our samples by using it to melt aluminum ($\approx$ 660°C).[2]

3.4.3 Knudsen Cell

The preparation chamber is also equipped with a Knudsen cell, or K-cell, that can be used for deposition (Figure 3.9). This component is not expected to be frequently used for surface preparation, although rudimentary thin films, such as polycrystalline metals, could potentially be grown. It is worth noting that, since the films would never have to leave vacuum between growth and measurement, they would have impeccably clean surfaces.

The primary reason that a K-cell was installed onto the spectrometer is so that it can be used to deposit a layer of polycrystalline gold onto a blank sample holder. The holder will be used to give a reference measurement for determining the sample's Fermi energy, as described in Section 2.1.2, as well as when determining the sample's contact potential, as described in Appendix D. In essence, the purpose of the holder is to ensure that the measured energies of the unoccupied states are referenced properly and are not reported with erroneous offsets.

---

[1] HeatWave Labs, Inc. 101138

[2] We were running initial tests on the heater using a sample holder that we thought had been assembled using titanium screws, which melt around 1670°C. You can imagine our surprise when the screws, which were actually made of aluminum, began to melt as we exceeded 650°C. Recall that aluminum, like many metals, sublimates as it approaches its melting point, and so it began depositing on the inside of our viewports!

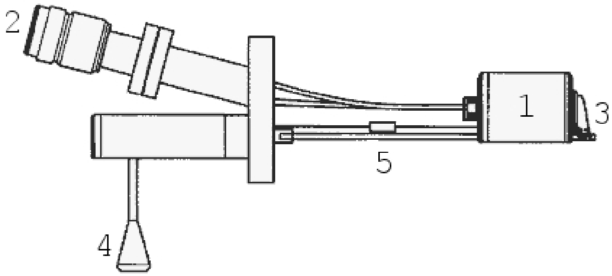

Figure 3.9: The Knudsen cell. The deposition material is inserted into the crucible (1) where it is heated close to its melting temperature by current supplied through the connector (2). When a high vapour pressure has been produced, the crucible door (3) can be opened with the handle (4) to start deposition. The crucible's outer casing is cooled with water lines to reduce outgassing (5) (connectors not shown). Some aspects are not to scale. Drawing is adapted from Ref. [32].

3.4.4 Quartz Crystal Monitor

A quartz crystal monitor (QCM) is used to determine the thickness, or more specifically the rate of growth, of thin films [33]. Quartz crystals are naturally piezoelectric, which means they produce a voltage when deformed, or alternatively deform when a voltage is applied to them. By applying an alternating electric field, one can therefore drive a quartz crystal to oscillate. However, if the frequency of the applied field differs from the crystal's natural resonance, then the crystal will resist the oscillation and produce its own field superimposed on top of the driving field. This can be measured and used to determine how far off of the resonance the driving field is. Of course, a resonance frequency is not unique to a particular crystal size, but instead is associated with a set of sizes that each correspond to a half-integer number of resonant wavelengths. Therefore, the exact size of the crystal cannot be determined from this information alone. However, if the resisting field is measured while a film is being deposited onto the crystal, then the crystal's resonant frequency will change, and the magnitude of the resisting field will oscillate as the driving field passes in and out of phase with resonance. Using this information, the rate at which the film is deposited can be determined.

Our QCM[1] (Figure 3.10) is used to determine the rate at which the K-cell deposits a film as a function of supplied current. As we only have plans to use the K-cell to deposit gold, and this only needs to be done on rare occasion, the QCM is usually left off of the system and re-installed as needed.

---

[1] Inficon, IPN 074-154

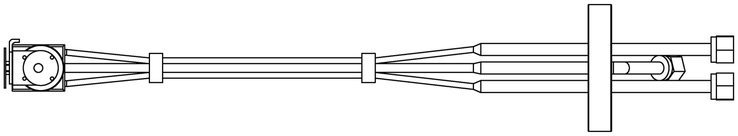

Figure 3.10: The quartz crystal monitor. The crystal is placed in the receptacle on the bottom of the apparatus (left in the diagram). Current is passed through the center connector. The other two connectors are for water cooling, which is required since deposited films are close to the melting temperature of the respective element(s).

3.4.5 Crystal Cleaver

The surface preparation technique that we intend to use most often involves a crystal cleaver[1] (Figure 3.11). The cleaver operates by pushing a blade through the sample that is placed up against an anvil. If the sample is positioned properly, the blade will slice off a thin layer to expose a fresh surface underneath. More specifically, the cleaver will cause the sample to undergo either cleaving or fracturing. When a sample is cleaved, it breaks along a natural plane of weakness. Many of the samples our group intends to study, such as the cuprate superconductors, have planes that are particularly weak and easy to cleave. Therefore, the blade acts more to peel off the top layer of the surface, rather than doing any real cutting. When a sample is fractured, on the other hand, there are no weak planes available, at least not corresponding to the sample's current orientation, and thus the blade must force its way through the crystal. Fractured surfaces are more likely to be rough microscopically, and thus can sometimes benefit from annealing.

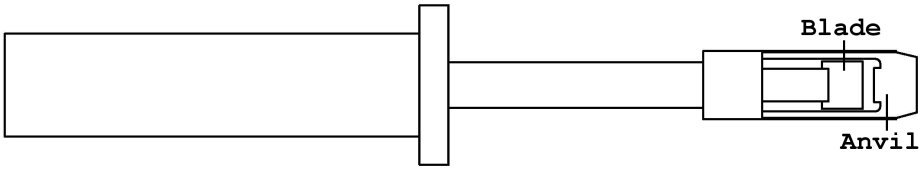

Figure 3.11: Crystal cleaver. The blade can be moved closer to and farther from the anvil by turning the handle.

3.4.6 Pumping System

The preparation chamber was designed to be pumped at relatively high speeds. As described in Sections 3.4.1 and 3.4.2, large gas loads can arise within the chamber, such as

---

[1] Kratos Analytical

argon from ion sputtering and outgassing from elevated temperatures, and they need to be quickly pumped out to keep sample surfaces clean and to keep the spectrometer under UHV. Furthermore, high pumping speeds help the preparation chamber serve as a barrier to stop high pressures and “sticky” gas species from passing from the load-lock to the IPES chamber.

The preparation chamber is pumped with a 750 L/s turbo[1] and a TSP,[2] and the chamber's ducts were designed with large diameters and short lengths to fully utilize the high speeds of these pumps. For example, the turbo is connected to the chamber through a duct $L \approx 325$ mm long and $d \approx 146$ mm in diameter. The conductance through this duct is given by [34]

$$C = \frac{d^3}{3L}\sqrt{\frac{\pi R_0 T}{2M}}, \tag{3.1}$$

where R_0 is the universal gas constant, T is temperature, and M is the molar mass of the gas species. This comes out to about 4470 L/s for H_2, the slowest species to pump. The turbo achieves 580 L/s for H_2 at its inlet [35], and thus from [34]

$$\frac{1}{S_{\mathrm{NET}}} = \frac{1}{S} + \frac{1}{C}, \tag{3.2}$$

where S is the speed of the pump and S_{NET} is the pumping speed in the chamber, the turbo will pump at about 513 L/s.

When backed by a scroll pump, which produces a backing pressure around 10^{-2} Torr, the turbo is specified to reach a base pressure[3] around 10^{-10} Torr [35]. However, from the contamination timescales given in Section 2.4, we wish to achieve operating pressures (which are often higher than the pump's base pressure) on the order of 10^{-11} Torr. The pump's limiting factor is its compression ratio for H_2, and so to reduce the pressure in the chamber, the partial pressure of hydrogen in the pump's exhaust line has to be reduced. We achieved this by backing the pump with a second, inexpensive turbo[4] (which is in turn backed by a rough pump) that reduces the pressure at the exhaust port of the chamber's turbo to around 10^{-5} Torr. Given a compression ratio of 2.5×10^6 [35], we expect the base pressure to now approach 10^{-13} Torr.

In practice, the 750 L/s turbo can easily maintain a chamber pressure below 10^{-10} Torr when the ion gun and heater stage are not active. Using the TSP, this pressure can be

---

[1] Agilent Turbo-V 750 TwisTorr

[2] Gamma Vacuum

[3] At the inlet of the pump when attached to a standard, stainless steel UHV chamber.

[4] Agilent TPS-Compact Turbocart

reduced substantially. When the TSP is optimized for efficient titanium consumption, we have recorded pressures as low as 1.7×10^{-11} Torr,[1] but if we were to increase the rate of TSP regeneration, it would pump more aggressively and potentially lower this pressure even further.

3.5 IPES Chamber

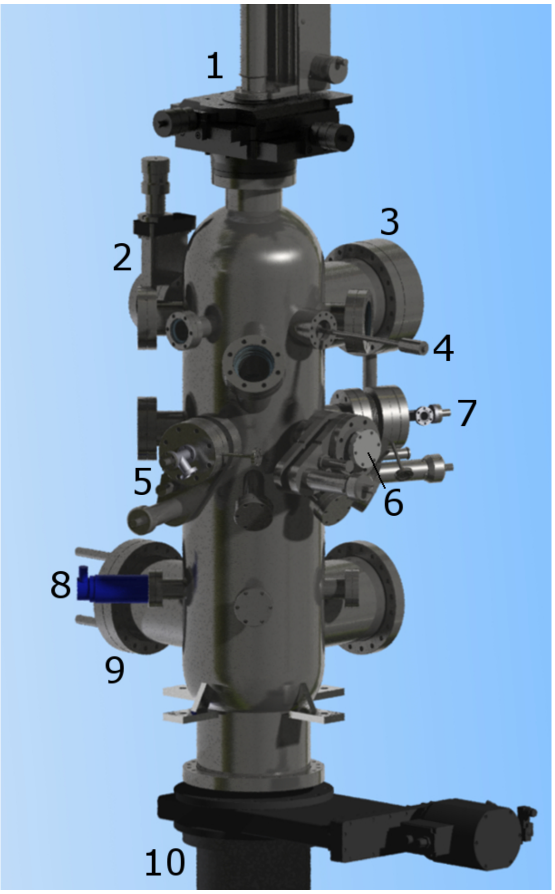

Figure 3.12: The IPES experimentation chamber showing the manipulator (1), LEED (3), in-vacuum screwdriver (4), GM photodetectors (5 and 7), electron gun (6), ion gauge (8), TSP (9), cryopump (10), and port leading to the preparation chamber (2). A detailed schematic can be found in Appendix I.

---

[1] Gauge reading on a SRS Stabil-Ion 370121 UHV ion gauge.

Using the transfer arm in the preparation chamber, samples can be moved to the IPES chamber and inserted into the receptacle shown in Figure 3.13. The tapered edges on the sample holder mate with guiding plates and ensure that the holder ends up centered in its slot. This in turn lines up a tapped hole in the holder (Figure 3.3) with a 4-40 screw in the receptacle that can be turned with an in-vacuum screwdriver. The screw guarantees that the holder cannot accidentally come loose and fall into the chamber, as well as creates a solid electrical connection. The receptacle is outfitted with two slots for sample holders so that a second, gold-covered holder can be used for determining Fermi levels and contact potential (Appendix D). It also features a Faraday cup for directly measuring the electron beam. The receptacle can be moved by a four-stage manipulator[1] that provides motion along x, y, z, and θ. To make these motions more convenient for the user, the assembly's center of rotation passes just above the surface of the azimuthal sample holder so that the electron beam should stay fixed at the approximately same sample position while θ is being adjusted.

3.5.1 LEED

The top of the IPES chamber is dedicated to performing low-energy electron diffraction (LEED) [36]. This is a well-established surface science technique, and we purchased our apparatus commercially.[2] It operates by firing a beam of low-energy electrons ($\sim 10 - 100$ eV) onto a sample surface, whereby some of the electrons back-scatter onto a phosphor screen. Due to their de Broglie wavelength, the electrons interfere and cause some regions of the screen to light-up while leaving others dark. If the sample's surface is well-ordered on the atomic scale, then the pattern will be sharp and predictable [37]. However, if the surface is amorphous, polycrystalline, or covered in adsorbed gasses, then the pattern will be distorted to some degree. Therefore, LEED is an effective probe of surface quality and can be used to directly determine if a sample has been sufficiently prepared for IPES. In addition, it can be used to verify whether a sample has been contaminated during the course of a measurement. We intend to use our LEED apparatus on a primarily qualitative basis when inspecting samples, determining if they are ordered enough for measurement or else require additional cleaning.

---

[1] VG Scienta Transax Translator

[2] LK Technologies, RVL2000/8/R

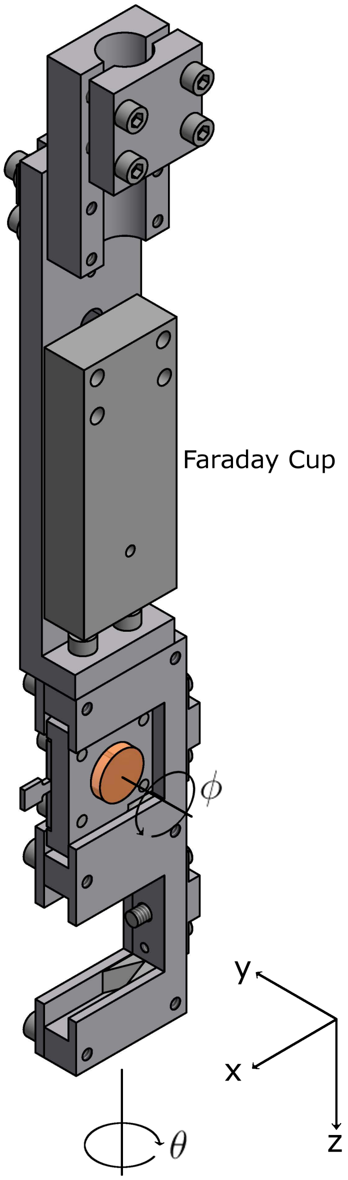

Figure 3.13: Sample holder receptacle in the IPES chamber showing an azimuthal holder inserted in the upper slot. Notice the screw (visible in the lower slot) that is used to secure holders in place. The receptacle can translate in x, y, and z and be rotated around its axis by angle θ. Rotating the azimuthal plug changes angle ϕ.

3.5.2 IPES

The components for performing IPES are positioned lower in the chamber. The two ports for the GM tubes are positioned symmetrically about the port for the low-energy electron gun, with which they form a horizontal plane. All three of the ports are equipped with linear translators that allow the devices to be moved in close to the sample when measurements are being taken and then retracted when the receptacle is being positioned, which helps them avoid collisions. There are also three viewports that allow the user to see the sample from various vantage points, and three more ports that are reserved for future use.

Many other IPES research groups have constructed custom low-energy electron guns based on a design presented by Stoffel and Johnson in 1985 [38]. We instead elected to purchase our gun commercially[1] in the hopes of saving significant time and resources. Building a low-energy electron gun with sufficiently high current and energy resolution for IPES that still maintains a small spot size and low angular divergence is a nontrivial exercise. When Stoffel and Johnson built their gun, there were no commercial options available. However, surface science technologies have greatly developed over the past three decades, and we believe our gun can perform comparably to theirs. For energies below 10 eV, both guns report currents on the order of 5 μA, spot sizes of about 1 mm^2, and an angular spread around 5° [39]. In addition, our gun produces an energy resolution comparable to those reported by other groups [8].

In order to improve the performance characteristics of the electron gun, our chamber was constructed from μ-metal, an alloy of nickel and iron. This material is engineered to posses an exceptionally high magnetic permeability and thus provides shielding from static magnetic fields. It is commonly used around low-energy electron guns [36] to avoid deflection from small fields such as the Earth's. Using μ-metal is an inexpensive and effective means of protecting an electron beam, and we have specifically noticed that our chamber reduces the intensity of Earth's field by at least an order of magnitude. (For more, see Appendix E.)

The lower end of the chamber is also equipped with a residual gas analyzer[2] (RGA) that is used for leak detection and to characterize the vacuum environment. Understanding the composition of the residual gas species in the vacuum can be important for performing IPES on reactive samples. Although it is installed on the IPES chamber, it can be used effectively to monitor the preparation chamber and load-lock, as well.

---

[1] Staib Instruments, Inc., NEK 150-1

[2] Stanford Research Systems, RGA 100

3.5.3 Pumping System

The IPES chamber is outfitted with a closed-loop helium cryopump[1] and a TSP.[2] Using Equations (3.1) and (3.2), the cryopump is expected to achieve pumping speeds of approximately 2200 L/s for H_2, and its base pressure is limited only by the outgassing rates of the chamber [40]. In practice, the chamber can readily achieve operating pressures below 10^{-10} Torr, which is comparable to what is found in the preparation chamber and compatible with the results of Section 2.4. If lower pressures were required for a reactive sample, this could be achieved with aggressive pumping using the TSP and thorough baking of the chamber.

3.6 Control Software

When performing an angle-resolved IPES experiment, many spectra are taken as a function of the energy of the electron gun and the sample's orientation in order to map-out as much of the Brillouin zone as possible. An enormous amount of time can be saved if these spectra can be generated through automated scans. Furthermore, the IPES spectrometer is comprised of a myriad of individual apparatus, many of which have multiple parameters that must each be carefully set for an experiment to execute properly. Keeping track of all of these settings can be an overwhelming task, particularly for inexperienced users. Therefore, we interfaced the spectrometer's most important components into a single LabVIEW[3] program that can be used to control, monitor, and scan over a multitude of the most commonly adjusted parameters. The program serves to highlight critical values that novice users may overlook, and it allows for more precise and intelligent control compared to a manual interface. Arguably its most powerful feature is its ability to perform multidimensional scans that would otherwise take users hours to setup and perform.

The program consists of a master process that manages and permits communication between several subroutines. Each subroutine controls the interface for one component on the spectrometer (for example, the electron gun) or runs a specific user task (for example, generating a scanning algorithm). Example screen shots illustrating the user-interface are shown in Figure 3.14, and a detailed description of the program's layout can be found on the group's wiki (Appendix H).

---

[1] CTI-Cryogenics Cryo-Torr 8F Cryopump, 8200 Compressor

[2] Gamma Vacuum

[3] National Instruments, LabVIEW 2010

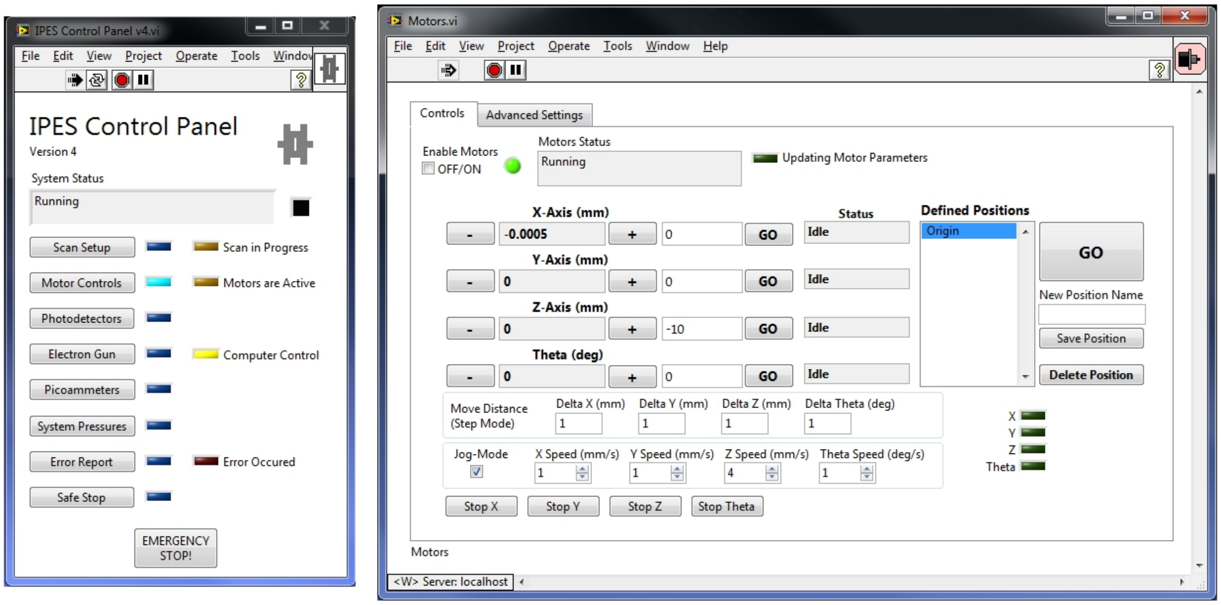

System Status: Running

Enable Motors ☐ OFF/ON

Motors Status: Running

				Status
X-Axis (mm)	-0.0005	0	GO	Idle
Y-Axis (mm)	0	0	GO	Idle
Z-Axis (mm)	0	-10	GO	Idle
Theta (deg)	0	0	GO	Idle

Defined Positions: Origin

New Position Name:

	Delta X (mm)	Delta Y (mm)	Delta Z (mm)	Delta Theta (deg)
Move Distance (Step Mode)	1	1	1	1

	X Speed (mm/s)	Y Speed (mm/s)	Z Speed (mm/s)	Theta Speed (deg/s)
Jog-Mode ☑	1	1	4	1

Figure 3.14: Example screen shots of the IPES control software showing the master process (left) and the subroutine that controls the manipulator (right).

Chapter 4

Photodetectors

As described in Chapter 2, angle-resolved inverse photoemission is performed in the vacuum ultra-violet (VUV) region where the intensity of the emitted photons is relatively weak. Therefore, our spectrometer requires the use of a photodetector with a high quantum efficiency and a wide collection angle to maximize count rates and minimize dwell times. No such device can be purchased commercially, and so a custom-design detector was constructed. Most practitioners of IPES today use detectors based around Geiger-Müller (GM) counting tubes, and we decided to follow their example. In particular, we based our design on that put forth by Stiepel et al. [8], which to our knowledge achieves the best energy resolution of any VUV GM photodetector.

Geiger-Müller tubes are utilized in a wide range of applications involving the detection of radiation. The Geiger counter for example, which employs a GM tube as its sensor, was developed by Geiger and Müller in 1928 [41] and is now commonly used for detecting nuclear radioactivity. For a more detailed look at GM tube operation, as well as radiation detection in general, Knoll's textbook [42] is a thorough and widely cited reference.

4.1 Basic Principles

The basic design of a GM tube is shown in Figure 4.1. The device is composed of a cylindrical conductor filled with a so-called "detection" gas and a conductive wire that runs along the central axis. When photons enter the tube, they are absorbed by gas molecules to produce ion pairs. Due to a high voltage setup between the cylinder and the wire, the negative ion in each pair is accelerated toward the wire (anode) and the positive ion accelerates toward the inner walls of the tube (cathode). When the ions reach their respective electrode, they deposit their change and become neutral. This charge is measured by external electronics that can then elucidate characteristics of the incident radiation.

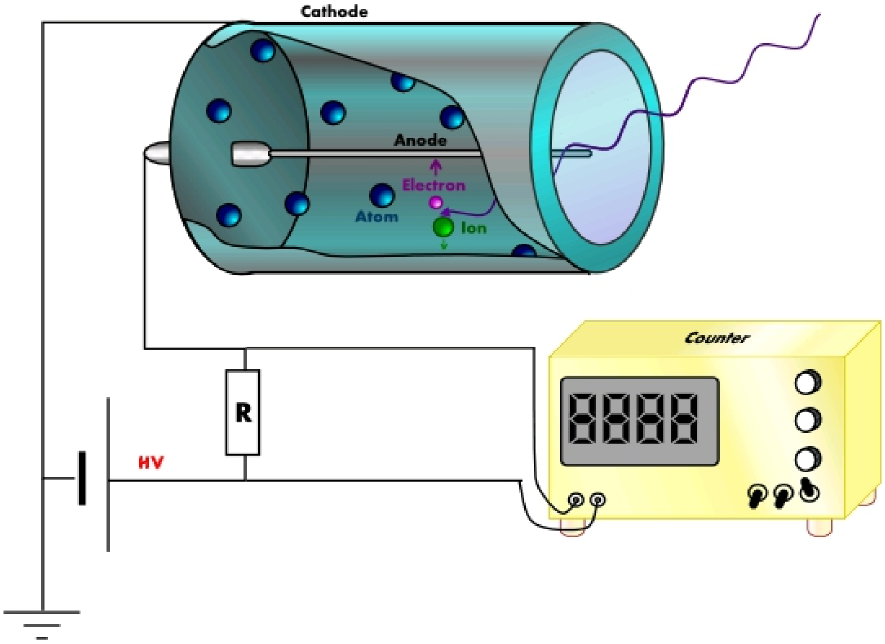

Figure 4.1: Basic design of a Geiger-Müller photodetector. Graphics adapted from Ref. [43].

For an IPES experiment, a GM photodetector must only measure a single photon frequency. This ability is naturally engineered into the GM tube by two means. First, the ionization energy of the detection gas ensures that photons below some threshold frequency cannot produce ion pairs. Therefore, every GM tube inherently acts as a high-pass filter sensitive only to energies above some cutoff. Second, photons in the range of interest to IPES cannot penetrate the metallic cathode and must be let into the tube through a window. It is easiest to install this window at the end of the tube, as in Figure 4.1, but it can be positioned anywhere. By selecting an appropriate material that is transparent to VUV photons but absorbing at higher energies, the window can behave as a low-pass filter. In combination, the window and detection gas thus make-up a band-pass filter, where the width of the pass-band is determined by the difference between the gas's ionization energy and the window's transmission cutoff. Many different materials have been employed for IPES including I_2 [4], CS_2 [44], ethanol [45], n-propanol [45], dimethyl-ether [12], and acetone [46] for detection gasses and CaF_2 [3], SrF_2 [47], and MgF_2 [48] for windows, all of which achieve a FWHM between about 400 and 100 meV.

4.1.1 Gas Multiplication

While the ions in the tube are drifting toward the anode and cathode, they undergo collisions with molecules in the gas along the way. Since the detection gas is stationary, its molecules will have zero velocity on average going into such collisions, and therefore the ion will tend to donate some of its kinetic energy to the molecule and slow down. In this way, the ion moves in a kind of stop-and-go pattern: accelerating due to the electric field, stopping after running into a molecule, then accelerating again. For a constant electric field and density of the detection gas, the ion will achieve some average maximum velocity between collisions and donate some average amount of energy per collision to the gas. However, since the electric field in the tube varies with a $1/r$ profile, the acceleration that the ion experiences depends on its location, and so too must its maximum velocity between collisions. If the ion is negative, it will encounter an increasingly stronger electric field as it drifts toward the central anode and therefore experience increasingly more energetic collisions. If the field becomes sufficiently strong, then it is possible that the ion will donate so much energy during a collision that the gas molecule will also become ionized. There will then be two negative ions that continue to drift toward the anode. During their next collisions, which can only be stronger due to the increasing electric field, they may each ionize yet another gas molecule, resulting in four ions drifting toward the anode. The number of negative ions will then start to grow like this in an exponential manner until they all reach the anode and neutralize.

The process just described is known as a Townsend avalanche [49,50], and it is the driving mechanism behind a phenomenon known as gas multiplication. Clearly, the avalanche results in more charge reaching the anode than what would have occurred if only the original ion had arrived. However, it is also important to note that the amount of extra charge will be the same no matter where in the tube the original ion begins its journey. This arises from the fact that, for a given mass of the ion and density of the detector gas, there is a threshold value of the electric field beyond which the avalanche will begin. Since the tube has cylindrical symmetry, this threshold corresponds to a critical radius, r', that defines the outer limit of the avalanche region surrounding the anode. Any ion that drifts into this region will immediately trigger an avalanche that, because it has the same distance to develop before reaching the anode, will always produce the same number of ions. The total amount of charge that reaches the anode will thus be the amount of charge on the original ion, multiplied by the number of ions created by the avalanche. Since the avalanche is due to collisions with the detection gas, the process is aptly named gas multiplication.

The size of a Townsend avalanche depends on the distance of the critical radius, r', from the anode, which in turn depends on the voltage difference between the anode and cathode.[1] For high voltages, the electric field in the tube is very strong, r' sits a long way out from the anode, and the degree of gas multiplication will be large. For low voltages, on the other hand, r' and the gas multiplication will be small. If the voltage is very low, then it is possible for r' to actually be less than the radius of the anode, which means no where in the tube will electrons be accelerated to high enough velocities to initialize an avalanche, and there will be no gas multiplication. The user can therefore choose the extent of gas multiplication simply by setting the voltage to the appropriate value.

In practice, the magnitude of gas multiplication can vary between detection events for various reasons. Many of these are related to microscopic fluctuations such as in the density of the detection gas and the electric field strength due to the presence of the ions. A detailed description of these effects are beyond the scope of this thesis, but a statistical analysis that accounts for their influence on a detector's output can be found in Ref. [42]. One important reason for variance that should be noted, however, is the possibility for the original ion pair to be created within the avalanche region between r' and the anode. In this case, the negative ion will immediately trigger an avalanche, but since there is less distance for it to grow before it reaches the anode, less charge will be generated. In fact, since the avalanche develops exponentially, the amount of charge will generally be much less and perhaps not be counted by the detector's electronics. This issue is minimized by engineering the detector to have a very narrow avalanche region tightly surrounding the anode wire so that statistically, the vast majority of ion pairs originate outside of the avalanche region.

When a photon is absorbed by a molecule in a gas, it ejects an electron into the surrounding environment. For many gasses, that electron will quickly be absorbed by a nearby neutral molecule so that the result of the photon was to create a positive and negative ion pair. However, in other gasses, neutral molecules have a very low electronic affinity, and the electron will remain free indefinitely. Due to their completely-filled outer shells, the noble gasses are good examples of species that support positive ion/free electron pairs after photoionization [26]. Free electrons have much higher mobility than negative ions, so they can achieve higher velocities and undergo more violent collisions under the influence of an electric field. This implies that their use in a GM photodetector requires

---

[1] The size of a Townsend avalanche also depends on geometrical factors and properties of the detection gas. See Equation (4.6).

less voltage to generate the same gas multiplication, and thus detection gasses with very low electronic affinities are often preferred. Argon, for example, is a common detection gas in many radiation sensors [42].

4.1.2 Modes of Operation

The goal of a GM photodetector is to measure the photon flux entering the tube. If the flux is low, then gas multiplication, as described in the previous section, will be required to increase the amount of charge reaching the anode and enable the external electronics to take an accurate measurement. For high flux, however, the charge initially generated by the photons is sufficiently large that it can be detected without any multiplication. Thus, the user will often adjust the degree of multiplication to suit the application by changing the voltage applied between the anode and cathode. Although the absolute size of the multiplication depends on many factors, the behaviour of the tube as a function of voltage will always show the same qualitative features. As shown in Figure 4.2, this behaviour adheres to several regions, or modes, that each demonstrate important properties of GM tube operation and are appropriate for use in different applications.

Recombination

Immediately following a photoionization event in the detection gas, the free electron and positive ion that were just created will be in close proximity to one another. If there is no externally applied electric field, then electrostatic attraction will draw them together, whereby they will neutralize through recombination. In Figure 4.2, this corresponds to the curve vanishing for zero applied voltage. If a very low voltage is applied, then a small force will attempt to pull the electron and ion apart. The electron may make it to the anode, but recombination is overwhelmingly likely. As the applied voltage is increased, the force separating the particles grows, recombination becomes less and less likely, and the height of the curve increases.

Saturation

As the applied voltage continues to increase, eventually the force separating the electron and ion will be so strong that recombination becomes negligible,[1] and the curve in Figure 4.2 levels off. Now all of the free electrons created through photoionization will make

---

[1] It should be noted that, although initial recombination is eliminated, there is still the possibility that ions from separate photoabsorption events can encounter one another as they drift through the gas and

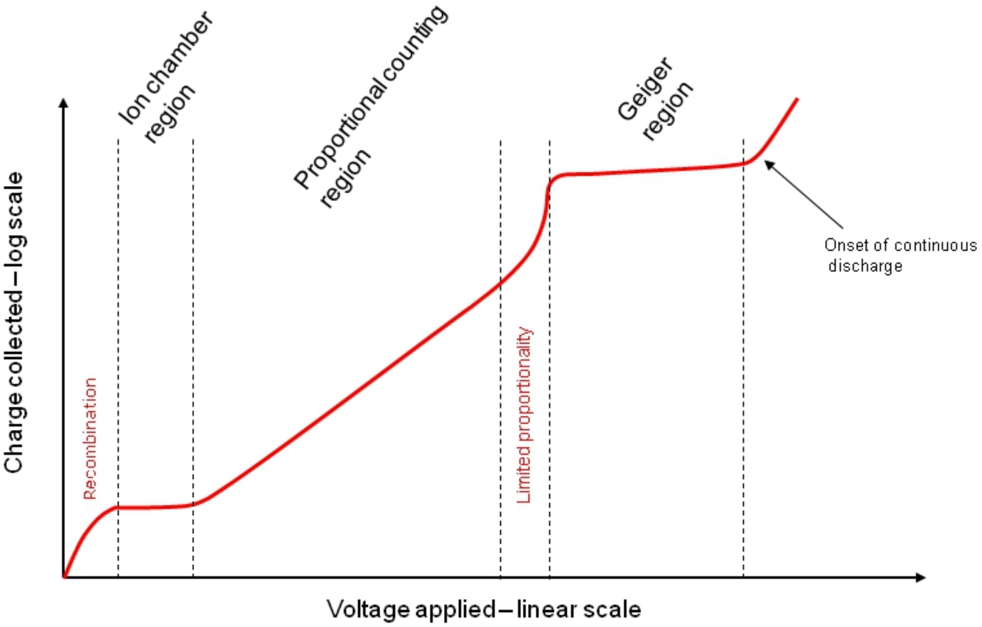

Figure 4.2: Charge collected by the anode as a function of anode voltage (cathode grounded) for constant incident flux. The region where recombination is non-negligible is generally avoided. Limited proportionality can be used for IPES, but is avoided for many applications. No detection is possible beyond the onset of continuous discharge. Graphics adapted from Ref. [51].

it to the anode for detection. However, the voltage is too low for gas multiplication to occur, and only incident radiation with a high flux can be detected. GM tubes operating in this mode find a wide range of application in so-called ionization chambers [52], though they rarely utilize cylindrical geometry. The flux in a typical IPES experiment is to low to exploit saturation mode.

Proportional Mode

If the voltage is increased further, Townsend avalanches will start triggering and gas multiplication will occur. Operating under these conditions is known as being in proportional mode since gas multiplication ensures that the amount of charge reaching the anode will be proportional to the amount of charge created by the photoionization event. If a GM tube is engineered properly so that the gas multiplication is sufficiently strong to make

---

recombine. For the low flux encountered in IPES, this is negligible, but it needs to be taken into account when operating an ion chamber.

individual events detectable, then an IPES experiment can be run in proportional mode. Note that a GM photodetector running in proportional mode is sometimes referred to as a proportional counter [53].

Limited Proportionality

Up to this point, the dynamics of the electrons and ions moving through the detection gas have been mostly overlooked. How they diffuse through the tube, as well as the time it takes for them to travel to the cathode and anode, are nontrivial subjects that are beyond the scope of this thesis. For additional details, particularly regarding how they relate to the detector's output pulse shape, we direct the reader to Ref. [42]. One aspect that we will discuss, however, is the discrepancy between the speed at which free electrons and ions move through the tube. Due to their smaller mass and collision cross section, electrons might move 1000 times faster or more through the tube than the positive ions they leave behind. Therefore, to a good approximation, electrons complete their journey to the anode, including the Townsend avalanche, before the positive ions have really moved at all. For low incident flux and small avalanches, this is of little consequence, and the ions slowly drift toward the cathode independent of the electrons whizzing through the tube. But if many ionization events occur over a short time, such as in many large avalanches, then the positive ions can significantly alter the electric field in the tube. In particular, they tend to form a cloud of positive charge around the anode, where most ionization events occur, that disrupts the $1/r$ nature of the electric field and effects subsequent avalanches.

When the applied voltage is increased beyond the proportional mode, avalanches become very large, and the effects of the positive ion cloud become significant. Gas multiplication no longer ensures proportionality between the number of original ions and the charge that reaches the anode. Therefore, the GM tube is said to operate in limited proportionality mode. For an IPES experiment, limited proportionality is of no concern, and the only important difference between this mode and proportional mode is the size of the avalanches. However, for GM tubes used to detect other kinds of radiation, such as alpha particles or gamma rays, this becomes more important. A photon in the VUV range will produce one ion pair when it is absorbed, and thus the number of incident photons equals the number of avalanche pulses that reach the anode, regardless of their magnitude. Other particles, however, may produce many ion pairs, and thus both the number of avalanche pulses and their heights are required to determine the number of incident particles [42].

Geiger-Müller Mode

For voltages higher than those encountered in limited proportionality mode, electrons will encounter exceedingly high field values before they reach the anode. Townsend avalanches can thus become so energetic that they will start to emit photons with sufficiently high energy to be detected in the tube. In other words, an avalanche can emit a photon that will be absorbed in a different region of the tube and create another ion pair. The electron from that pair will then drift toward the anode and spark a second avalanche. The second avalanche will then emit another photon, and the cycle continues. Due to the same effects that are important in limited proportionality mode, a large cloud of positive charge will start to surround the anode and alter the local electric field, with the net effect being to reduce the magnitude of the field. Eventually, the field will be reduced to such an extent that avalanches will no longer trigger, and the production of photons will cease. The cycle is therefore self-limiting, but it will cause the entire avalanche region to discharge after encountering a single free electron.

The size of the avalanche pulse when running in Geiger-Müller mode will be far larger than in any other mode. This is advantageous in many applications, including IPES, that detect low-energy particles with low flux. However, as described earlier, it takes a considerable amount of time for the positive ions to drift away from the anode before another avalanche can occur. During this time, the detector is blind to incident photons, and so dead time procedures may need to be executed [54].

Continuous Discharge

If the applied voltage is increased too far, the GM tube will begin to continuously discharge. In other words, a constant stream of electrons will flow into the anode, regardless of whether any photons are entering the tube. There are multiple mechanisms that can cause this behaviour [54]. For example, the anode wire will never be perfectly smooth, and microscopic features such as sharp peaks can generate exceptionally high values of the local electric field. This in turn can ionize the surrounding gas through a process known as a corona discharge, which will trigger an avalanche.

Another possible culprit is electrons liberated from the cathode walls. When a positive ion is neutralized through the absorption of an electron, it will release energy of the amount

$$E_{\text{out}} = E_{\text{bind}} - E_{\phi}, \tag{4.1}$$

where E_{bind} is the binding energy of the state in the ion being filled and E_{ϕ} is the work

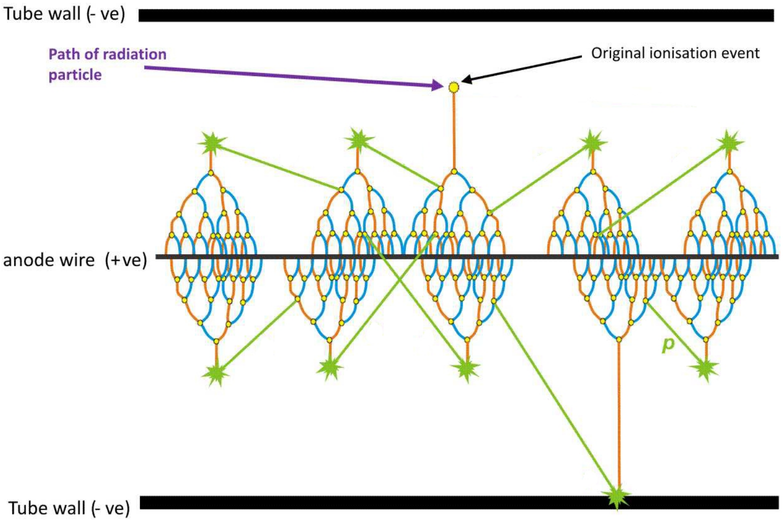

Figure 4.3: The mechanism underlying a Geiger-Müller discharge. The free electron created by the incident photon triggers a Townsend avalanche. The avalanche produces a VUV photon, which gets absorbed elsewhere in the tube and creates a second free electron. The second electron creates a second avalanche, and the cycle continues until the entire tube has discharged. Graphics adapted from Ref. [55].

function of the cathode walls. If

$$E_{\text{out}} \geq E_{\phi}, \tag{4.2}$$

then it is possible that a second electron will be ejected from the cathode and drift toward the anode to cause another avalanche. This process is problematic when operating in any mode, but the small probability of its occurrence usually makes its effects negligible. At worst, it causes the occasional erroneous avalanche immediately following a true detection event, which can be identified and corrected in the final data. However, so many positive ions are generated during a Geiger-Müller discharge that it can become overwhelmingly likely that at least one extra electron will always be liberated from the cathode walls. This electron will then trigger another Geigher-Müller discharge, which will liberate another electron, and the cycle continues perpetually.

Whatever the cause, continuous discharge will always occur in any GM tube if the voltage is ramped high enough. The massive number of electrons produced with every Geiger-Müller discharge completely washes out any information about actual detection events, and so no detector can be used in this mode. In fact, it is possible to damage a detector if operated in this mode for too long by overloading the electronics, the presence of arcing inside the tube, or denaturing of the detection gas from frequent, violent collisions (if it is a complex compound like a hydrocarbon).

4.1.3 Signal Processing

When a GM tube is operated in proportional, limited proportionality, or Geiger-Müller mode, as is the case for IPES, each detection event creates a pulse of charge on the anode created by the Townsend avalanche. This pulse is short-lived and has an intensity on the order of pA or less, and so it is very difficult to detect directly. It must therefore first pass through a series of signal conditioning electronics, the particular sequence of which is well established for IPES [11].

The anode is connected to a preamplifier,[1] or preamp, which greatly amplifies the signal and turns the charge pulse into a voltage pulse. In other words, the amplitude of the pulse exiting the preamp is proportional to the amount of charge it receives. It collects the charge using an RC circuit, and therefore the pulse shape is a sharp rise followed by an exponentially decaying tail. This pulse then passes into an amplifier[2] which filters some of the noise and linearly amplifies the signal according to user-based settings. The amplifier also reshapes the pulse into a narrow peak with a time constant on the order of μs. The pulse is then sent through a single channel analyzer[3] (SCA) which acts as a discriminator and analogue-to-digital converter. Again according to user settings, the SCA will detect pulses within a certain height interval and, for each one, output a digital pulse. The digital pulse is then fed into a computer counter card[4] which can be integrated into various software to determine the count rate measured by the detector.

4.2 Design

Geiger-Müller photodetectors found in recent experiments [8–11, 13], like the example shown in Figure 4.4, are all based on the original design constructed by Denninger, Dose, and Scheidt in 1979 [4]. The device consisted of a stainless steel tube of approximately 1” inner diameter capped on one end by a CaF_2 window 2 mm thick. The anode consisted of a stainless steel wire 1.5 mm in diameter, and the tube was filled with a mixture of I_2

---

[1] Ortec 142PC

[2] Canberra 2012

[3] Canberra 2031

[4] National Instruments, PCI-6221

and He gas.[1] It obtained a band-pass of about 560 meV FWHM centered upon 9.6 eV in the VUV range. Subsequent designs by other groups included different anode metals, different methods for attaching the window, and different gas/window material combinations, but remained essentially the same in terms of concept and geometry. Dose, Fauster, and Schneider attempted the first significant change in 1986 by heating their SrF_2 window to lower the cutoff energy and reduce the width of the transmission window to 172 meV FWHM [47]. This methodology has recently been repeated by Budke and coworkers, but the difficulty to implement such a design has hindered its widespread adoption. The most recent change was demonstrated by Stiepel, Ostendorf, Benesch, and Zacharias in 2005 when they added a gas absorption chamber in front of their CaF_2 window [8]. The chamber can be filled with krypton gas, which has an absorption peak corresponding to the high-energy end of their pass-band. By adjusting the pressure of the krypton, they can decrease the width of their transmission window, to an extent limited only by the maximum differential pressure that their windows can withstand. They achieved a resolution of 115 meV FWHM, but this could in theory be greatly improved. They were also able to achieve more precise control over their resolution with less effort than is required when changing the temperature of windows, and therefore we elected to base our GM photodetectors on a similar design.

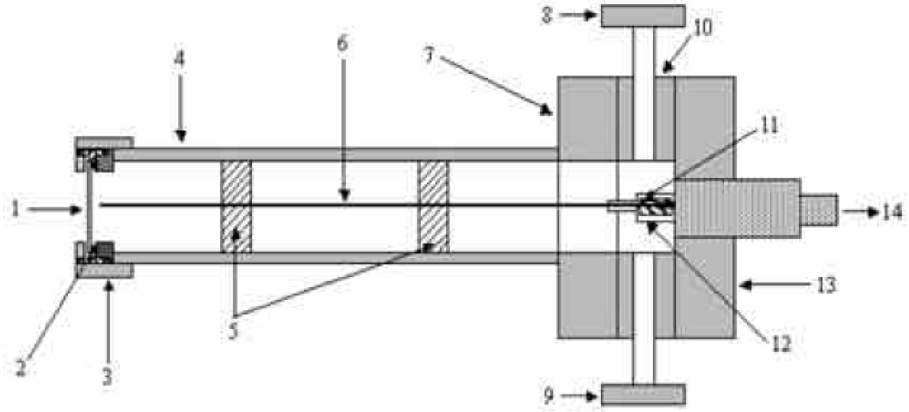

Figure 4.4: The GM tube used by Shukla, Banik, and Barman [11], typical of most GM tubes used for IPES, showing the window (1), O-ring seal (2), cathode (4), Teflon spacers (5), anode (6), CF flanges (7, 10, 13), detection gas inlets (8, 9), connector (11), Teflon insulator (12), and SHV feedthrough (14).

---

[1] The I_2 served as the detection gas. The He was present to increase the pressure and supply extra electrons during the Townsend avalanche. The He is known as a multiplication gas, and its use is common practice in many GM tubes.

4.2.1 Geometry

An important step in our design process was to determine what diameter of tube we should use. Clearly, a wider diameter would potentially be able to capture a wider collection angle,[1] but it could also limit how close the detector can get to the sample due to space restrictions. In particular, enough room had to be left to allow the electron gun to approach the sample. Therefore, to determine the optimal diameter, some numerical calculations were performed that computed the solid angle collected for a variety of geometries.

The geometric framework used in our calculations is depicted in Figure 4.5. For simplicity, we assumed the GM tube must point directly at the sample. In other words, a line that bisects and is normal to the window must pass through the center of the sample (the origin in the figure). In addition, the detector is assumed to be brought as close to the sample as possible without colliding with the electron gun, which means it becomes closest for $\beta \to 90°$. However, as the angle is increased, the bottom edge of the detector eventually drops below the sample plane and, since VUV photons cannot penetrate the solid sample, will be in the sample's shadow and not collect any photons. Any part of the detector below the plane must thus be disregarded from the solid angle calculation. The total solid angle collected by a detector is therefore given by

$$\Omega = 2\pi(1 - \cos\chi) - \iint_S \sin\theta' d\theta' d\phi', \tag{4.3}$$

where S is the surface of the detector's window below the sample plane and χ is the half angle of the cone that is formed by the window and the sample's center.

Figure 4.6 shows the results of the calculations for several tube diameters that correspond to the maximum that will fit inside standard a standard 2.75”, 4.5”, and 6” flange. It also shows how the results change when the sample plane is tilted, which is important since we intend to rotate the sample for angle-resolved IPES. Clearly, the solid angle over which photons can be collected increases for increasing tube diameter, as expected. However, the observed pattern of the optimum angles for the GM tubes relative the electron gun was not so obvious. For the 2.75” flange, the GM tube captures the most solid angle around 75°. But for 4.5” and 6”, it increases to 83° and 86°, respectively.

We ultimately elected to use a 4.5” flange for our GM tube. This was partly due to the fact that installing a 2 mm-thick window made of a brittle fluoride crystal onto a GM tube so large as to fit in a 6” flange would likely be very costly and technologically

---

[1] Recall that IPES suffers from relatively low photon flux and long dwell times. Having a wide collection angle captures more photons and achieves a higher signal to noise ratio in less time.

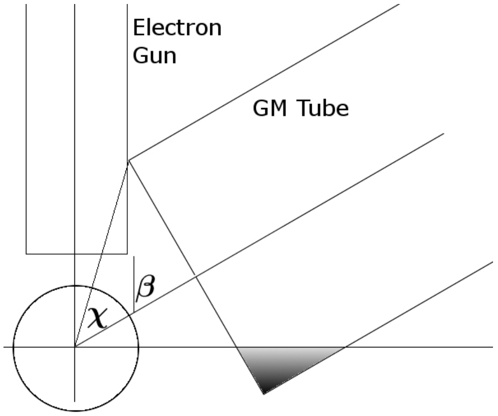

Figure 4.5: Geometry used to optimize the position of the GM tube as a function of β. The shaded region will not see any photons and must be subtracted from the solid angle calculation.

challenging. However, it was also because no GM tube intended for use on a VUV IPES spectrometer to our knowledge has ever been constructed with a diameter much larger than 1". The GM tube on the 4.5" flange would increase this by about 90%, and although there is no indication in the literature that 1" is chosen for any reason besides practical convenience and tradition, we decided it would be best not to stray too far into uncharted territory. We also elected to position the GM tubes at 70° from the sample plane. This was a compromise with practical restrictions on the positioning of the flanges, but it still achieves a collection angle close to nominal. In fact, the algorithm that generated the data in Figure 4.6 underestimated the size of the absorption chamber that was ultimately installed onto the end of the tube, and thus the 4.5" curves likely appear more similar to those for the 2.75" flange, which are approximately maximized at 70°.

4.2.2 The GM Tube

Following in the footsteps of Stiepel and coworkers, we decided to engineer our pass-band using acetone as the detection gas and CaF_2 as the entrance window. This achieves a mean detection energy of 9.84 eV with an inherent resolution of 320 meV FWHM [8]. To further improve the resolution, we added an absorption chamber in front of the windows that can be filled with krypton gas to a pressure that we can precisely control. The absorption chamber is separated from vacuum by a second, identical CaF_2 window with an inter-window spacing of 7.6 mm. A fine copper mesh with 88.6% optical transmission[1] protects the outer window

---

[1] Precision Eforming, MC-49

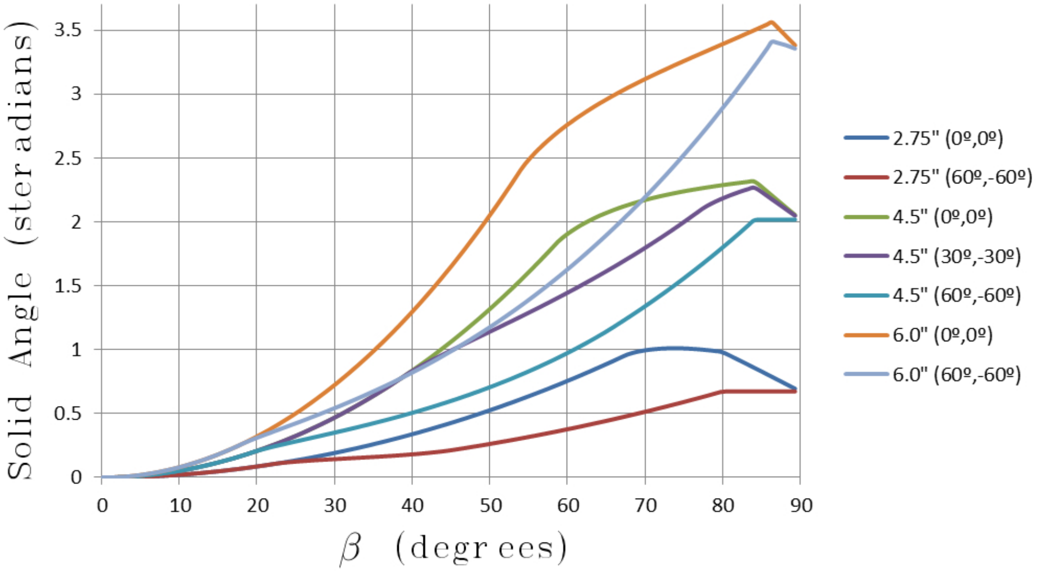

Figure 4.6: Solid angle collected versus viewing angle β. Two GM tubes are assumed, placed symmetrically about the electron gun. Data presented for tubes mounted on 2.75", 4.5", and 6" flanges. Angles in brackets indicate sample tilt, θ, where $\theta = 0$ implies normal incidence.

from the electron beam that can otherwise cause charging. The windows can withstand a pressure differential of up to 1.5 atm, and thus we can fill our absorption chamber with approximately twice as much krypton (by mass) than previously demonstrated. Our tube should therefore be capable of achieving at least the same resolution of 115 meV, if not significantly better.

Our final design for the GM photodetector is shown in Figure 4.7. All metallic components are made from austenitic stainless steel to be chemically inert and non-magnetic, the latter being an important property due to the close proximity of the electron gun. The cathode tube, absorption chamber, and widows were constructed as a single piece, which we had manufactured by MPF Products, Inc. Therefore, many of the small details, such as the radii of the windows and the spacing between them, were dictated by the company's engineering capabilities, but the finished product closely resembles the design we originally proposed. Many other groups (for example Ref [12]), have installed their own optics using UHV epoxy, but we opted to employ the expertise of a third party to ensure a clean and reliable solution, which MPF delivered.

The tube is mounted on a double-sided 4.5" CF flange that can be installed onto the

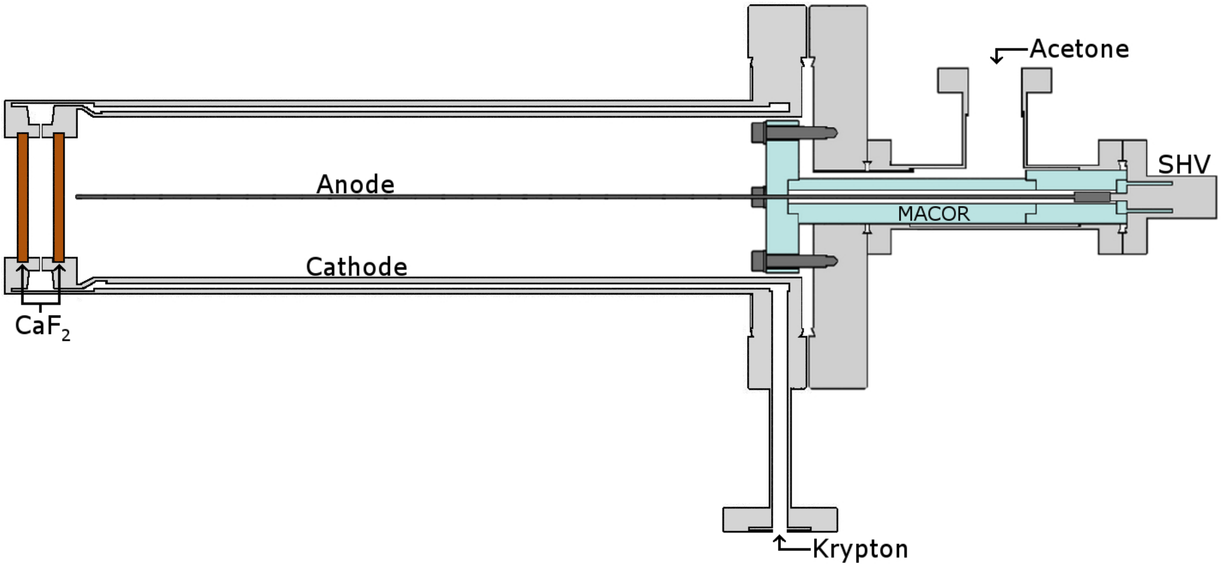

Figure 4.7: Our GM photodetector design, to scale.

chamber with the anode assembly, mounted on a 4.5" to 1.33" (mini) zero-length reducer,[1] installed right behind. The anode wire is mechanically fixed to a mini safe high voltage (SHV) feedthrough[2] that is separated from the reducer by a mini tee,[3] the side port of which is used to fill and evacuate acetone. The wire is electrically isolated from the grounded tee with a sheath of ceramic MACOR to avoid issues that may arise from the higher electric field in this region (brought about by the smaller diameter tube). Photons absorbed in the tee will experience more gas multiplication and disrupt the measured pulse-height distribution. Furthermore, this region is more likely to undergo Geiger-Müller or continuous discharges at high voltages, potentially making the tube less stable. The MACOR is held in place by four 6-32 PEEK screws assembled with aluminum lock washers to maintain tension while the components change size during a bake.

The cathode has an inner diameter of about 48 mm, and the wire, made of stainless steel which we mechanically polished,[4] has a diameter of 1 mm. The windows are each 3 mm-thick and have a viewable diameter of about 35.5 mm. The detection chamber sits back from the front of the detector by 1.7 cm, and the detector has an outer diameter of about 57.4 mm (±0.2 mm or so due to a perimeter weld). Taking all of this into ac-

---

[1] MDC 150006

[2] Accu-Glass SHV5-GS-133

[3] MDC 404000

[4] Using sand papers down to 1 μm grit size.

count, the two GM tubes installed at 70° from the electron gun collect a total solid angle of approximately 0.86 steradians, or 14% of a hemisphere, when the sample is normal to the electron beam. (For the details of how we came to this value, see Appendix F. Note that the effect of the copper mesh has been neglected.)

4.3 First Results

Recent articles about VUV IPES (for example, see Ref. [10]) suggest that using acetone in a GM detector solves many of the performance issues experienced by earlier tubes that used other gasses (see Ref. [14, section 4.6]). The procedure for constructing and operating the essential components of an IPES spectrometer is now well-established, and having closely followed this procedure, we were hopeful that we would get our GM photodetectors up and running with minimal hassle. However, we have encountered considerable difficulty, and at the time of writing, our GM tubes are still not fully operational.

During the first tests of the tubes, we aimed the electron gun at a polycrystalline aluminum sample holder in the hopes of producing VUV photons to initially verify that the tubes are at least capable of detecting something. To our surprise, the tubes did not report any counts regardless of the beam's energy. Having no way to rule out the possibility that this was due to a lack of any photons being produced, we then installed an old ion gauge filament directly in the line-of-sight of the tubes. By passing sufficient current through the filament, it glows white hot and thus guarantees that there is at least some flux of VUV photons entering the tubes. However, still no counts were detected.

Upon closer inspection, it was discovered that the tubes do actually output pulses, but they are usually hidden below the noise level. Also, many of these pulses are erroneously produced and can show up even when no photons enter the GM tube. (Example pulses and a demonstration of how it can be lost in the noise is shown in Figure 4.8.) However, by increasing the SCA cutoff pulse height until most of the noise is excluded, the count rate substantially increases when the filament is activated, thus indicating that some of the pulses are caused by true detection events. For example, the count rate was once recorded to rise from 0.14 Hz to 0.83 Hz, an increase by a factor of almost 6. It should also be noted that this increase is reproducible for a variety of anode voltages and detection gas pressures, and that no other noise-induced increase has ever produced such a dramatic result. Therefore, we have concluded with confidence that the GM tubes are actually operating, but poorly.

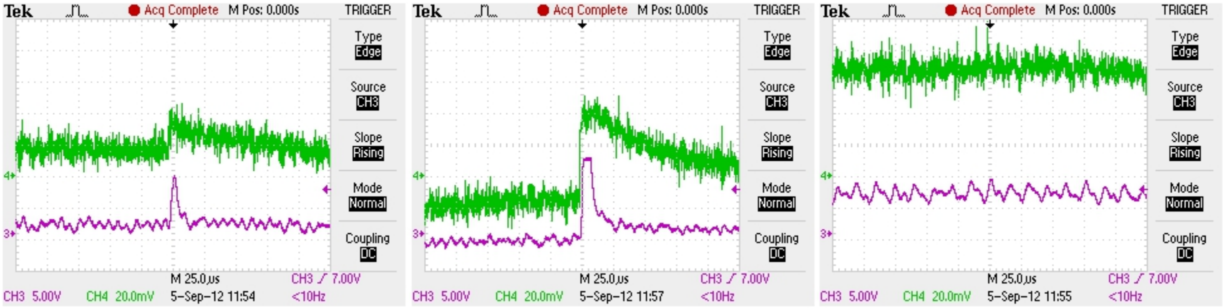

Figure 4.8: Example output from the GM photodetectors after passing through the preamp (green) and amplifier (purple). Left: A pulse showing the expected shape from each device. Center: A pulse of exceptionally high amplitude, likely from a GM discharge. Right: Example low-frequency, high-amplitude noise oscillation that demonstrates how the SCA is incapable of separating signal from noise.

4.4 Potential Problems

After verifying that all of the other components, including the electron gun and signal processing electronics, are operating properly, we concluded that our troubles must originate from one of two sources. First, our GM tubes seem to experience an abnormally high level of noise, which could be drowning out all but the largest pulses. Certainly, our spectrometer possesses an array of complicated apparatus that are potential sources of electrical and vibrational interference, and it is possible that smaller spectrometers in the literature may be less noisy. The second potential problem could arise from the only appreciable difference between our GM tube and those in the literature: the inner radius of our cathode is nearly double the usual size. When the original design was first reported [4], the authors did not make it clear that the dimensions of their tube were optimal. To our knowledge, we are the first experimenters of VUV IPES to make significant geometric alterations to this design, and thus we cannot rule out the possibility that increasing the cathode's radius does not detrimentally alter the tube's operation without first performing our own analysis.

4.4.1 Noise

The reports in the literature rarely provide sufficient details about their electronics for us to deduce the pulse heights experienced by other groups, but Banik and coworkers estimate that approximately 10 000 electrons reach their anode after an average detection event [10]. This would imply a pulse height coming out of our preamp, which reports a gain of 4 V/pC, of approximately 6.4 mV. However, typical noise at that stage has an amplitude of $\sim$ 20 mV or worse, making the detection of such small pulses very difficult.

It is likely that the majority of our noise is originating on the anode wire where it begins at reasonably low levels, but after passing through the preamp and amplifier, grows to intolerable amplitudes. This is supported by the results in Figure 4.9, which depict the reduction in noise after the SHV cable between the anode and the preamp was replaced by a zero-length adapter. Noise of all frequencies was dampened by approximately half. Thus, we believe the best course of action going forward is to improve the noise characteristics of the anode assembly.

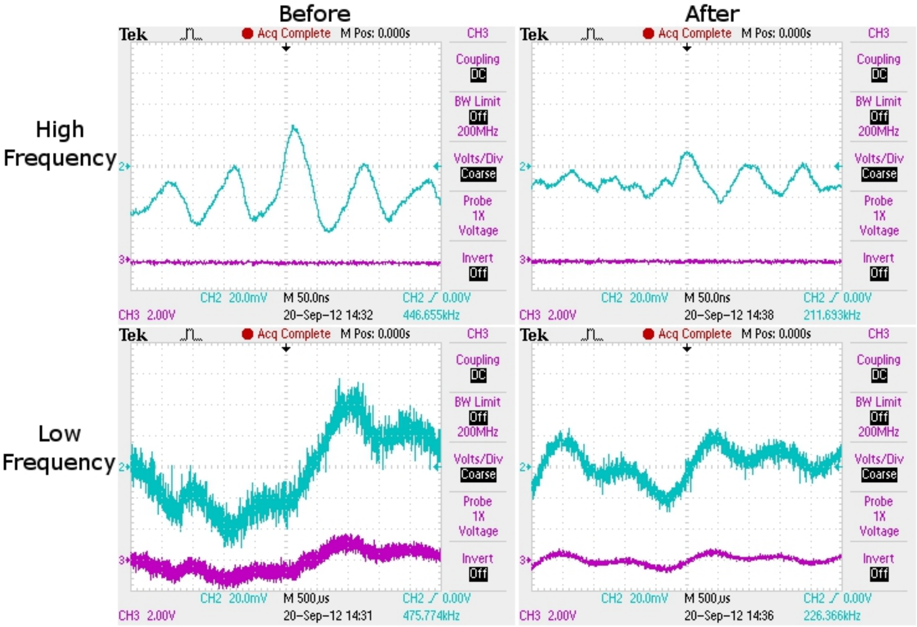

Figure 4.9: Noise coming out of the preamp (blue) and amplifier (purple). The amplitude of both high frequencies (top row) and low (bottom row) reduce to approximately half of their original value (left column) after the SHV cable between the preamp and anode is replaced by a zero-length adapter (right column).

There are two sources that dominate the noise in the anode assembly. The first is mechanical. Since the wire is more than 21 cm long and only 1 mm thick, it is not surprising that it might vibrate due to nearby pumps and other moving parts on the vacuum system. The precise effects of an oscillating wire on the detector's output are not immediately obvious, however we have witnessed that they can be potentially significant. Simply hitting the side of the chamber with one's hand causes a short-lived, high-amplitude spike in the noise, which implies low-amplitude, prolonged oscillations from vibrating pumps could certainly account for at least part of our background noise. Furthermore, testing the tube after physically isolating it from the spectrometer has demonstrated a dramatic reduction in noise consistent with the associated reduction in vibration.

The second noise source comes from the ground loop that our design inherently facilitates. Since the SHV feedthrough is electrically connected to the grounded chamber, a loop exists from earth ground, to the electronics, to the preamp, to the SHV connector, to the GM tube, to the chamber, and back to earth ground. The physics of how ground loops can affect the noise of low-amplitude signals is nontrivial, but in general their effect is to worsen the signal quality [56]. Again testing the tube after isolating it from the system, we have validated this trend and seen that breaking the ground loop significantly improves the detector's output signal.

4.4.2 In-Depth Analysis of GM Tube Operation

To understand the effects of our cathode's unusually large radius, we must determine what pulse heights we expect the tube to output. The following analysis is derived from the work of Knoll in Ref. [53].

Theoretical Pulse-Height

Assuming we are in proportional mode so that space charge effects are negligible (Section 4.1.2), then the total charge that reaches the anode after a photoionization event is given by

$$Q = n_0 e M, \tag{4.4}$$

where n_0 is the number of electrons initially created in the detection event ($n_0 = 1$ for VUV photons) and e is the elementary electric charge. The gas multiplication M is determined from the general relation

$$\ln M = \int \alpha(r) dr, \tag{4.5}$$

where the integral is over the avalanche region. The function $\alpha(r)$ is known as the first Townsend coefficient and is unique to every gas and the geometry of the detector. Evaluating this integral is nontrivial, but a commonly used solution for cylindrical geometry was presented by Diethorn [57]:

$$\ln M = \frac{\mathbb{V}}{\ln b/a} \frac{\ln 2}{\Delta \mathbb{V}} \left(\ln \frac{\mathbb{V}}{Pa \ln b/a} - \ln K \right). \tag{4.6}$$

This equation takes geometry into account through a and b, the radii of the anode and cathode, respectively. The tunable parameters are the voltage on the anode, $\mathbb{V}$, (cathode is grounded) and the pressure of the detection gas, P. In addition, M depends on two constants of the gas: $\Delta\mathbb{V}$, the voltage through which a free electron moves between ionization events, and

$$K = \frac{\mathscr{E}}{P}, \tag{4.7}$$

the threshold ratio of the electric field, $\mathscr{E}$, and gas pressure above which multiplication is possible. Since our preamp has a gain of 4 V/pC, then the pulse height we should expect, in mV, is

$$\begin{aligned} W &= 4 \times 10^{15} Q & (4.8)\\ &= 4 \times 10^{15} e \times \exp\left[\frac{\mathbb{V}}{\ln b/a}\frac{\ln 2}{\Delta\mathbb{V}}\left(\ln\frac{\mathbb{V}}{Pa\ln b/a} - \ln K\right)\right]. & (4.9)\end{aligned}$$

Comparison with the Literature

To proceed, we require precise values of K and $\Delta\mathbb{V}$ for acetone, which are unfortunately hard to find in the literature. Furthermore, we should justify the intervals of a, b, $\mathbb{V}$, and P over which the Diethorn solution is accurate for an acetone-filled tube. This is a nontrivial exercise beyond the scope of this thesis, and the results are likely to only be approximate anyway. It might therefore seem like we are forced to abandon our goals, but we can still arrive at a reasonable, order-of-magnitude estimate for the pulse height by using approximate values of the constants and trusting that the Diethorn solution is at least somewhat accurate for most of the values of interest. More importantly, we can still make a direct and accurate comparison between the performance of our tube and those found in the literature. We can then determine if we should expect comparable pulse heights, and consequently if our current design is limited by noise or geometry.

Banik, Shukla, and Barman have examined the operating characteristics of their acetone/CaF_2 photodetector as a function of anode voltage and gas pressure [10]. They found optimal operating conditions of 745 V and 4 mbar ($\simeq$ 3 Torr), which due to the similarity between tubes in the literature, we can assume is at least close to optimal for most detectors. Using values of $\Delta\mathbb{V} = 30$ V and $K = 13.3$ V/mm·Torr[1] [53], we would expect a typical tube with a 1”-diameter cathode and 1 mm-diameter anode to output

---

[1] These values are actually for propane, but its similarities to acetone, both chemical and physical, imply they should be valid, at least to a modest approximation. In fact, many volatile hydrocarbons have values of the same order of magnitude as those used here.

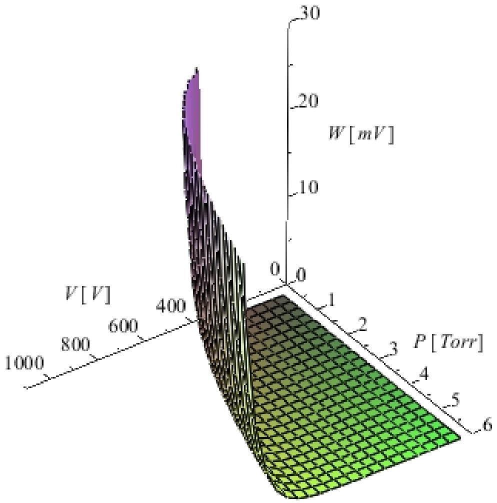

Figure 4.10: Expected output pulse height as a function of anode voltage and gas pressure using our detector's geometry.

pulses from our preamp with a height of roughly 285 mV. Using our geometry, we expect the pulse heights to only be 15 mV. The latter height corresponds well to the pulses we have observed (Figure 4.8). However, it is more important to consider the qualitative result of this comparison, namely that our tube should output pulses far smaller than those of other groups.

Figure 4.11 shows how W depends on the radius of the anode for multiple cathode radii. Invariably, as the cathode radius decreases, the pulse height increases. This is not surprising since a smaller distance between the anode and cathode implies a stronger voltage gradient (i.e. electric field), which generates a larger avalanche. However, the results are more complicated as the anode radius is varied while the cathode radius is fixed. For very small anode radii, the pulse height approaches infinity, which corresponds to the case of a very thin wire and thus very high electric field values in its immediate vicinity. This is the limit in which GM tubes are theoretically intended to operate, where the $1/r$ dependence of the electric field generates large but uniform gas multiplication. Pulse height also increases, though, as the anode radius is increased, albeit more slowly. Again, this occurs since the separation between the anode and cathode is disappearing, but the pulses in this regime now resemble those of a parallel plate avalanche counter [53]. The electric field approaches a constant value and the avalanche region becomes very large. It will thus become far more likely for ionization events to occur within the avalanche region, resulting in a wide distribution of pulse heights and a less stable detector.

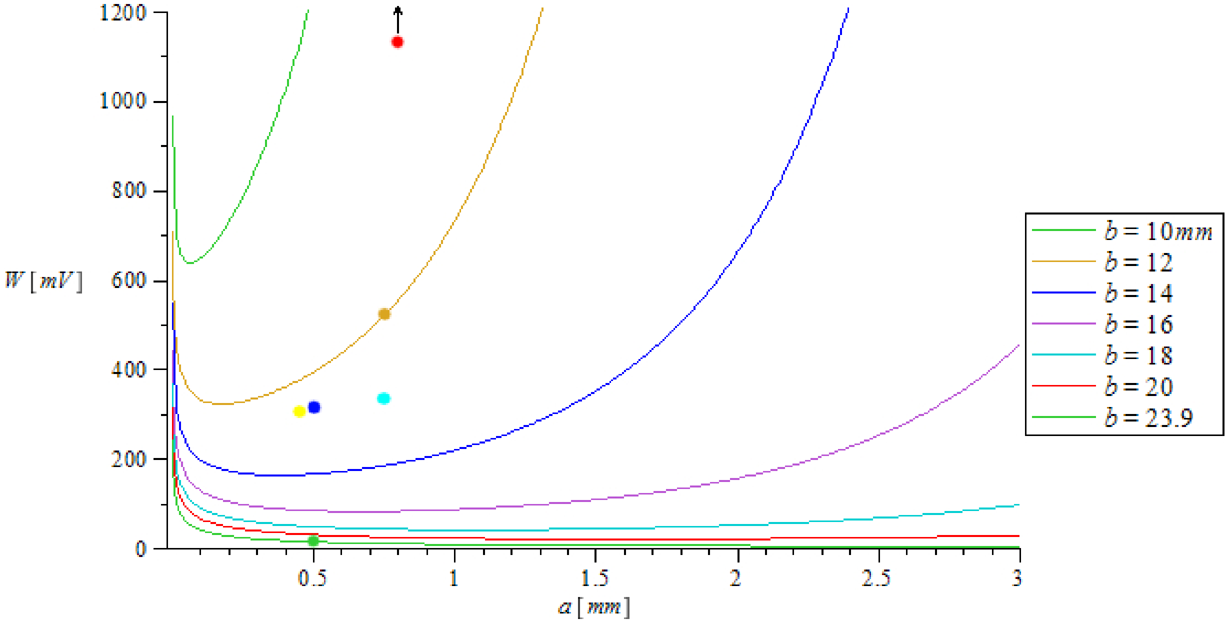

Figure 4.11: Pulse height as a function of anode and cathode radii. Large values on the left of the curves' minima correspond to "classic" GM behaviour, whereas large values on the right are approaching parallel plate avalanches. Dots correspond to the geometry of tubes in the literature (a, b): yellow (0.45, 12.5) [46]; blue (0.5, 12.5) [8]; cyan (0.75, 12.7) [12]; gold (0.75, 12) [4]; red (0.8, 8.9) [11]; green (0.5, 23.9) [our design].

The results of Figure 4.11 display a disturbing trend in the GM tubes designed for IPES. First of all, the majority of designs reside in the low-amplitude well in the center of the graph. In particular, our own design sits very close to the minimum value of the $b = 23.9$ mm curve. In essence, we accidentally optimized the geometry of our tube to have the lowest possible pulse height, and the tubes of many other groups are not far off. Decreasing our cathode's radius and/or changing our anode's radius in either direction would undoubtedly improve our tube's performance. Furthermore, it is also troubling that those tubes in the literature that are significantly far from the well, such as in Ref. [11] (red dot in the figure), are on the side approaching parallel plates. This could be the reason why some tubes exhibit such large pulse height distributions [10], but more work must be done to know for sure.

4.5 Proposed Modifications

Going forward, we plan to implement some design changes that should improve the performance of our GM tubes. As shown in Figure 4.12, the new tube will be different in three important respects. First, structural supports will be inserted between the cathode and anode to significantly reduce vibrations and, as a consequence, noise. The supports must be rigid and electrically insulating, and their cross sectional area (not shown in the figure) must be small so that they block as few photons as possible from passing deeper into the tube (Appendix G). Thus, we intend to use MACOR ceramic machined into a shape similar to the spokes of a wheel. Second, the ground of the SHV feedthrough will be electrically isolated from the CF flange, and therefore also from the vacuum chamber. A new cathode with a smaller radius will then have to be inserted inside the old one and connected to the ground on the SHV, and it too must be isolated from the vacuum chamber (see the figure). With this configuration, the ground loop described in Section 4.4.1 will thus be broken, and the noise should be reduced substantially further. Finally, the reduction of the cathode's radius will also have an effect on the height of the output pulses. As described in Section 4.4.2, reducing the cathode's radius causes pulse heights to increase, which makes the effects of noise less significant. However, we will have to be careful to avoid the parallel plate regime, possibly by reducing the anode's radius if necessary.

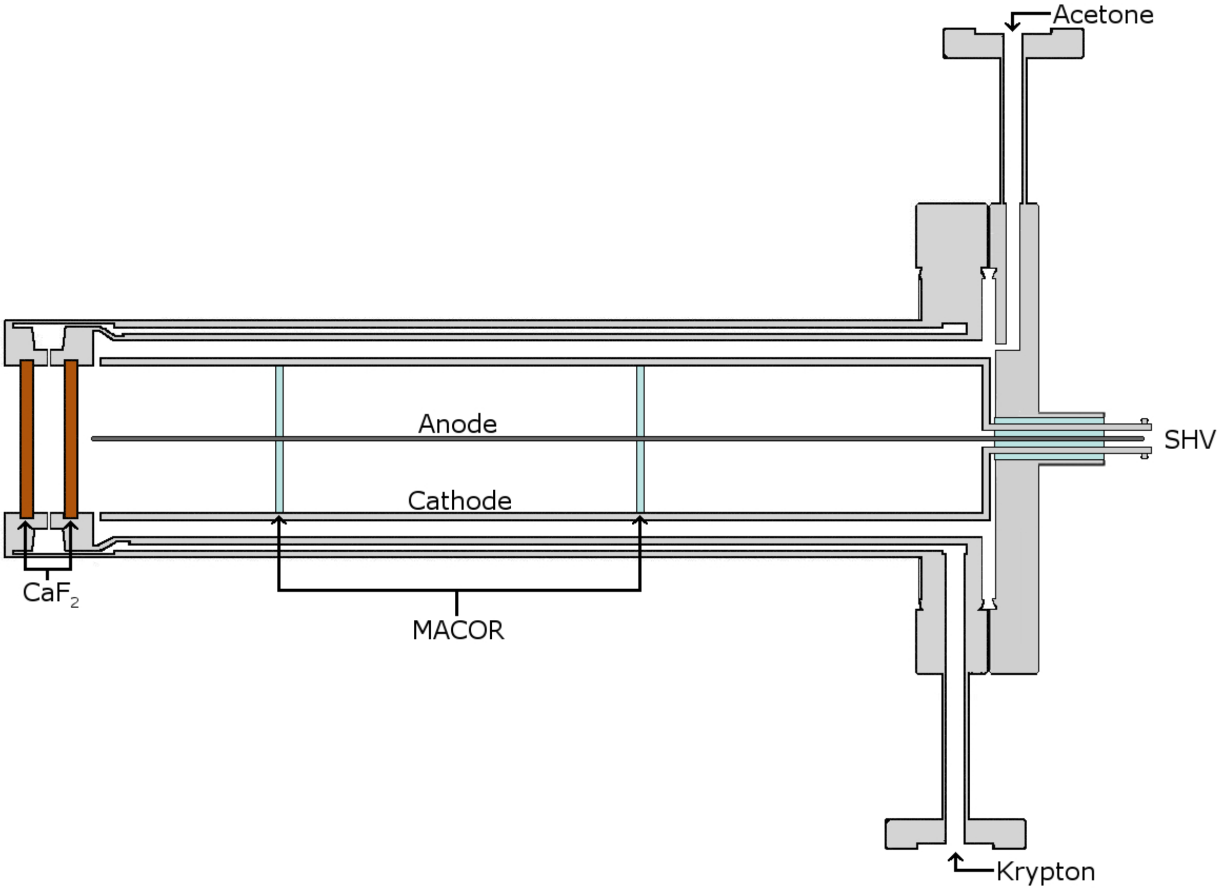

Figure 4.12: Schematic of the proposed modifications to the GM tube that eliminate the inherent ground loop, mechanically stabilize the anode, and should therefore result in a higher signal-to-noise ratio.

Chapter 5

Conclusions

With the construction of the IPES spectrometer recently completed, the vast majority of its components are now operating at a level that meets or exceeds our expectations. The various sample preparation apparatus have been tested and have proven that they will be capable of producing well-ordered surfaces with very little contamination from adsorbed particles. In addition, our custom-designed sample holders and sample transportation and storage systems have demonstrated their effectiveness and their potential to save the experimenter valuable time by reducing the frequency with which samples need to be moved into and out of vacuum. Both the preparation and IPES vacuum chambers can achieve pressures deep in the ultra-high vacuum region, a capability that is necessary to maintain clean sample surfaces and to facilitate long intervals of uninterrupted measurements, and the system's most important and commonly used user-adjustable parameters have been centralized into a single piece of control software that, among many other functions, can generate complicated, multi-dimensional scans intended to make the collection of lengthy series of IPES measurements more efficient.

The Geiger-Müller photodetectors are the last major components on the system that have yet to be commissioned. However, after a few geometrical modifications that we intend to implement in the near future that should increase the signal-to-noise ratio of their output, we expect them to operate with an energy resolution and collection efficiency that rivals or surpasses other leading detectors in the field. Following this, all that remains is to characterize the resolution of the detectors, electron gun, and the spectrometer as a whole, which we plan to perform using several well-studied surfaces of copper single crystals, before moving on to examine the cuprate superconductors. We are confident that our spectrometer will ultimately become a state-of-the-art system for performing ARIPES, and that with it, our group will be in a position to make significant progress in the field of strongly correlated materials.

References

[1] J. B. Pendry, “Theory of inverse photoemission,” *Journal of Physics. C, Solid State Physics*, vol. 14, pp. 1381–1391, March 1981.

[2] N. V. Smith, “Inverse photoemission,” *Reports on Progress in Physics*, vol. 51, pp. 1227–1294, 1988.

[3] V. Dose, “VUV isochromat spectroscopy,” *Applied Physics*, vol. 14, pp. 117–118, September 1977.

[4] G. Denninger, V. Dose, and H. Sheidt, “A VUV isochromat spectrometer for surface analysis,” *Applied Physics*, vol. 18, no. 4, pp. 375–380, 1979.

[5] S. Hüfner, *Photoelectron Spectroscopy: Principles and Applications*, ch. 9. Berlin: Springer-Verlag, 3rd ed., 2003.

[6] D. P. Woodruff, N. V. Smith, P. D. Johnson, and W. A. Royer, “k-resolved inverse photoelectron spectroscopy and its application to Cu(001), Ni(001), and Ni(110),” *Physical Review. B, Condensed Matter*, vol. 26, pp. 2943–2955, September 1982.

[7] P. D. Johnson and S. L. Hulbert, “Inverse photoemission,” *Review of Scientific Instruments*, vol. 61, pp. 2277–2288, September 1990.

[8] R. Stiepel, R. Ostendorf, C. Benesch, and H. Zacharias, “Vacuum ultraviolet photon detector with improved resolution for inverse photoemission spectroscopy,” *Review of Scientific Instruments*, vol. 76, May 2005.

[9] M. Budke, V. R. adn H. Liebl, G. Rangelov, and M. Donath, “Inverse photoemission with energy resolution better than 200 meV,” *Review of Scientific Instruments*, vol. 78, August 2007.

[10] S. Banik, A. K. Shukla, and S. R. Barman, "Optimal operating conditions and characteristics of acetone/CaF_2 detector for inverse photoemission spectroscopy," *Review of Scientific Instruments*, vol. 76, May 2005.

[11] A. K. Shukla, S. Banik, and S. R. Barman, "Fabrication of an inverse photoemission spectrometer to study unoccupied electronic states," *Current Science*, vol. 90, February 2006.

[12] I. G. Hill and A. B. McLean, "A comparison of two high performance inverse photoemission bandpass detectors," *Review of Scientific Instruments*, vol. 69, January 1998.

[13] M. Budke, T. Allmers, M. Donath, and G. Rangelov, "Combined experimental setup for spin- and angle-resolved direct and inverse photoemission," *Review of Scientific Instruments*, vol. 78, November 2007.

[14] A. G. Mark, "Kripes studies of metal and semiconductor surfaces," Master's thesis, Queen's University, Kingston, Canada, April 2004.

[15] M. Nakatake, Y. Okamura, S. Akiyama, H. Namatame, and M. Taniguchi, "High-resolution photon detection system for inverse-photoemission spectroscopy," *Journal of Electron Spectroscopy and Related Phenomena*, vol. 88-91, pp. 1027–1030, March 1998.

[16] N. W. Ashcroft and N. D. Mermin, *Solid State Physics*, ch. 18, p. 360. Brooks/Cole, Cengage Learning, 1976.

[17] S. Hüfner, *Photoelectron Spectroscopy: Principles and Applications*, p. 45. Berlin: Springer-Verlag, 3rd ed., 2003.

[18] I. G. Hill, *Design of An Inverse Photoemission Spectrometer For Studies of Quantum Wires.* PhD thesis, Queen's University, Kingston, Canada, September 1997.

[19] J. Lipton-Duffin, "First results from a third generation kripes system," Master's thesis, Queen's University, Kingston, Canada, September 2001.

[20] S. Hüfner, *Photoelectron Spectroscopy: Principles and Applications.* Berlin: Springer-Verlag, 3rd ed., 2003.

[21] P. D. Johnson and J. W. Davenport, "Calculated inverse photoemission cross sections from adsorbed molecules," *Physical Review. B, Condensed Matter*, vol. 31, pp. 7521–7525, June 1985.

[22] J. J. Sakurai and J. Napolitano, *Modern Quantum Mechanics*, ch. 7, pp. 472–483. San Francisco: Addison-Wesley, 2nd ed., 2011.

[23] J. J. Sakurai and J. Napolitano, *Modern Quantum Mechanics*, ch. 5, pp. 355–365. San Francisco: Addison-Wesley, 2nd ed., 2011.

[24] J. M. Lafferty, *Foundations of Vacuum Science and Technology*, ch. 1, p. 19. New York: John Wiley & Sons, Inc, 1998.

[25] G. Anger, A. Winkler, and K. D. Rendulic, "Adsorption and desorption kinetics in the systems H_2/Cu(111), H_2/Cu(110) and H_2/Cu(100)," *Surface Science*, vol. 220, no. 1, pp. 1–17, 1989.

[26] W. M. Haynes, ed., *CRC Handbook of Chemistry and Physics*. Cleveland, Ohio: CRC Press, 93rd ed., 2013. Chemical Rubber Company.

[27] "Sample holder for RSXS endstation." `http://exshare.lightsource.ca/REIXS/Pages/SamplePrep.aspx`. Candian Light Source.

[28] A. Technologies, "High/ultra-high vacuum seminar," USA, September 2011.

[29] "RMDG40 PGRMS(OMH) dual shaft rotatable sample transporter." `http://www.ferrovac.ch/`, 2010. Ferrovac GmbH.

[30] LK Technologies, *LK Technologies NGI3000 Sputtering Gun Owner's Manual*, July 1996.

[31] R. G. Musket, W. McLean, C. A. Colmenares, D. M. Makowiecki, and W. J. Siekhaus, "Preparation of atomically clean surfaces of selected elements: A review," *Applications of Surface Science*, vol. 10, no. 2, pp. 143–207, 1982.

[32] "Miniature knudsen-cell (k-cell)." `http://tectra.de/k-cell.htm`, 2012. tectra GmbH.

[33] Inficon, *IC/5 Operting Manual.* ch. 2.

[34] J. M. Lafferty, ed., *Foundations of Vacuum Science and Technology*, ch. 2. New York: John Wiley & Sons, Inc, 1998.

[35] Agilent Technologies, *Turbo-V 750/850 TwisTorr*, September 2010.

[36] LK Technologies, *Reverse View 8" LEED Optics with Retraction Model RVL2000/8/R*, 2011.

[37] C. S. McKee, M. W. Roberts, and M. L. Williams, "Defect surface structures studied by leed," *Advances in Colloid and Interface Science*, vol. 8, pp. 29–87, 1977.

[38] N. G. Stoffel and P. D. Johnson, "A low-energy high-brightness electron gun for inverse photoemission," *Nuclear Instruments and Methods in Physics Research*, vol. 234, pp. 230–234, February 1985.

[39] Staib Instruments, *User's Manual Low Energy Electron Source NEK-150-1*, June 2009.

[40] Helix Technology Corporation, *Cryo-Torr Pump Installation, Operation, and Maintenance Instructions*, 2005.

[41] H. Geiger and W. Müller, "Elektronenzählrohr zur messung schwächster aktivitäten," *Die Naturwissenschaften*, vol. 16, no. 31, pp. 617–618, 1928.

[42] G. F. Knoll, *Radiation Detection and Measurement*. John Wiley & Sons, Inc., 4th ed., 2010.

[43] T. Knott. http://en.wikipedia.org/wiki/File:Geiger.png, 2005. Wikimedia Commons.

[44] P. M. G. Allen, P. J. Dobson, and R. G. Egdell, "Empty electronic states in the sodium tungsten bronzes: A study by inverse photoemission spectroscopy," *Solid State Communications*, vol. 55, pp. 701–704, August 1985.

[45] J. A. Lipton-Duffin, A. G. Mark, and A. B. McLean, "Photon detection with n-propanol and C_2H_6O isomers," *Review of Scitentific Instruments*, vol. 73, pp. 3149–3153, September 2002.

[46] D. Funnemann and H. Merz, "10 eV photon detector for inverse photoemission," *Journal of Physics. E, Scientific Instruments*, vol. 19, no. 7, pp. 554–557, 1986.

[47] V. Dose, T. Fauster, and R. Schneider, "Inproved resolution in VUV isocromat spectroscopy," *Applied Physics. A, Solids and Surfaces*, vol. 40, pp. 203–207, August 1986.

[48] K. C. Prince, "Improved inverse photoemission detector," *Review of Scientific Instruments*, vol. 59, pp. 741–742, May 1988.

[49] G. F. Knoll, *Radiation Detection and Measurement*, ch. 4. John Wiley & Sons, Inc., 4th ed., 2010.

[50] B. B. Rossi and H. H. Staub, *Ionization chambers and counters: experimental techniques*. New York: McGraw-Hill, 1949.

[51] D. Sim. `http://en.wikipedia.org/wiki/File:Detector_regions.gif`, 2012. Wikimedia Commons.

[52] G. F. Knoll, *Radiation Detection and Measurement*, ch. 5. John Wiley & Sons, Inc., 4th ed., 2010.

[53] G. F. Knoll, *Radiation Detection and Measurement*, ch. 6. John Wiley & Sons, Inc., 4th ed., 2010.

[54] G. F. Knoll, *Radiation Detection and Measurement*, ch. 7. John Wiley & Sons, Inc., 4th ed., 2010.

[55] D. Sim. `http://en.wikipedia.org/wiki/File:Spread_of_avalanches_in_G-M_tube.jpg`, 2012. Wikimedia Commons.

[56] *Low Level Measurements Handbook*, ch. 3. Keithley, 6th ed.

[57] W. Diethorn, "A methane proportional counter system for natural radiocarbon measurements," tech. rep., Carnegie Institute of Technology, Pittsburgh, March 1956. NYO-6628.

[58] J. M. Lafferty, ed., *Foundations of Vacuum Science and Technology*. New York: John Wiley & Sons, Inc, 1998.

[59] M. S. Kaminsky and J. M. Lafferty, eds., *Dictionary of Terms for Vacuum Science and Technology*. Woodbury, New York: AIP Press, 1980.

[60] J. M. Lafferty, ed., *Foundations of Vacuum Science and Technology*, p. 5. New York: John Wiley & Sons, Inc, 1998.

[61] D. V. Schroeder, *An Introduction to Thermal Physics*, p. 12. Addison Wesley Longman, 2000.

[62] E. H. Kennard, *Kinetic theory of Gases with an Introduction to Statistical Mechanics*, p. 110. New York: McGraw-Hill, 1938.

[63] A. Roth, *Vacuum Technology*, p. 45. Amsterdam: North Hollad Publications, 3rd ed., 1990.

[64] D. Da and X. Da, "Kinetic theory of gas molecules in an extrahigh vacuum," *Journal of Vacuum Science and Technology. A, Vacuum, Surfaces, and Films*, vol. 5, pp. 2484–2487, July 1987.

[65] J. M. Lafferty, ed., *Foundations of Vacuum Science and Technology*, section 3.3, pp. 159–170. New York: John Wiley & Sons, Inc, 1998.

[66] Cacycle. `http://en.wikipedia.org/wiki/File:Two_moving_spirals_scroll_pump.gif`, 2006. Wikimedia Commons.

[67] Agilent, "Agilent | TriScroll 600." `http://www.chem.agilent.com/en-US/products-services/Instruments-Systems/Vacuum-Technologies/Primary-Vacuum-Pumps/TriScroll-600/Pages/default.aspx`, November 2012.

[68] P. V. GmbH, "Turbopumps." `http://www.pfeiffer-vacuum.com/filepool/File/Literatur_Pdf/PT0191PEN-Turbopumps.pdf?referer=1649`, August 2012.

[69] J. M. Lafferty, ed., *Foundations of Vacuum Science and Technology*, p. 238. New York: John Wiley & Sons, Inc, 1998.

[70] J. M. Lafferty, ed., *Foundations of Vacuum Science and Technology*, section 4.6, pp. 238–247. New York: John Wiley & Sons, Inc, 1998.

[71] B. Automation, "CTI-Cryogenics." `http://buy.brooks.com/products/category17.html`, November 2012.

[72] J. M. Lafferty, ed., *Foundations of Vacuum Science and Technology*, ch. 5. New York: John Wiley & Sons, Inc, 1998.

[73] NOAA/NGDC and CIRES, "Main field total intenstiy (F)." `http://www.ngdc.noaa.gov/geomag/WMM/`, January 2010.

[74] M. Nobre, A. Fernandes, F. Ferreira da Silva, R. Antunes, D. Almeida, V. Kokhan, S. V. Hoffmann, N. J. Mason, S. Eden, and P. Limão-Vieira, "The VUV electronic spectroscopy of acetone studied by synchrotron radiation," *Physical Chemistry Chemical Physics*, vol. 10, no. 4, pp. 542–549, 2008.

APPENDICES

Appendix A

Vacuum

Inverse photoemission must be performed under the pristine conditions of ultra-high vacuum (UHV). The techniques and apparatus for producing UHV are well established, and many of the required components are now commercially available. However, vacuum science is an extensive field in its own right, and researchers who conduct experiments in UHV greatly benefit from a familiarity with its underlying physics. For our spectrometer, the requirement of UHV was often a dominating consideration in many of our designs. Since it constituted such a large portion of my education, and also because new student researchers in our laboratory will need to learn about UHV, I have included this appendix as a review of the basics of vacuum science. This information should be particularly helpful for Chapter 3, where designs of the various components in our spectrometer are described. For further reading, see Ref. [58].

A.1 Definitions and Conventions

A vacuum is defined as a region of space devoid of all matter. Producing a true vacuum in the laboratory for use in an experiment is virtually impossible, so researchers must instead rely on low-pressure environments that can closely approach the vacuum idealization. This is generally achieved by housing experimental apparatus in a well-sealed container that is then evacuated until its internal gas pressure is sufficiently low for the particular application. For sensitive experiments, the necessary pressure can be exceedingly low and requires a great deal of thought and effort to be achieved.

Range	Pressure	Particle Density*	Mean Free Path*
Atmospheric Pressure	760 Torr	2.4×10^{19} cm^{-3}	64 nm
Rough			
	10^{-3} Torr	$3.2{\times}10^{13}$ cm^{-3}	4.9 cm
High (HV)			
	10^{-9} Torr	$3.2{\times}10^{7}$ cm^{-3}	49 km
Ultra-High (UHV)			
	10^{-12} Torr	32 188 cm^{-3}	49 Mm
Extreme High (XHV)			
	0	0	∞

*300 K, pure N_2

Table A.1: The vacuum ranges. The various standards organizations have defined their own specific limits for each range that may not match those given here. However, the classification of a vacuum into a range is generally for qualitative description only, and these values should serve well as approximate guidelines.

A.1.1 Vacuum Ranges

For practical purposes, a vacuum is considered to be any environment with a gas pressure of less than 1 atmosphere. Different vacua can thus be distinguished by their different pressures, with lower pressure considered to be higher quality. The quality of a vacuum is also categorized into one of several ranges, listed in Table A.1. The choices for the specific values that divide the ranges arise from technological considerations [28, 58] In general, the set of equipment and sample-handling practices that is required to achieve a vacuum in each range is (for the most part) unique. This implies that there are also different costs associated with operating in each range, with the higher quality ranges usually being more expensive. For example, to improve the quality of a vacuum from 10^{-8} Torr in the high vacuum (HV) range to 10^{-10} Torr in the UHV range, new pump types and cleaner procedures will likely need to be employed, which may be expensive to implement. However, to go from 10^{-6} Torr to 10^{-8} Torr, both of which are in the HV range, smaller improvements will likely be required such as better seals or a pump upgrade.

Due to the differences in equipment and procedures, facilities are sometimes labelled with the vacuum range that they are equipped to reach. For example, a laboratory may be described as a “UHV lab” if it has the equipment and expertise required to produce and exploit UHV quality vacua for its experiments. This classification is used in part because many vacuum experiments are performed in just one of the ranges. For example, infrared spectroscopy is almost always performed in HV since in rough vacuum the pressures are intolerably high, and UHV will provide negligible benefit over HV that cannot justify the added costs. Thus, one would expect to find an infrared spectroscopy experiment in an "HV lab," but not in a "UHV lab."

Since it is increasingly challenging to achieve a higher quality vacuum, a new range has historically been "tacked on" to the low-pressure end of the spectrum following significant advancements in vacuum technology that made access to that pressure range widely available [59]. Currently, XHV defines the lowest pressure range since it is extremely difficult to achieve and only available in very specialized laboratories. However, if the technology to reach XHV ever goes into commercial production with reduced costs, then the lower limit of XHV will likely be redefined to some finite value, and a new range will be created for pressures lower than XHV.

A.1.2 Units

Vacuum science has a rich history that has resulted in the invention of a multitude of redundant units. The International Standards Organization recommends the Pascal (Pa), equivalent to N/m^2, for pressure measurement [60], but many other units are still in widespread use. In North America, the Torr is very common and is used primarily throughout this thesis. It is helpful to remember that [26]

$$1 \text{ atm } = 760 \text{ Torr } = 101\,325 \text{ Pa.} \tag{A.1}$$

Additional conversion information can be found in Appendix B.

A.2 The Behaviour of Low-Density Gasses

Gasses at and around atmospheric pressure are well described by classical fluid mechanics and usually behave more or less according to our intuition. At much lower pressures, however, the rarity of particle interactions can cause some behaviour that may be unexpected to the inexperienced user.

A.2.1 The Ideal Gas Law

Pressure is defined as the net force exerted onto a surface per unit area by the impinging particles of a gas. The pressure contributed by one particle having mass m and velocity component perpendicular to the surface, $v_{\perp,i}$, upon which it collides is thus

$$\varrho = 2mv_{\perp,i}, \tag{A.2}$$

where we have assumed an elastic collision. Since for constant temperature the gas does not undergo a net exchange of energy with the walls of its container, this is a valid assumption (at least on average). If η particles, each with mass m, strike the surface per unit time with velocity perpendicular to the surface $v_{\perp,i}$, then the resulting pressure will be given by

$$P_i = \sum \varrho = 2\eta m v_{\perp,i}. \tag{A.3}$$

Statistically, half of the particles in the gas will have $v_\perp$ directed toward the surface and half away. Therefore, the flux of particles incident upon the surface must be

$$\eta = \frac{n_i v_{\perp,i}}{2}, \tag{A.4}$$

where n_i is the number of particles per unit volume with perpendicular velocity $v_{\perp,i}$, and Equation (A.3) becomes

$$P_i = n_i m v_{\perp,i}^2. \tag{A.5}$$

The total pressure from all particles must therefore be

$$\begin{aligned} P &= \sum_i P_i \qquad &(A.6)\\ &= \sum_i n_i m v_{\perp,i}^2 \qquad &(A.7)\\ &= nm \sum_i \frac{n_i v_{\perp,i}^2}{n}. \qquad &(A.8) \end{aligned}$$

But this can be rewritten as

$$P = nm\overline{v_\perp^2}, \tag{A.9}$$

where n is the total particle density and the overbar represents the arithmetical mean.

By symmetry, the average of the square of a gas particle's velocity component in any particular direction must be the same as in all other directions. Therefore, we have

$$\overline{v_\perp^2} = \overline{v_x^2} = \overline{v_y^2} = \overline{v_z^2}, \tag{A.10}$$

and also

$$\begin{aligned}\overline{v^2} &= \overline{(v_x^2 + v_y^2 + v_z^2)} \qquad \text{(A.11)}\\ &= \overline{(3v_\perp^2)}\\ &= 3\overline{v_\perp^2}. \qquad \text{(A.12)}\end{aligned}$$

Upon substitution into Equation (A.9), this leads to

$$P = \frac{1}{3}nm\overline{v^2}. \tag{A.13}$$

From thermodynamics [61], we know that for a particle with 3 translational degrees of freedom,

$$\frac{1}{2}m\overline{v^2} = \frac{3}{2}kT. \tag{A.14}$$

Thus,

$$P = nkT. \tag{A.15}$$

The above relation is known as the ideal gas law. Assuming a constant density throughout the gas, this can be rewritten as

$$PV = NkT \tag{A.16}$$

where V is the total volume and N the total number of gas particles.

The above analysis implicitly assumes that the gas particles undergo interactions only in the classical sense. In other words, gas particles travel in straight lines at constant speed until they undergo simple, instantaneous, elastic collisions with either another gas particle or a surface of the container. Although in reality gas particles frequently experience interactions that are complicated in nature and extended in time [28], this condition is approximately satisfied when the gas is of a high temperature and low density. To great precision, room temperature air can be modelled by the ideal gas law, and it only becomes more applicable for vacua.

According to Equation (A.15), the density of a gas is linearly proportional to its pressure. Therefore, when a gas at atmospheric pressure is reduced to a high quality vacuum like UHV, the number of particles within it may be reduced by 11 orders of magnitude or more. To a very good approximation, no gas remains after such a reduction, and our assertion that UHV is an adequate substitute for an ideal vacuum is validated.

A.2.2 The Mean Free Path

Employing the hard sphere approximation, a collision occurs in a gas whenever particles come within a distance of 2 radii of each other. For simplicity, we can begin by assuming there are only two particles in the gas. This situation can then be modelled with one particle having radius

$$\delta = r_1 + r_2 \tag{A.17}$$

and the other being a zero-dimensional point. Furthermore, we can work in the reference frame where the point particle is stationary and the δ particle moves with relative velocity $\vec{v}_{\text{rel}}$. As the δ particle moves through the container, it sweeps out a cylinder with volume $\pi\delta^2 \times \ell$, where

$$\ell = v_{\text{rel}}\Delta t \tag{A.18}$$

is the relative distance that the particle has travelled. A collision will have occurred after time Δt if the point particle can be found in the swept volume. Quantitatively, this will happen on average when

$$\pi\delta^2 v_{\text{rel}}\Delta t = \frac{1}{n}, \tag{A.19}$$

with $n = N/V$ being the number density of gas particles, specifically $1/V$ in our scenario. Maxwell has shown that the average speed of a particle in a gas relative to another particle is given by [62]

$$\bar{v}_{\text{rel}} = \sqrt{2}\bar{v}, \tag{A.20}$$

where $\bar{v}$ is in the usual reference frame of the stationary container. So Equation (A.19) can be rewritten as

$$\sqrt{2}\pi\delta^2\bar{v}\Delta t = \frac{1}{n}. \tag{A.21}$$

We now define the mean free path

$$\lambda = \bar{v}\Delta t \tag{A.22}$$

as the average distance a particle travels between collisions, which occur on average every Δt seconds. Rearranging Equation (A.21), we find

$$\lambda = \frac{1}{\sqrt{2}\pi\delta^2 n}. \tag{A.23}$$

Since we have been dealing with average quantities, we can without loss of generality relax our earlier assumptions and apply this equation to any ideal gas.

A.2.3 Molecular Flow

Particles in an ideal gas interact only through collisions, and it is therefore collisions that must facilitate equilibrium. As indicated by Table A.1, the mean free path in high-quality vacua can be many kilometers long, which leads to negligibly rare collision rates as compared to a gas at atmospheric pressure. Using Equations (A.14), (A.22), and (A.23), one can calculate that a gas of pure N_2 molecules (mass $\approx 4.7\times10^{-26}$ kg, radius $\approx$ 1.9 Å [63]) has an average collision rate (per particle) of about 8.1 THz at atmospheric pressure, but only 11 μHz at 10^{-12} Torr. Consequently, low-density gases can take many orders of magnitude longer to recover after small disturbances from equilibrium than what we intuitively expect from our experiences with atmospheric gasses. When dealing with UHV environments, gasses may never reach equilibrium during the course of an experiment [64], a fact that must be taken into account when engineering high-quality vacuum systems.

The most unintuitive behaviour of a low-density gas arises when its mean free path exceeds the diameter of its enclosing vacuum chamber. In this scenario, gas particles can travel many times back-and-forth from one wall of the chamber to another without interacting with another gas particle. At the UHV pressure of 10^{-10} Torr, for example, the mean free path is roughly 500 km. In a 12"-diameter chamber, a particle is likely to collide with the chamber walls more than 1500 times before colliding with another gas particle. Each particle, therefore, behaves virtually like it is the only one in the chamber, and the interaction between the particle and the chamber walls becomes by far the more important factor determining the behaviour of the gas.

When particles in a gas behave independently due to low collision rates and long mean free paths, the gas is said to be in the molecular flow regime. For typical vacuum chambers, this constitutes any pressure below about 0.01 Torr [28]. This is in contrast to the so-called continuum flow, also known as viscous flow, regime that occurs in "high-density" gasses with pressures above about 0.1 Torr [28]. Particles in continuum flow interact with each other far more often than with the walls of the chamber, giving rise to the the fluidic properties of gasses to which we are accustomed.

A.3 Vacuum Pumps

Pumps on a vacuum system serve two purposes. First, they are used to initially pump the system down from atmospheric pressure, and second, they are used to indefinitely maintain vacuum despite the production of any gasses in the chamber. For pressures in the UHV region or lower, both of these tasks are nontrivial.

A.3.1 Rough Pumps

Before a chamber is first pumped down, it is filled with ambient air at atmospheric pressure. Gasses of this density are in continuum flow, and therefore standard pump designs can be exploited to begin evacuation. In essence, vacuum pumps designed for continuum flow gasses operate in conceptually the same manner as any fluid pump, including those designed for, say, water, but with modifications that optimize them for low-density and high-compressibility.

Pumps that operate at atmospheric pressure employ the following basic steps: An empty compartment is opened to the vacuum chamber and quickly fills with gas.[1] It is then sealed, compressed, and opened to the external environment, i.e. the air. Using further compression, virtually all of the gas is forced out of the container before it is once again sealed and expanded back to its original volume. At this point, the internal pressure of the container is much lower than that of the vacuum chamber, and the cycle repeats. In practice, the design of the compartment resembles that of a piston, at least in principle, in that one of its sides is a plate that can be pushed-up tightly against another side to effectively reduce the enclosed volume to zero. This allows almost complete evacuation into the external atmosphere so that, when the plate is pulled back again, the compartment is essentially empty.

Vacuum pumps designed for continuum flow can generally only achieve rough vacuum pressures, and are therefore known as rough pumps. Their base pressure is limited by two processes. The first is that once HV has been achieved and the gas in the vacuum chamber is in molecular flow, it takes much longer to reach equilibrium (Section A.2.3). So instead of quickly flowing into the empty compartment, the gas will tolerate being in an energetically unfavourable state and allow the compartment to stay empty for the short period of time before it is closed again. Therefore, the rate at which the pump removes gas from the chamber (in particles per unit time) drastically drops. The second limitation arises from the pump containing moving parts which necessarily have microscopic gaps between them that allow gas to leak back into the vacuum (known as backstreaming). As the pressure in the chamber lowers, the gradient across the pump increases, and so does the rate at which gas leaks. Since the change in chamber pressure is a function of the rate at which particles are removed minus the rate at which particles leak in, the pressure eventually settles at an equilibrium value roughly around the onset of HV (Figure A.1).

For HV systems, rough pumps are often lubricated with a viscous oil that serves to plug the gaps between moving parts and greatly reduce backstreaming. For systems intended to

---

[1] It is assumed that the vacuum chamber is currently filled with air and has yet to be pumped down to vacuum.

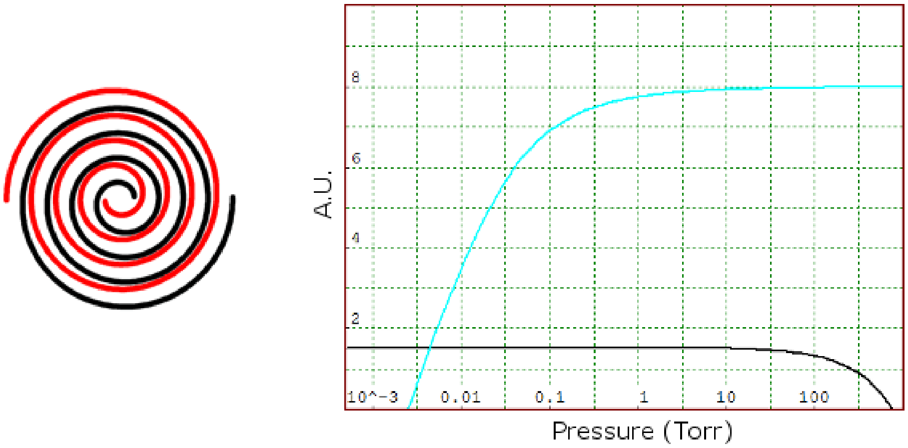

Figure A.1: Left: The pumping manifold of a scroll pump. Note the many air-tight cells formed between the two scrolls. As one scroll translates relative to the other in a circular path, the cells are compressed and move toward the exhaust outlet that sits in the center. Right: Typical performance data for a hypothetical scroll pump in arbitrary units. The black curve is the rate at which air leaks back into the vacuum. It is zero for atmospheric pressure in the vacuum chamber. The blue curve is pumping speed (volume/time), which is the net rate at which particles are removed from the chamber. The pressure at which it reaches zero is the minimum pressure that the pump can achieve. The curves are based on qualitative considerations given in Ref. [65]. The drawing of the scrolls is adapted from Ref. [66].

reach UHV or better, however, such oils cannot be used due to their high vapour pressures, and so a dry rough pump must instead be employed. Leak rates in dry pumps can be reduced by machining parts to fit tightly together and applying "non-stick" coatings such as Teflon between them, but of course these features add to the price. Of the many types of dry rough pumps available, the scroll pump is a high-performance option commonly found on UHV systems. The general operation of a scroll pump is illustrated in Figure A.1. Simplistically speaking, it consists of two interwoven spiral-shaped manifolds, known as scrolls, sandwiched between two flat plates. The center of one manifold is offset from the other such that many isolated cells form between their arms. During operation, the center of the offset manifold orbits the center of the other, which results in the cells migrating towards the exhaust port while also being compressed. Note that the scrolls do not rotate. Scroll pumps can achieve high pump rates and base pressures around 10^{-2} Torr [67].

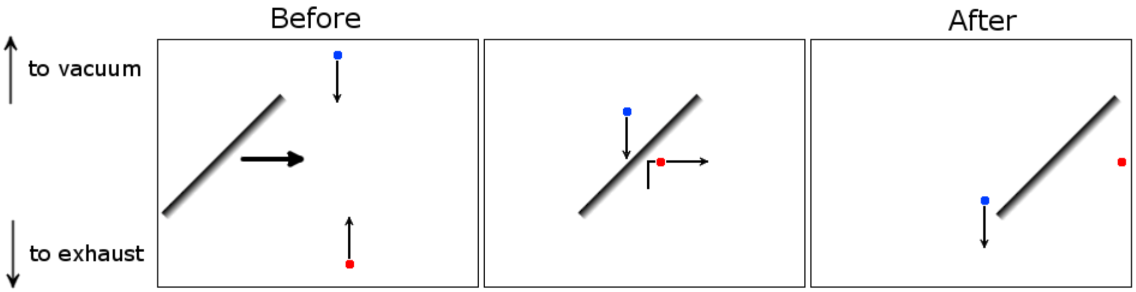

Figure A.2: Basic idea behind the operation of a turbo pump. Gas particles travelling toward the exhaust (blue) are likely to slip past the blades unhindered. Particles travelling toward the vacuum (red), however, are likely to collide with a blade and deflect back the way they came.

A.3.2 Turbomolecular Pumps

Turbomolecular pumps, or just turbos, are used to reach pressures anywhere in the range from low-quality HV to high-quality UHV and thus are available with a wide variety of performance specifications. For example, a turbo's pump speed, which determines how quickly the pump will approach it's base pressure and how much of a gas load it can handle, can range from 10 L/s to more than 2500 L/s [68]. This allows them to serve many different purposes in a variety of disciplines and applications. Their flexibility, as well as their relatively low cost and infrequently required maintenance, makes them one of the most widely used vacuum pumps [69].

A turbo pump is basically comprised of multiple high-speed fan blades, lined up in series, that attempt to "swat" any gas particles that enter the pump out of the chamber. To do this, the blades must be spinning fast enough that they move with comparable velocity to the particles in the gas. (As a reference, N_2 molecules at 300K move at roughly 52 000 cm/s.) The result is that when a particle travels towards the blades from the vacuum chamber, the angle at which the blades are tipped allow them to slip out of the way and let the particle travel through unaffected. However, particles attempting to move backward through the pump into the vacuum chamber again almost always collide with a blade and are deflected back into the pump. The basic idea is illustrated in Figure A.2. In practice, a turbo pump may contain tens or hundreds of blades, some of which more closely resemble screws than fans, that spin at different speeds and are tipped at different angles [70]. The overall speed of the pump is generally characterized by the speed of the first fan closest to the vacuum and ranges from several hundred Hz for large-diameter pumps to a few thousand Hz for smaller pumps.

Turbo pumps suffer from the restriction that they cannot be used for gasses in continuum flow. A system must already be pumped into the molecular flow regime using a rough pump before a turbo can be activated. Furthermore, while an operating turbo will maintain molecular flow conditions in the vacuum chamber, it's foreline will slowly fill with exhausted particles and require additional pumping from a rough pump in order to avoid building up to continuum flow.

One reason why turbos can only be operated at low pressures is that the blades spin at such high velocities that an extraordinary amount of power would be required to keep them running in a high-pressure gas, an obstacle that may not be impossible to overcome but is undesirably expensive. In addition, turbos generate a lot of heat when operated at high pressures. This arises partly from the power they consume, but even more troublesome is the heat generated from the friction between the blades and the air. Turbo blades are usually constructed from aircraft aluminum to keep them light [68,70], but this also makes them relatively soft. Heating the blades while under the force of a large gas load can cause them to permanently deform.

Like rough pumps, turbo pumps suffer from backstreaming due to the spacing between their moving parts. With turbos, however, the spacing is much larger (think of the spacing between fan blades) and thus limits the pump in a conceptually different way. With rough pumps, the spacing serves as sort of a constant leak, effectively the same as if a small hole was punched into the wall of the vacuum chamber. With turbos, the leak is due to the probability of a particle maneuvering its way backward through the spinning blades. The tipping of the blades makes the probability of a particle travelling forward through the pump (out of the vacuum chamber) much more likely than travelling back, but if the density of particles is much larger on the exhaust side than on the vacuum side, then there still might be a net flow of particles backward through the pump that could raise the vacuum pressure.

The density of the exhaust pressure relative to the vacuum that causes the net flow of particles through the pump to vanish is known as the pump's compression ratio, and it is unique to each individual gas species. In fact, most performance capabilities for turbos are species-specific since, for a constant temperature, every species travels at a different speed (Equation (A.14)). In general, turbos perform better for heavy (slow) particles than for light (fast) ones, and the lowest pressure that the pump can support is limited to its compression ratio for the most abundant light species in the system, typically H_2.

A.3.3 Getter Pumps

Although turbo pumps can achieve UHV pressures, it is often advantageous to employ an additional type of pump, known as a getter pump, when very low pressures are desired. Unlike rough and turbo pumps, getter pumps do not have an exhaust, but instead collect and store gas particles in a condensed form that removes them from the vacuum. In this way, getter pumps are immune to backstreaming and thus can be used to achieve exceedingly low pressures. Two common types of getter pumps are the cryopump and the titanium-based family of pumps.

The basic principle behind a cryopump, as its name implies, is based on the ability to freeze gasses into solids at cryogenic temperatures. A cryopump therefore simply consists of a manifold with a large surface area that is cooled to very low temperatures. Due to the large temperature difference between the manifold and the particle, a significant amount of energy will (on average) be exchanged during a collision such that the particle's kinetic energy is greatly reduced. The goal is to freeze the particle into the solid state so that it is permanently removed from the chamber. However, even if the manifold only holds on to the particle temporarily, it will likely do so much longer than the room-temperature walls of the chamber, and so the presence of the pump will shift the chamber's pressure to a lower equilibrium value. Furthermore, the particle is likely to be moving far more slowly after leaving the cryopump and thus be more easily removed from the chamber by other pumps, like say a turbo.

Cryopumps suffer from the disadvantage of a finite pumping capacity. Quite literally, the cryogenic manifold will eventually saturate with condensed gas that needs to be removed before pumping can continue. In fact, immediately after it is initially cooled, the manifold will gradually pump less efficiently as gas particles begin populating its surface. This is due to the fact that the layer of condensed gas has a lower sticking coefficient than the manifold surface, which was specifically engineered to have a very high coefficient. In addition, the gas layer is thermally insulating, and its outermost surface will thus be warmer than the underlying manifold. After the gas layer becomes sufficiently thick, the surface of the pump will reach a critical temperature that results in an intolerably low pumping rate, and the pump will need to be regenerated. This involves warming-up the manifold and returning the gas particles to the vacuum where they can be removed by other pumps such as turbos. Clever methods have been developed to minimize the long-term degradation of the system's pressure during this process, but the pressure will inevitably increase temporarily.

Technically speaking, cryopumps can be operated at any temperature below that of the ambient environment (~300 K) and reduce the pressure in the vacuum chamber since any reduction in temperature will reduce the vapour pressure of gas species (i.e. the rate at which particles desorb off of the chamber walls). However, the lower the temperature of the pump, the more effective it will be. Important temperatures in practical use include 0°C, below which water vapour is pumped very effectively; 77 K, which is the approximate boiling temperature of liquid N_2 [26], is thus very conveniently reachable, and can pump all but the very light gasses present in UHV; and 10 K, which is the approximate minimum temperature obtainable by commercially available cryopumps that utilize mechanical closed-loop helium refrigerators [71, 72] and can pump all gasses to an appreciable degree. The most difficult gasses to pump are of course those that have the lowest boiling point, namely H_2 and the light noble gasses, which require as low an operating temperature as possible. Even at 10 K, however, the cryopump's capacity for such gasses is very low, and it will require frequent regeneration.

Since a cryopump has no moving parts, it can be used to pump any pressure of gas. It's performance may be hindered near atmospheric pressure if the refrigeration system cannot handle the high rate at which it must remove heat, but it will still pump with significant speed. So long as the total volume of gas in the chamber is not too large, cryopumps can pump from atmospheric pressure all the way down to UHV or better without the need to regenerate, which allows them to help speed up the pump-down times of a UHV system that otherwise depends solely on turbos. In practice, cryopumps are often activated shortly after the rough pumps have evacuated the chamber to molecular flow so as to extend the interval between regenerations, but still well before UHV is reached.

Getter pumps that utilize titanium operate by the same general principles as a cryopump, except that they rely on titanium's natural ability to capture gasses without the necessity of cold temperatures [72]. Upon collision with a clean surface of titanium, many gasses are likely to form physical, and more importantly, chemical bonds that keep them stuck to the surface for very long periods, even at room-temperature. In particular, titanium pumps are employed when help is needed in removing H_2, the most troublesome of UHV gasses, which titanium can pump at high rates.

Titanium pumps consist of a reservoir of bulk titanium, commonly in the form of a thick filament or sphere, that is hooked up to a high-current power supply so that it can be resistively heated. When the reservoir is brought close to titanium's melting point, it will sublimate and spray titanium vapour into the vacuum. A layer of titanium will then be deposited on the nearby walls of the chamber when the vapour undergoes its first collision, cools, and re-condenses back into the solid state. If setup correctly, the layer can be spread very thin and produce a large surface area to maximize pumping speed. When the layer eventually saturates with captured gasses, the pump can then be regenerated by heating the reservoir again and depositing a new layer of titanium overtop of the old one.

Therefore, unlike cryopumps, titanium pumps permanently remove gas from the chamber by burying it underneath solid titanium, and the trapped particles never have to return to the vacuum. However, regeneration can still significantly degrade vacuum pressures since the reservoir needs to be heated to a very high temperature, which inadvertently heats other components in the chamber and temporarily increases outgassing rates. Furthermore, refilling the finite reservoir of titanium requires the chamber to be periodically (albeit quite infrequently) opened to the ambient atmosphere, which detrimentally affects the vacuum quality for days or even weeks afterward.

The type of titanium pump just described is known as a titanium sublimation pump (TSP). Other variations of titanium pumps exist, most notably the ion pump which is very common on many UHV systems. Unlike TSP's, ion pumps can run continuously without the need for aggressive regeneration. However, they are often strictly reserved for maintaining UHV, whereas TSP's can be used in HV. Both ion pumps and TSP's can in theory operate in pressures as high as atmospheric, but they are highly inefficient under continuum flow conditions. Our spectrometer contains only TSP's, and so discussion in the text is limited to this variety of titanium-based getter pump.

Appendix B

Unit Conversions

B.1 Pressure Units

Table B.1: Conversion table of common pressure units. Values taken from Ref [26].

	Torr	Pa	bar	psi	mmHg	atm
Torr	1	133.322	1.33322×10^{-3}	0.01933672	1	1.31579×10^{-3}
Pa	7.5006×10^{-3}	1	10^{-5}	1.450377×10^{-4}	7.5006	9.8692×10^{-6}
bar	750.06	10^{5}	1	14.50377	750.06	0.98692
psi	51.7151	6894.757	0.06894757	1	51.7151	0.068046
mmHg	1	133.322	1.33322×10^{-3}	0.01933672	1	1.31579×10^{-3}
atm	760	101325	1.01325	14.69594	760	1

To use the table, find the row with the initial units. Then run across to the column with the final units. Multiply by the number in the cell to perform the conversion. For example,

$$500 \text{ Pa } \times 0.0075006 = 3.7503 \text{ Torr.}$$

Other common pressure units include:

- 1 micron = 0.001 mmHg
- 1 mbar = 0.001 bar

- 1 kPa = 1000 Pa

Pressure units may sometimes be stated with a trailing “g” or “a.” The former stands for gauge pressure and implies that the reading is relative to 1 atm. The latter stands for absolute pressure and is used to explicitly state that the measurement is not a gauge pressure. This is most commonly found using psi:

$$\begin{aligned} 1 \text{ psig } &= 1 \text{ psia } + 1 \text{ atm} \\ &= 1.068046 \text{ psia.} \end{aligned}$$

Today, the mmHg is, for all practical purposes, considered to be equivalent to the Torr. However, the mmHg is defined using the density of mercury and the accleration due to gravity, g. As the accepted values of these constants have changed with time, so too has the precise value of a mmHg.

B.2 Other Units

Except for pressure, most units frequently used in today’s literature conform to the SI standard. However, a few from the US customary units system are still in widespread use in North America, especially in industry. Some notable examples include [26]:

- 1 in = 2.54 cm
- 1 cubic foot = 28.316846592 L
- x°F = $(\frac{x-32}{1.8})$°C

Appendix C

UHV-Compatible Materials

The use of a material in UHV is appropriate only if that material has a very low vapour pressure, a low permeability to gasses (if used to separate UHV from higher pressures, like in the wall of a vacuum chamber), and a low outgassing rate (due to adsorbed or trapped gasses that cannot easily be removed in situ with baking).

Table C.1: Materials of note used in the IPES spectrometer.

Material	Description	Where it's Used
μ-Metal	Alloy with an especially high magnetic permeability that can therefore be used for magnetic shielding. Composition is proprietary, but likely contains approximately 77% Ni, 16% Fe, 5% Cu, and 2% Cr or Mo.	The IPES chamber is made of μ-metal. Also, the LEED is surrounded by a μ-metal shield.
316 Stainless Steel	A non-magnetic stainless steel alloy. Contains approximately 16% Cr, 10% Ni, and 2% Mo.	All miscellaneous steel parts in and around the IPES chamber, when available.

Continued on next page...

Table C.1 – Continued from previous page

Material	Description	Where it's Used
Aluminum 6061	High-purity aluminum alloy. Other elements make up less than 5% by weight, most notably Mg, Si, and Fe. Is generally the cheapest, widely-available, UHV-compatible metal for machining custom parts. Is non-magnetic.	The sample garage, sample receptacle, and various sample holder parts.
OFHC Copper	Stands for "Oxygen-Free, High-Conductivity" copper. Greater than 99% pure copper, particularly with low oxygen contamination.	Heater stage rails. Various sample holder parts.
PEEK	Stands for "polyether ether ketone." Is a relatively strong plastic with a high melting point.	Terminal block on the heater stage. Screws and washers on the sample receptacle for electrical insulation.
MACOR	Silicon-based ceramic. Composition is proprietary. Machinable, strong, electrically and thermally insulating, low thermal expansion, high melting point.	Electrical spacers in GM detectors.
Kapton	Versatile plastic film.	Insulation for the wiring connected to the Faraday cup and sample receptacle.
Steatite	A.k.a. soapstone. Naturally occurring mineral.	Ceramic beads insulating the heater stage wiring.
CaF_2	Brittle ionic crystal. Used for optics applications.	Entrance windows in GM detectors.

Table C.2: Other important UHV-compatible materials.

Material	Notes
18-8 Stainless Steel	All stainless steel alloys that contain approximately 18% Cr and 8% Ni. They are a subset of the 300 series of stainless steels, a.k.a. "austenitic" stainless steels. They are likely to be magnetic, but often less so than other steels.
304 Stainless Steel	A high-quality 18-8 stainless steel alloy. If available, it is preferable over other alloys in the 300 series (except perhaps 316).
300 Series Stainless Steel	Be careful when considering the use of a 300 series stainless steel that is not 18-8. Some alloys contain metals with high vapour pressures.
Viton	Proprietary synthetic rubber used as a reusable O-ring for CF flanges and KF flanges. For CF, does not usually seal as well as copper O-rings due to the difficulty getting it to seat properly.
Kalrez	Proprietary synthetic rubber similar to Viton, but more expensive. Used in our gate valves' O-rings. Permeable to He.
Silicate	A.k.a. glass. Used as the window in most viewports.
Gold	Too expensive to be used except for specialized applications.
Silver	Too expensive to be used in large components, but commonly found in the silver paint and silver epoxy that our group uses for sample preparation.
Titanium	Can be used as a substitute for Al as a nonmagnetic metal. Fresh surfaces will absorb/adsorb many gas species (particularly H_2) to act as a getter pump.
Kapton	A common application is for UHV-compatible tape.
Carbon Tape	Proprietary double-sided tape. Carbon-rich, electrically conductive glue on a core of plastic fibres.
Magic Tape	As in Scotch brand invisible tape. Proprietary composition found to be UHV-compatible. Does not bake well.
Beryllium Copper	A.k.a. spring copper. Useful for mounting samples.

Appendix D

Contact Potential

When two metals[1] are brought into electrical contact, the chemical potential (i.e. Fermi level) of their electrons will become the same once thermodynamic equilibrium is reached [16]. This is facilitated by electrons diffusing from the material with a higher chemical potential to the one with a lower potential, which causes the materials to charge. The material with the higher potential will become positively charged, and its electronic states, as well as its chemical potential, will thus shift to a lower (in magnitude) potential energy. Conversely, the material with a lower potential becomes negative and shifts to a higher energy. The number of electrons that need to flow before the chemical potentials become equal and the process stops is very small relative to the total number of electrons in the material, and therefore the nature of the electronic states, including their occupancy which dictates the material's Fermi level, remains effectively unaltered save for the uniform shift in energy. The difference in electrical potential between the two materials after equilibrium has been achieved is known as the contact potential, and its calculation is nontrivial. For IPES, it is important to remember that its value will be different for nonequivalent crystal surfaces and therefore depends on both the composition and crystallographic orientation of the sample.

When no voltages are applied, the sample and the cathode of the low-energy electron gun are in electrical contact (or rather both connected to a common ground) and thus their Fermi levels will be at the same energy. Defining this energy as zero, the cathode will thermionically emit electrons with an energy equal[2] to its work function, Φ_g. If the

---

[1] Or two materials that conduct electrons freely.

[2] Or slightly higher, depending on the cathode's temperature. Since the energy of emission relative to the cathode's Fermi level remains constant, however, the cathode's work function could be replaced by an effective work function $\Phi'_g = \Phi_g + \delta$, and the derivation would remain unchanged.

sample's work function, Φ_s, is larger than Φ_g, then these electrons will not be able to overcome the potential barrier and couple into the sample. The cathode will have to be raised to a voltage

$$V_g = \frac{\Phi_s - \Phi_g}{e} \tag{D.1}$$

before current will flow (Figure D.1). More generally, the sample can be held at an arbitrary voltage V_s, and by the same logic the cathode will have to be raised to a voltage

$$V_g = V_s + \frac{\Phi_s - \Phi_g}{e} \tag{D.2}$$

to induce a current. Rearranging, we find that

$$e(V_g - V_s) = \Phi_s - \Phi_g. \tag{D.3}$$

Essentially, this difference in voltage is required to overcome the difference generated by the electrical contact, and therefore Equation (D.3) defines the contact potential between the sample and the cathode [18, 19]. Explicitly, the quantitative definition of the contact potential is given by

$$\Delta = \Phi_s - \Phi_g. \tag{D.4}$$

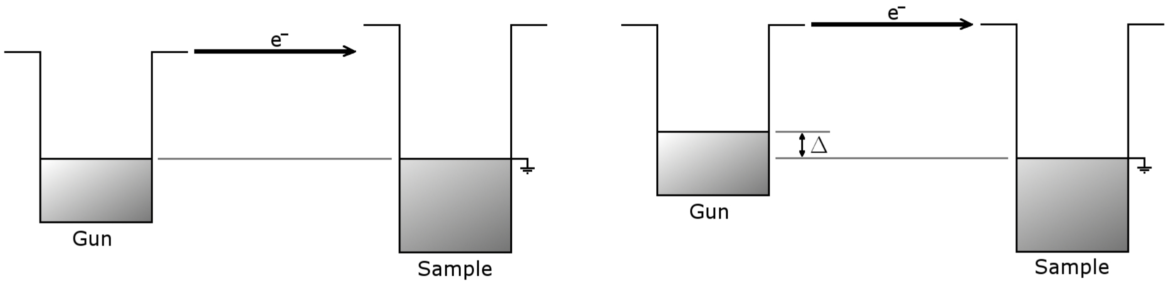

Figure D.1: Left: Energy diagram of the sample and electron gun's cathode when no external voltages are applies. Note that electrons cannot travel over the potential barrier from the gun to the sample. Right: Energies when Equation (D.3) is satisfied. The voltage difference between the sample and the cathode, Δ, is at the threshold value such that current can start to flow.

To find the contact potential for a particular sample, the procedure just outlined can be followed. Holding the sample at an arbitrary voltage, the energy of the electron beam is varied until the threshold value at which current starts to flow through the sample is found. Substituting the difference between the voltage on the sample and the cathode into Equation (D.3) yields Δ, which can then be used in Equation (2.16) to determine the kinetic energy of the incident electrons for any value of the cathode voltage. Note that this method is robust against unknown offsets that may exist between the various voltages around the vacuum system. For example, the sample and cathode voltages may be referenced from slightly different grounds, which would lead to an erroneous calculation of their difference. However, such a case would simply result in an effective value for Δ that would still ensure an accurate calculation of E_k.

As stated in the text, it is also important to note that the contact potential will vary depending on the crystallographic face that is being measured, even if they belong to the same crystal. So measuring Δ for one face, say Cu(111) for example, may not give you the correct Δ on a different face, Cu(100).

Appendix E

The Effect of an External Magnetic Field on the Low-Energy Electron Gun

When an electron experiences a magnetic force perpendicular to its direction of motion, it will travel in an arc with radius r_c, known as the cyclotron radius. The magnitude of the magnetic force is given by the Lorentz equation

$$F = evB\sin\theta, \tag{E.1}$$

where e is the electronic charge, v is the electron's speed, B is the magnitude of the magnetic field vector, and θ is the angle between $\vec{v}$ and $\vec{B}$. In our case, $\theta = 90^\circ$ and we can apply the circular motion equation

$$F = \frac{m_\mathrm{e} v^2}{r_c}, \tag{E.2}$$

where m_e is the electronic mass. Combining Equations (E.1) and (E.2), we find that the cyclotron radius is

$$r_c = \frac{m_\mathrm{e} v}{eB}, \tag{E.3}$$

or as a function of the electron's kinetic energy,

$$r_c = \frac{\sqrt{2 m_\mathrm{e} E}}{eB}. \tag{E.4}$$

The magnitude of Earth's magnetic field in the city of Waterloo is about 55 μT [73], which for a 10 eV electron corresponds to a cyclotron radius of about 19.4 cm. For a typical sample position 2 cm from the end of the electron gun, this amounts to a deflection of roughly 1.03 mm and a rotation of the incident angle by about 5.92°. Given that the unperturbed beam has a spot size and angular spread of around 1 mm^2 and 5°, respectively, the presence of the Earth's field can clearly have a significant effect on the nature of the beam. In particular, the uncertainty in the incident angle can approximately double, causing the uncertainty in $\vec{k}_{\parallel}$, given by

$$\Delta k_{\parallel} = k \sin\theta \sqrt{\left(\frac{\Delta k}{k}\right)^2 + \cot^2\theta (\Delta\theta)^2}, \tag{E.5}$$

to increase substantially.

We have recorded the magnetic field strength in the μ-metal chamber at unmeasurably low levels, which for our magnetometer must be at least an order of magnitude less than the strength of Earth's field. We can therefore claim an upper limit on the uncertainty in the beam's incident angle caused by external magnetic fields of about 0.5°.

Appendix F

Solid Angle Collected by the GM Photodetectors

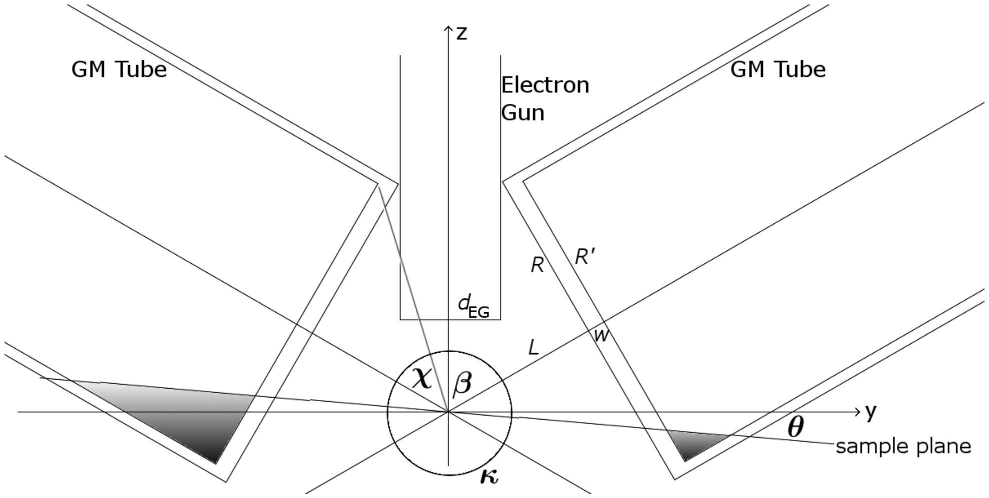

Figure F.1: Detailed schematic of the geometry used to optimize the position of the GM tubes. The sample is positioned at the origin. It can rotate in the plane by angle θ.

Figure F.1 shows the geometry of the GM detectors in proximity to the sample. The solid angle collected by each detector is given by

$$\Omega = 2\pi(1-\cos\chi) - \iint_S \sin\theta' d\theta' d\phi', \tag{F.1}$$

where S is the surface of the detector's innermost window below the sample plane and χ is the half angle of the cone that that is formed by the innermost window and the sample's center. The latter is found from

$$\chi = \tan^{-1} \frac{R'}{L+w}, \tag{F.2}$$

where R' is the radius of the innermost window, w is the distance from the front of the detector to the back of the innermost window, and L is the distance from the detector to the sample center. That distance is calculated as

$$L = \begin{cases} \frac{1}{2}d_{\mathrm{EG}} + R\cot\beta & \text{if } \frac{1}{2}d_{\mathrm{EG}} + R\cot\beta \geq \kappa \\ \kappa & \text{otherwise} \end{cases}, \tag{F.3}$$

where $d_{\mathrm{EG}} = 34$ mm is the diameter of the electron gun, R is the detector's radius, and κ is the radius swept by the sample holder, with which the detector must avoid a collision. For our calculations, we used $\kappa = 20$ mm, which is a bit larger than the radius of the sample receptacle. The integral in Equation (F.1) can then be computed in Cartesian coordinates:

$$\iint_S \sin\theta' d\theta' d\phi' = \iint_S \frac{z\cos\beta + [L'\sin\beta - \cot\beta\,(z - L'\cos\beta)]\sin\beta}{\sin\beta\left\{x^2 + z^2 + [L'\sin\beta - \cot\beta\,(z - L'\cos\beta)]^2\right\}^{3/2}} dxdz, \tag{F.4}$$

where $L' = L + w$. The domain over which x is integrated is given by

$$|x| < \begin{cases} \sqrt{R'^2 + L'^2 - Z_{\mathrm{int}}^2 - [L'\sin\beta - \cot\beta(Z_{\mathrm{int}} - L'\cos\beta)^2]} & \beta \leq 90^\circ + \theta \\ \sqrt{R'^2 + L'^2} & \text{otherwise} \end{cases} \tag{F.5}$$

where

$$Z_{\mathrm{int}} = \frac{(L+w)\sin\theta}{\cos\beta\sin\theta - \sin\beta\cos\theta}. \tag{F.6}$$

The z domain is defined by

$$(L+w)\cos\beta - \sin\beta\sqrt{R'^2 - x^2} < z < Z_{\mathrm{int}} \tag{F.7}$$

if $\beta \leq 90^\circ + \theta$ and

$$(L+w)\cos\beta - \sin\beta\sqrt{R'^2 - x^2} < z < (L+w)\cos\beta + \sin\beta\sqrt{R'^2 - x^2} \tag{F.8}$$

otherwise.

Appendix G

Penetration Depth of Acetone

For the detection energy of 9.6 eV in a $\mathrm{CaF_2}$/acetone GM photodetector, the absorption cross section of the acetone gas is roughly $\sigma = 26$ Mb [74], or 26×10^{-22} m^2. The penetration depth of the gas, δ, is defined as the distance a photon beam can travel through it before its intensity, I, drops to $1/e$ of its original value. According to the Beer-Lambert law,

$$I = I_0 e^{-n\sigma x}, \tag{G.1}$$

where n is the particle density of the gas and x is the distance travelled. Therefore, the penetration depth is given by

$$\begin{aligned} \delta &= \frac{\ln \frac{1}{e}}{-n\sigma} \\ &= \frac{1}{n\sigma}. \end{aligned} \tag{G.2}$$

The acetone behaves as an ideal gas, so we can substitute Equation (A.15) to obtain

$$\delta = \frac{kT}{P\sigma}. \tag{G.3}$$

At $T = 300$ K, the penetration depth as a function of acetone pressure is thus

$$\delta\,[\mathrm{cm}] \approx \frac{1.1949}{P\,[\mathrm{Torr}]}. \tag{G.4}$$

So for typical pressures of the detection gas ranging from 0.1 to 10 Torr, the penetration depth will range from about 12 cm to 1.2 mm, respectively. This verifies that the incident photon beam can still have significant intensity when it reaches the structural supports inserted into the cathode of the proposed GM tube in Section 4.4.1, and they must therefore be made with a small cross section to limit reductions in photon detection.

Appendix H

Wiki

Our group's website (http://dhawthorn.uwaterloo.ca/) contains a wiki[1] that group members can log into to find and edit information on a variety of topics. Most of the wiki is intended to be helpful with practical issues such as performing an experiment or preparing a particular sample material. A substantial portion deals with our group's activities at the Canadian Light Source, but the majority is related to the procedures involved with operating the IPES spectrometer. Tutorials for various equipment and useful information about materials that are commonly encountered in our lab can also be found. Some of this includes health and safety information that will hopefully be more readily available in electronic format. In addition, the wiki provides some history of the spectrometer and its various apparatus that group members may find interesting.

Figure H.1: The logo for our group's wiki.

---

[1] Created by Mirko Vucicevich.

Appendix I

Technical Drawings

The following figures elaborate on the information given in the text regarding various equipment related to the IPES spectrometer. All drawings and the equipment they describe were created by the author.

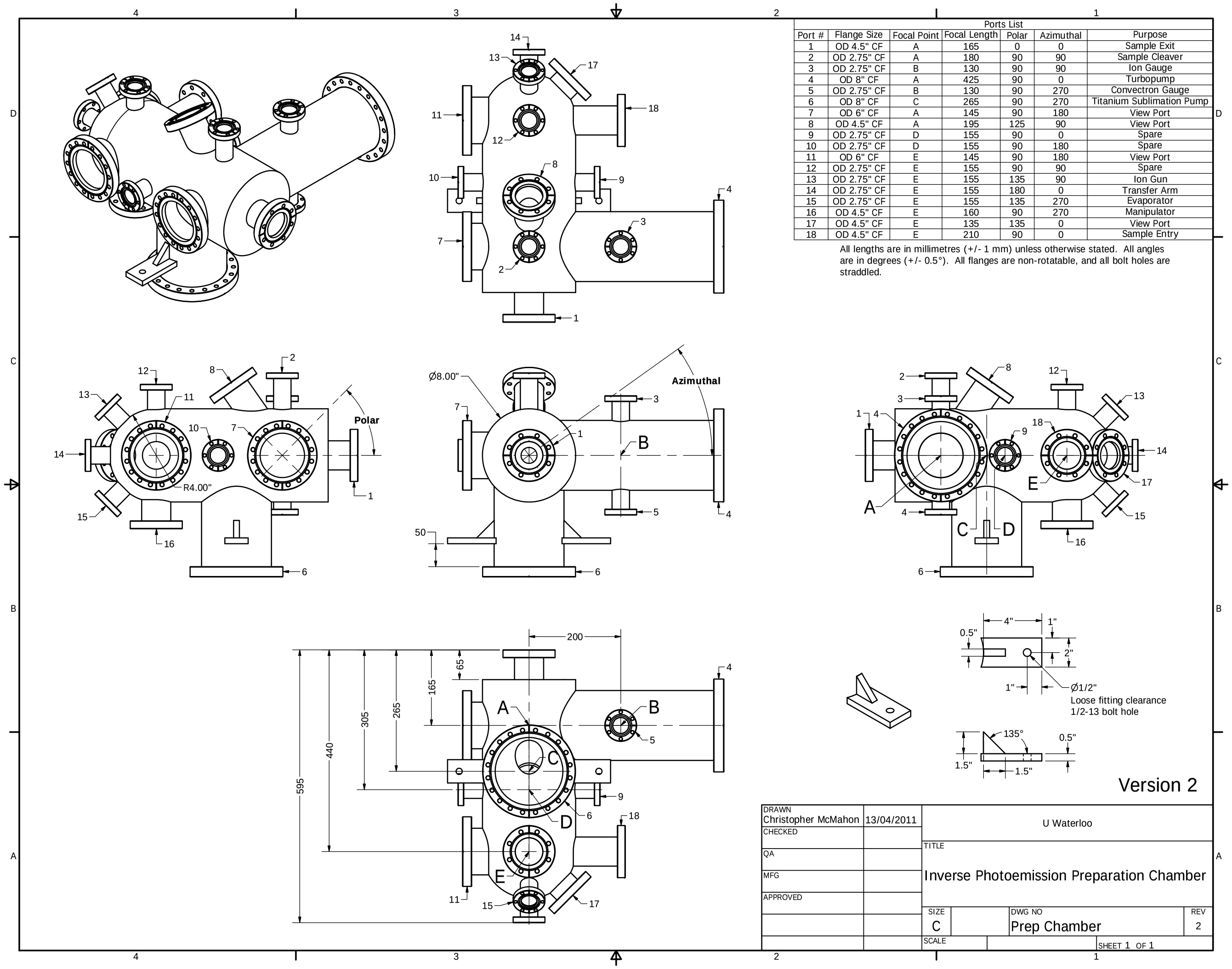

Ports List						
Port #	Flange Size	Focal Point	Focal Length	Polar	Azimuthal	Purpose
1	OD 4.5" CF	A	165	0	0	Sample Exit
2	OD 2.75" CF	A	180	90	90	Sample Cleaver
3	OD 2.75" CF	B	130	90	90	Ion Gauge
4	OD 8" CF	A	425	90	0	Turbopump
5	OD 2.75" CF	B	130	90	270	Convectron Gauge
6	OD 8" CF	C	265	90	270	Titanium Sublimation Pump
7	OD 6" CF	A	145	90	180	View Port
8	OD 4.5" CF	A	195	125	90	View Port
9	OD 2.75" CF	D	155	90	0	Spare
10	OD 2.75" CF	D	155	90	180	Spare
11	OD 6" CF	E	145	90	180	View Port
12	OD 2.75" CF	E	155	90	90	Spare
13	OD 2.75" CF	E	155	135	90	Ion Gun
14	OD 2.75" CF	E	155	180	0	Transfer Arm
15	OD 2.75" CF	E	155	135	270	Evaporator
16	OD 4.5" CF	E	160	90	270	Manipulator
17	OD 4.5" CF	E	135	135	0	View Port
18	OD 4.5" CF	E	210	90	0	Sample Entry

All lengths are in millimetres (+/- 1 mm) unless otherwise stated. All angles are in degrees (+/- 0.5°). All flanges are non-rotatable, and all bolt holes are straddled.

Version 2

DRAWN Christopher McMahon	13/04/2011	U Waterloo
CHECKED		
QA		TITLE
MFG		Inverse Photoemission Preparation Chamber
APPROVED		SIZE C · DWG NO Prep Chamber · REV 2
		SCALE · SHEET 1 OF 1

Figure I.1: Preparation chamber specifications

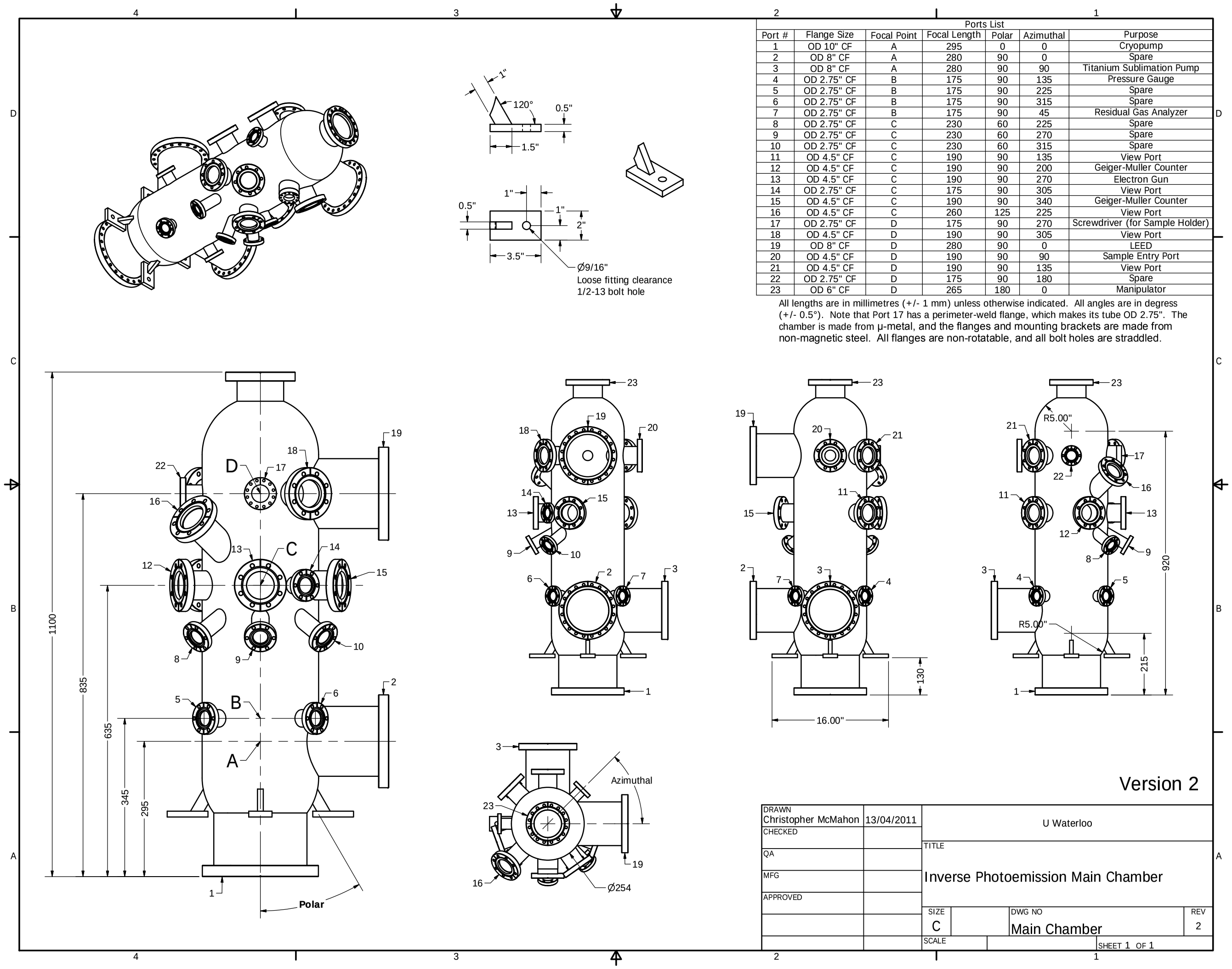

Ports List

Port #	Flange Size	Focal Point	Focal Length	Polar	Azimuthal	Purpose
1	OD 10" CF	A	295	0	0	Cryopump
2	OD 8" CF	A	280	90	0	Spare
3	OD 8" CF	A	280	90	90	Titanium Sublimation Pump
4	OD 2.75" CF	B	175	90	135	Pressure Gauge
5	OD 2.75" CF	B	175	90	225	Spare
6	OD 2.75" CF	B	175	90	315	Spare
7	OD 2.75" CF	B	175	90	45	Residual Gas Analyzer
8	OD 2.75" CF	C	230	60	225	Spare
9	OD 2.75" CF	C	230	60	270	Spare
10	OD 2.75" CF	C	230	60	315	Spare
11	OD 4.5" CF	C	190	90	135	View Port
12	OD 4.5" CF	C	190	90	200	Geiger-Muller Counter
13	OD 4.5" CF	C	190	90	270	Electron Gun
14	OD 2.75" CF	C	175	90	305	View Port
15	OD 4.5" CF	C	190	90	340	Geiger-Muller Counter
16	OD 4.5" CF	C	260	125	225	View Port
17	OD 2.75" CF	D	175	90	270	Screwdriver (for Sample Holder)
18	OD 4.5" CF	D	190	90	305	View Port
19	OD 8" CF	D	280	90	0	LEED
20	OD 4.5" CF	D	190	90	90	Sample Entry Port
21	OD 4.5" CF	D	190	90	135	View Port
22	OD 2.75" CF	D	175	90	180	Spare
23	OD 6" CF	D	265	180	0	Manipulator

All lengths are in millimetres (+/- 1 mm) unless otherwise indicated. All angles are in degress (+/- 0.5°). Note that Port 17 has a perimeter-weld flange, which makes its tube OD 2.75". The chamber is made from μ-metal, and the flanges and mounting brackets are made from non-magnetic steel. All flanges are non-rotatable, and all bolt holes are straddled.

Version 2

DRAWN Christopher McMahon	13/04/2011	U Waterloo
CHECKED		TITLE Inverse Photoemission Main Chamber
QA		
MFG		
APPROVED		SIZE C · DWG NO Main Chamber · REV 2
		SCALE · SHEET 1 OF 1

Figure I.2: IPES chamber specifications

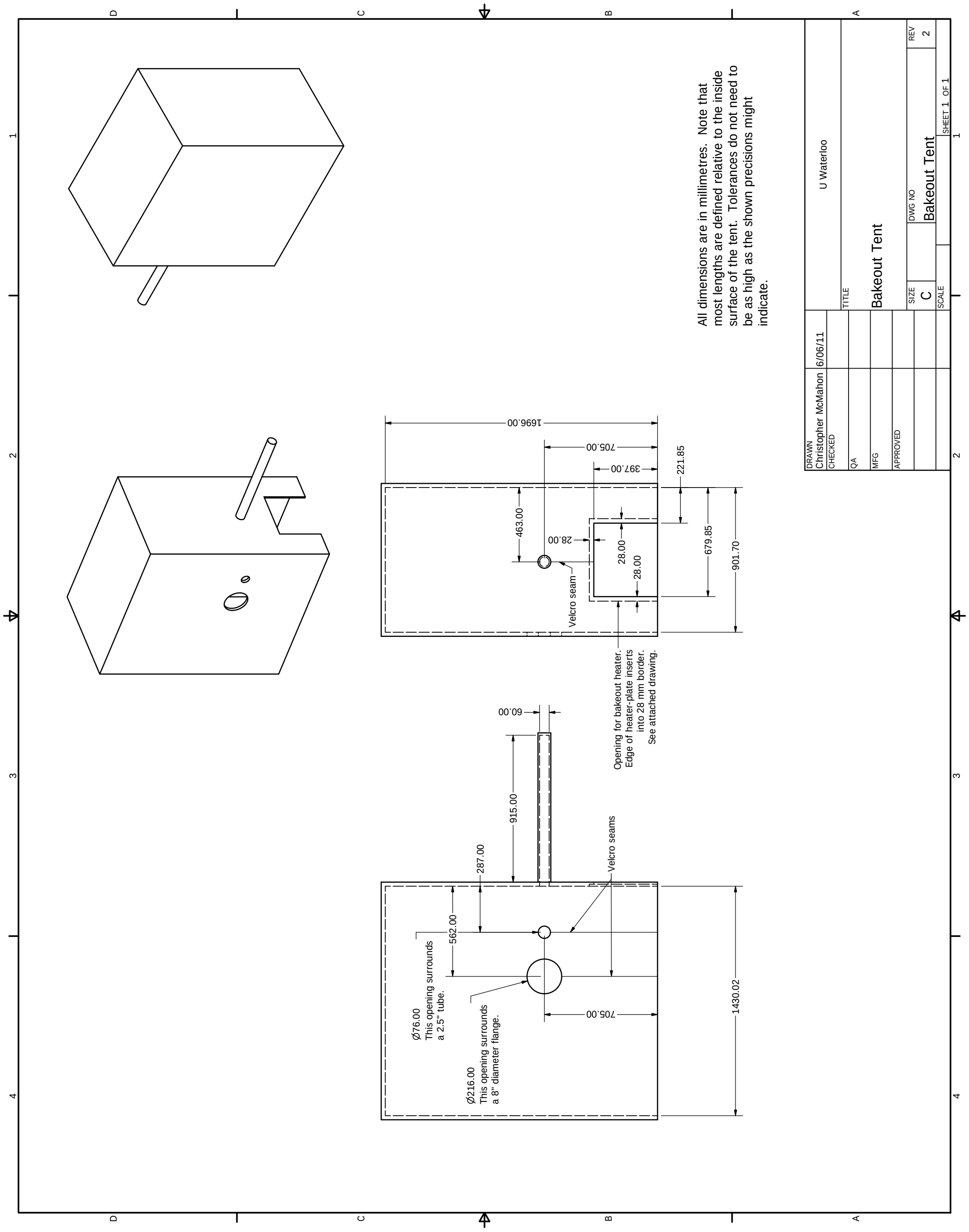

Figure I.3: Bakeout tent

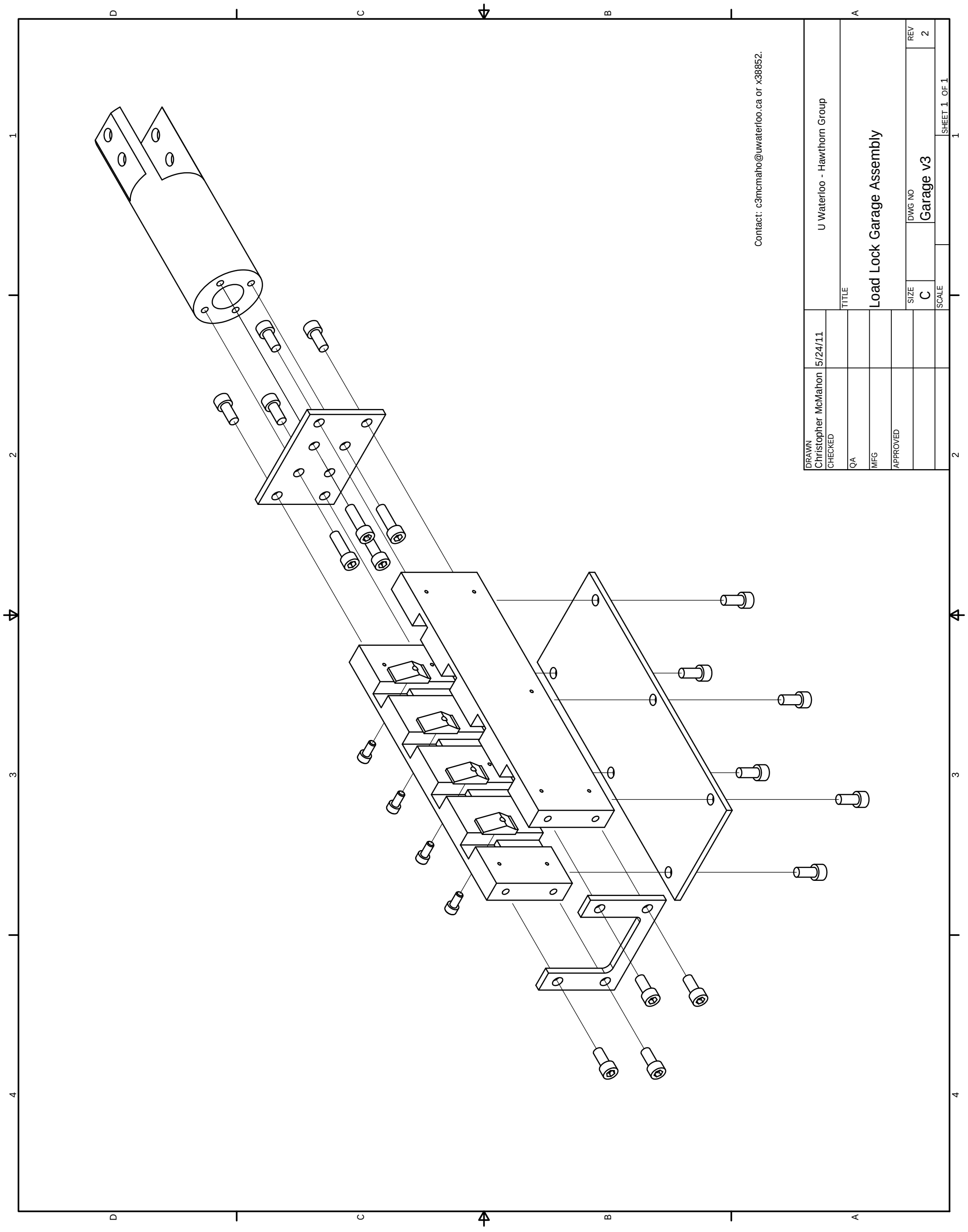

Figure I.4: Load-lock garage explosion

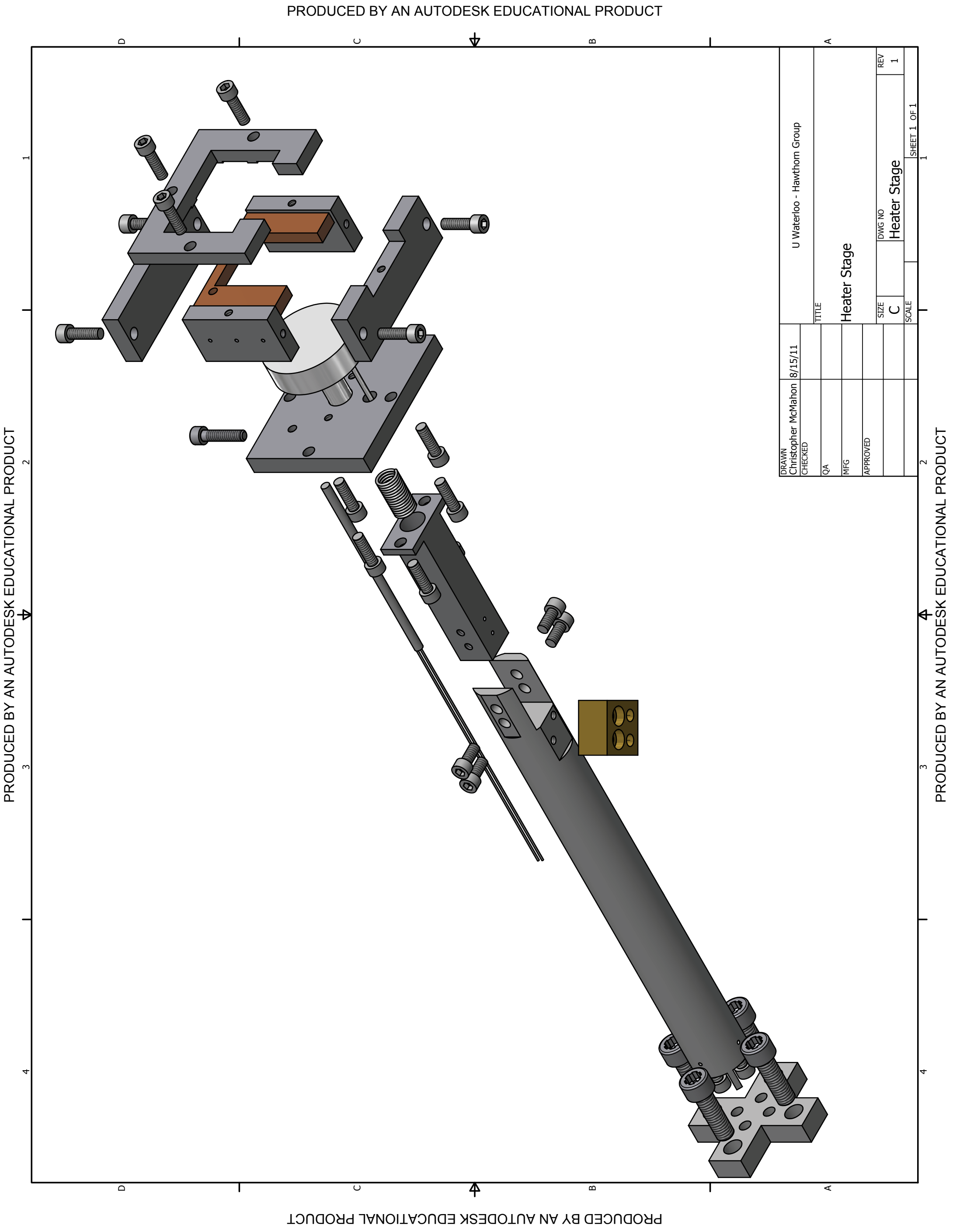

Figure I.5: Heater stage explosion

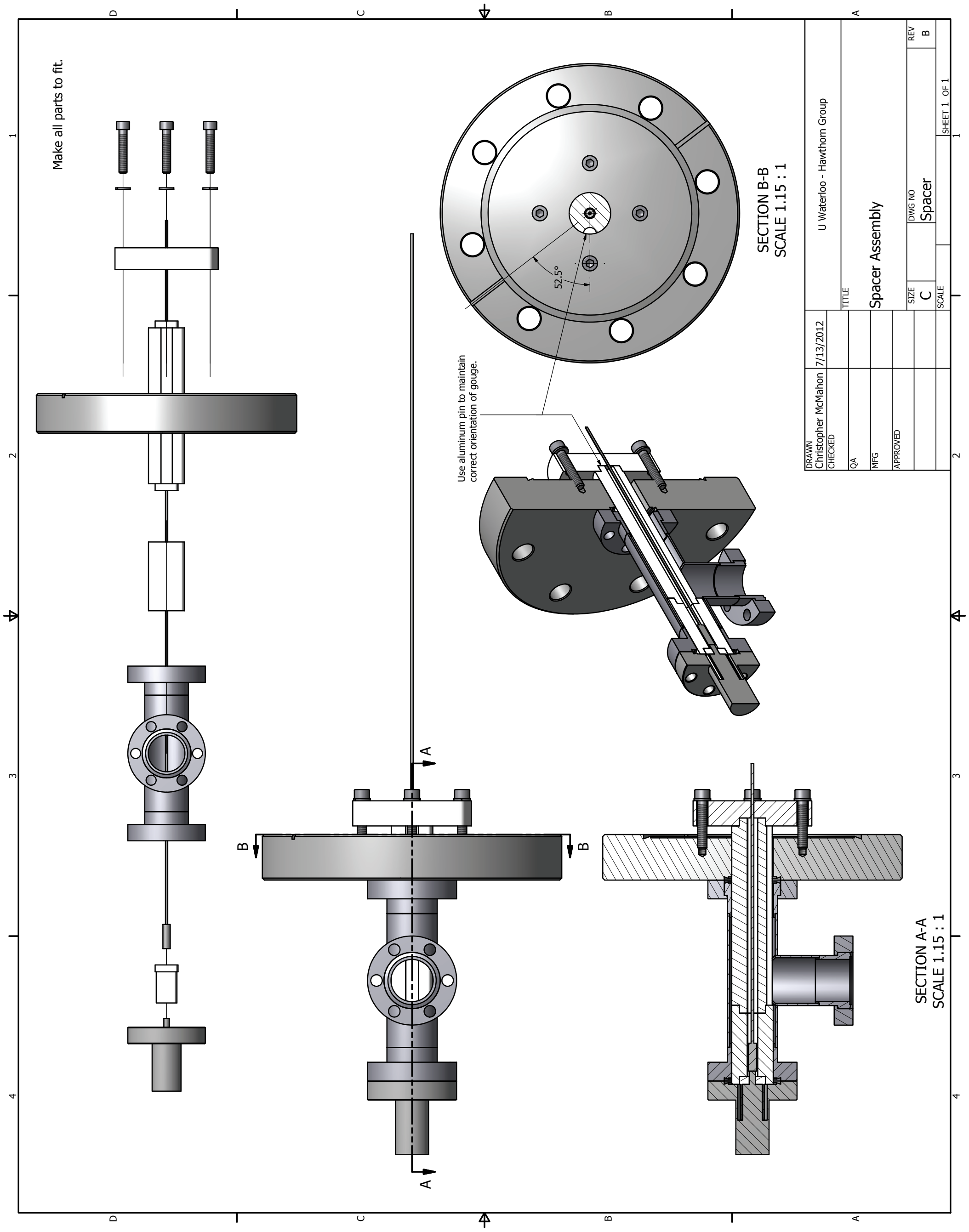

Figure I.6: MACOR spacers in GM detectors

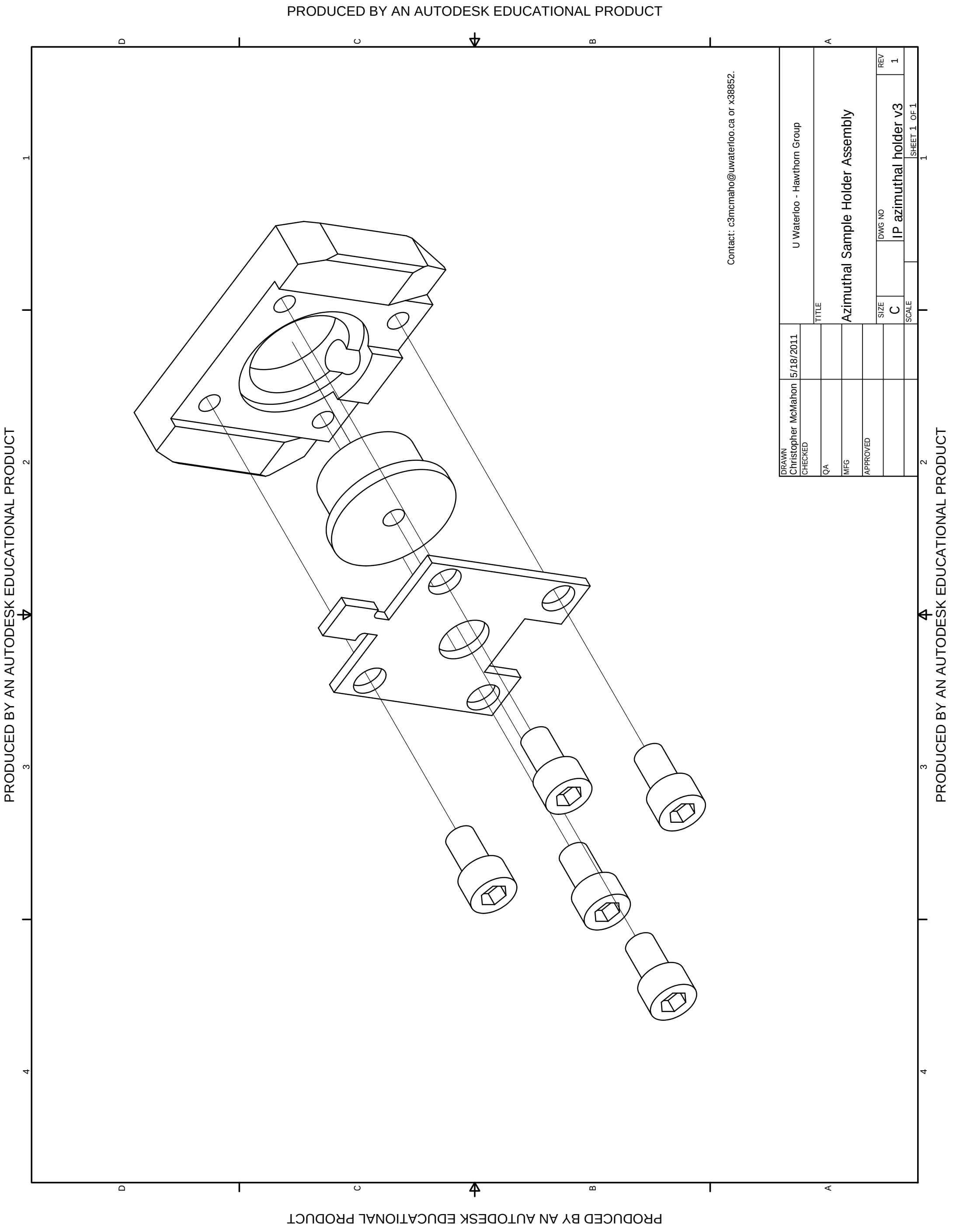

Figure I.7: Azimuthal sample holder explosion

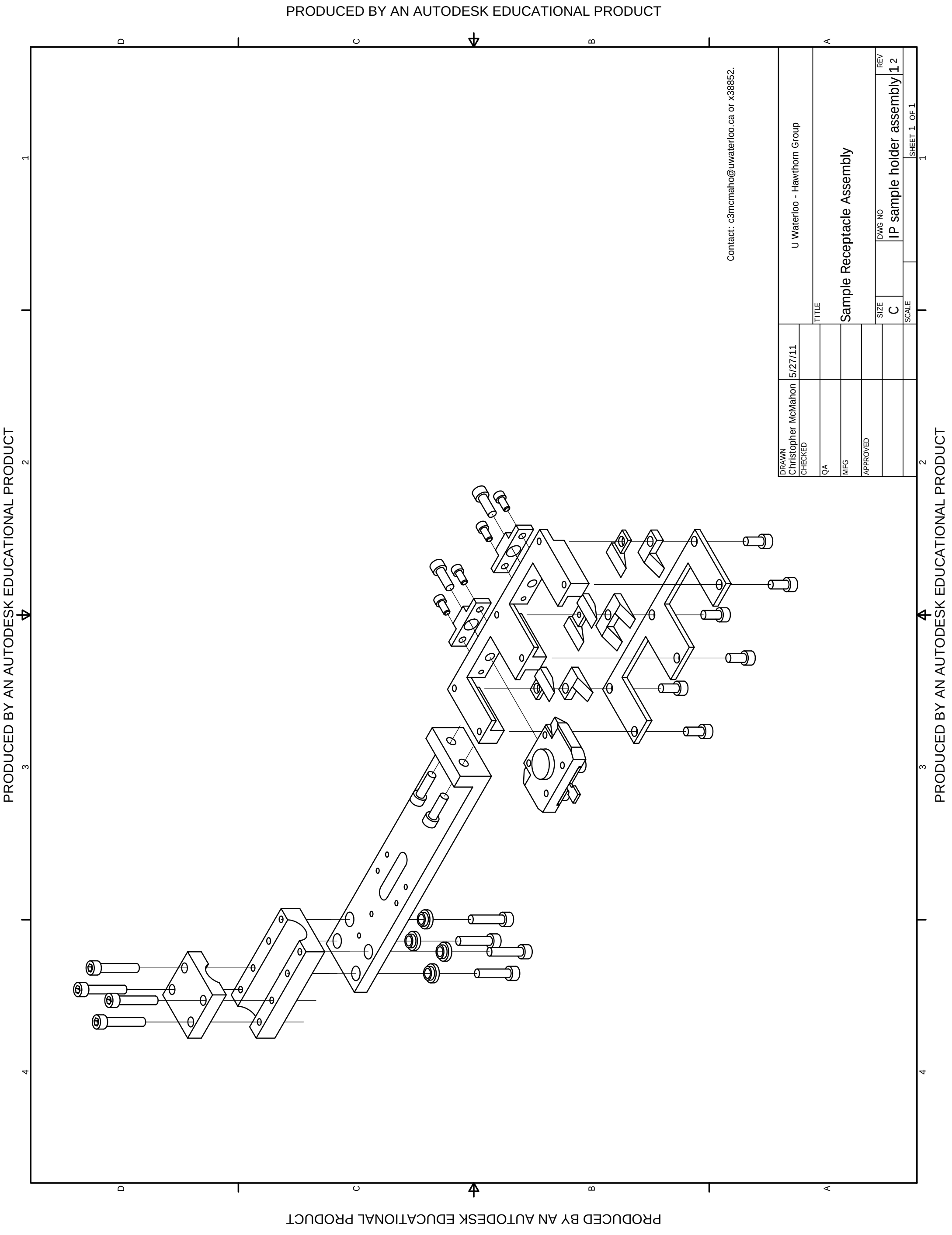

Figure I.8: Sample receptacle explosion